GROWTH AND CHARACTERIZATION OF NOVEL, III-V SEMICONDCONDUCTOR HETEROSTRUCTURES

Thesis by
Douglas Collins

In Partial Fulfillment of the Requirements
for the Degree of
Doctor of Philosophy

California Institute of Technology
Pasadena, California

1994

(Submitted June 28, 1993)

To Nick and Debbie

List of Publications

Work related to this thesis has been, or will be, published under the following titles:

Chapter 2

"Evidence for coherent interaction between quantum well states in AlAs/GaAs triple barrier heterostructures," D.A. Collins, D.H. Chow, D.Z.-Y. Ting, E.T. Yu, J.R. Söderström and T.C. McGill, *Superlattices and Microstructures* **8**, pg. 455 (1990).

"Large peak-to-valley current ratios in triple barrier heterostructures," D.A. Collins, D.H. Chow, D.Z.-Y. Ting, E.T. Yu, J.R. Söderström and T.C. McGill, *Sol. Sta. Elec.* 32(12), 1095 (1989).

"The effect of the X-point on escape of electrons from the quantum well of a double-barrier heterostructure," M.K. Jackson, D.Z.-Y. Ting, D.H. Chow, D.A. Collins, J.R. Söderström and T.C. McGill, *Phys. Rev. B.*, 43(6), 4856 (1991).

"X-point tunneling in AlAs/GaAs double arrier heterostructures," D.Z.-Y. Ting, M.K. Jackson, D.H. Chow, J.R. Söderström, D.A. Collins and T.C. McGill, *Sol. Sta. Elec.* 32(12), 1513 (1989).

Chapter 3

"Prospects for the future of narrow-gap materials.", T.C. McGill and D.A. Collins, Semi, Sci. Tech. 8(1), 1 (1993).

"InAs/GaSb/AlSb: the material system of choice for novel tunneling devices," D. A. Collins, D. H. Chow, E. T. Yu, D. Z.-Y. Ting, J.R. Söderström, Y. Rajakarunanayake, and T. C. McGill, *Resonant Tunneling in Semiconductors*, L.L. Chang Ed. Plenum Press, New York, 1991.

"Interband tunneling in InAs/GaSb/AlSb heterostructures," D. A. Collins, D.Z.-Y. Ting, E. T. Yu, D. H. Chow, J.R. Söderström, Y. Rajakarunanayake, and T. C. McGill, *J. Crys. Growth* 111(1-4), 664 (1991).

"Demonstration of resonant transmission in InAs/GaSb/InAs interband tunneling devices," E.T. Yu, D.A. Collins, D.Z.-Y. Ting, D.H. Chow and T.C. McGill, *Appl. Phys. Lett.* 57(25), 2675 (1990).

"Large peak current densities in novel resonant interband tunneling heterostructures," D.Z.-Y. Ting, D.A. Collins, E.T. Yu, D.H. Chow and T.C. McGill, *Appl. Phys. Lett.* 57(12), 1257 (1990).

"Experimental observation of negative differential resistance from an InAs/GaSb interface," D.A. Collins, E.T. Yu, Y. Rajakarunanayake, J.R. Söderström, D.Z.-Y. Ting, D.H. Chow, and T.C. McGill, *Appl. Phys. Lett.* 57(7), 683 (1990).

"Modeling of novel heterojunction tunnel structures," D.Z.-Y. Ting, E.T. Yu, D.A. Collins, D.H. Chow and T.C. McGill, *J. Vac. Sci. Technol. B* 8(4), 810 (1990).

"Novel InAs/GaSb/AlSb tunnel structures," D.H. Chow, J.R. Söderström, D.A. Collins, D.Z.-Y. Ting, E.T. Yu and T.C. McGill, SPIE **1283**, pg. 2 *Quantum-Well and Superlattice Physics III* (1990).

"Modeling InAs/GaSb/AlSb interband tunnel structures," D. Z.-Y. Ting, E. T. Yu, D. A. Collins, D. H. Chow, and T. C. McGill, *Computational Electronics*, Kluwer Academic Publishers (Boston) 1990.

Chapter 4

"Experimental observation of large room temperature current gains in a Stark effect transistor," D. A. Collins, D. H. Chow and T. C. McGill, *Appl. Phys. Lett.* 58(15), 1673 (1991).

"High gains observed at room temperature in Stark effect tunneling transistors," D. A. Collins, D. H. Chow and T. C. McGill, *Proceedings of the International Electron Device Meeting, San Fransisco*, Dec. 12-15 (1990).

Chapter 5

"RHEED studies of the growth of InAs/$Ga_{1-x}In_xSb$ strained-layer superlattices," D. A. Collins, T. C. Fu, D. H. Chow and T. C. McGill, *J. Vac. Sci. Tech. B* 10(4), 1779 (1992).

"Type II superlattices for infrared detectors and devices," D. H. Chow, R. H. Miles, J. N. Schulman, D. A. Collins and T. C. McGill, *Semi. Sci. and Tech.* 6(12C), 47 (1991).

Chapter 6

"Investigation of the mixed anion GaSb/InAs heterointerface," M.W. Wang, D.A. Collins, R.W. Grant and T.C. McGill. To be published in J. Vac. Sci. B **11**, July/August (1993).

"RHEED observation of anion exchange reactions on InAs surfaces," D. A. Collins, M.W. Wang, R.W. Grant and T.C. McGill, unpublished.

Publications related to this work but not included in this thesis are as follows:

"Extracting discontinuities in early vision with networks of resonant tunneling diodes," H.J. Levy, D. A. Collins and T. C. McGill, Proceeding of the 1992 IEEE International Symposium on Circuits and Systems, 2041 (1992).

"Interfacial reactions and band offsets values in the AlSb/GaSb/ZnTe material system," E. T. Yu, M. C. Phillips, D. H. Chow, D. A. Collins, M. W. Wang, J. O. McCaldin and T. C. McGill, *Phys. Rev B.*, 46(20), pg. 13379 (1992).

"Characterization of CdSe/ZnTe Heterojunctions," M.C. Phillips, E.T. Yu, Y. Rajakarunanayake, J.O. McCaldin, D.A. Collins and T.C. McGill *J. Crys. Growth* 111(1-4), 820 (1991).

"p-type doping of gallium antimonide grown by molecular beam epitaxy using silicon," T.M. Rossi, D.A. Collins, D.H. Chow and T.C. McGill, *Appl. Phys. Lett.* 57(21), 2256 (1990).

"Measurement of the valence band offset in novel heterojunction systems: Si/Ge (100) and AlSb/ZnTe (100)," E.T. Yu, E.T. Croke, D.H. Chow, D.A. Collins, M.C. Phillips, T.C. McGill and J.O. McCaldin, *J. Vac. Sci. Technol. B* 8(4), 908 (1990).

"Growth of ZnTe and $ZnSe_xTe_{1-x}$ epilayers and superlattices on GaSb," M.C. Phillips, Y. Rajakarunanayake, J.O. McCaldin, D.H. Chow, D.A. Collins and T.C. McGill SPIE **1285**, pg. 158, *Growth of Semiconductor Structures and High-T_c Thin Films on Semiconductors* (1990).

"Band alignment of $Zn_{1-x}Cd_xTe/ZnTe$ and $ZnTe_{1-x}Se_x/ZnTe$ strained layer superlattices," Y. Rajakarunanayake, M.C. Phillips, J.O. McCaldin, D.H. Chow, D.A. Collins and T.C. McGill SPIE **1285**, pg. 142, *Growth of Semiconductor Structures and High-T_c Thin Films on Semiconductors* (1990).

"Optical investigation of the band offset of $Cd_xZn_{1-x}Te/ZnTe$ and $ZnTe_{1-x}Se_x/ZnTe$ superlattices," Y. Rajakarunanayake, M.C. Phillips, J.O. McCaldin, D.H. Chow, D.A. Collins and T.C. McGill, *Mat. Res. Soc. Symp. Proc.* **198**, pg. 427 (1990).

Acknowledgments

My advisor, Professor T.C. McGill is one of the most unique people I have ever met. He is tireless in his quest to provide the resources necessary for his group to continue its research. It doesn't seem fair for Tom to deal with the grunge of fund raising while all we have to do is play with the toys, but no graduate student ever complained about that. Tom provides nearly complete freedom to his students, though he's always ready to help us see "the big picture". While the system may seem a little frustrating at times it does a wonderful job of producing students capable of independent research. In addition, I've enjoyed swapping stories and sharing a few beers with a fellow Scotch-Irishman.

Marcia Hudson deserves the credit for keeping the administrative end of the group functioning. In addition to dealing with P.O.'s and keeping the bureaucrats at bay, she is always cheerful and willing to listen. I'm afraid that Marcia may have spoiled a generation of graduate students. I am also grateful to Sandy Brooks for taking care of numerous rush orders.

I owe huge debts to Drs. David Chow and Jan Söderström who patiently taught me to be a scientist. Besides their obvious talents and deep understanding of semiconductor physics, Dave's generosity and Jan's good humor created a wonderful environment in which to learn and grow. I am especially beholden to Dave for the immense amount of time and effort he cheerfully committed to my education.

A great number of people have contributed to the results presented in this thesis. Drs. David Chow and Jan Söderström used the electrical measurements in Chapter 2 to teach me MBE growth and device processing, while Prof. Mike Jackson performed the optical measurements reported in that chapter. Dr. David Ting and Prof. Ed Yu made the calculations presented in Chapter 3, while Dr.

David Chow contributed to the experimental results. The work in Chapter 3 was the result of the most stimulating and productive period of my graduate career, and I am grateful for the opportunity of working with Drs. Ting and Chow and Prof. Yu. Tracy Fu wrote the computer code used to acquire the RHEED data in Chapter 5, and made a significant contribution to the data analysis. Tracy's code evolved into the computer program used in Chapter 6, so it is doubtful that either chapter would exist without his contributions. In addition, Tracy's enthusiasm and humor were just the right medicine for a slightly cynical senior graduate student. Mike Wang performed the XPS measurements in Chapter 6, and I greatly respect his work ethic and patient nature. Dr. Ron Grant shepherded the XPS measurements and helped with the analysis of the RHEED data in Chapter 6.

Harold Levy, the local dude-speak guru, has been very generous with his time in helping to solve various computer problems. Harold always seems to have a joke or six, ready to ease a bad day, and I will miss his humor when I leave Caltech. Mark Phillips has been a bottomless source of common sense and sarcastic good humor. Johanes Swenberg served as a sounding board at times and helped tremendously with maintaining the clean room. I'll never forget our electrifying experience on a mountain near Bishop. Yixin Liu's unique perspective on the world has been very enlightening, and I hope we can continue to share many profitable experiences in the future. I admire Ron Marquardt's dogged determination as well as his appetite for haggis. I've also enjoyed many fruitful interactions with Shaun Kirby, Chris Springfield, Per-Olov Pettersson, Todd Rossi, George Papa, David Reich and Rob Miles.

I am grateful for the friends who helped keep things in perspective. Biff H., and the camping trips from hell. Bob's beer 'n brots view of life. Ed and Patty's intoxicating zest for life. Pete's enthusiasm for just *about everything.*

Beth and Tom's communist politics. Dave L. for the single-malt, camping and skeet. Andy's jinx. Doug and Debbie for being Scottish. Frankie and Peggy for their mellowness and Frank P. for his calmness. Biff Y. and the kamakazi defense. Jason and Niki for their friendship. Mike and Michael for their good natures. Linda for the housing. Thank you.

Abstract

The material presented in this thesis concerns the growth and characterization of III-V semiconductor heterostructures. Studies of the interactions between bound states in coupled quantum wells and between well and barrier bound states in AlAs/GaAs heterostructures are presented. We also demonstrate the broad array of novel tunnel structures realizable in the InAs/GaSb/AlSb material system. Because of the unique broken-gap band alignment of InAs/GaSb these structures involve transport between the conduction- and valence-bands of adjacent layers. These devices possess a wide range of electrical properties and are fundamentally different from conventional AlAs/GaAs tunnel devices. We report on the fabrication of a novel tunnel transistor with the largest reported room temperature current gains. We also present time-resolved studies of the growth fronts of InAs/GaInSb strained layer superlattices and investigations of surface anion exchange reactions.

Chapter 2 covers tunneling studies of conventional AlAs/GaAs RTD's. The results of two studies are presented: (*i*) A test of coherent vs. sequential tunneling in triple barrier heterostructures, (*ii*) An optical measurement of the effect of barrier X-point states on Γ-point well states. In the first it was found if two quantum wells are separated by a sufficiently thin barrier, then the eigenstates of the system extend coherently across both wells and the central barriers. For thicker barriers between the wells, the electrons become localized in the individual wells and transport is best described by the electrons hopping between the wells. In the second, it was found that Γ-point well states and X-point barrier states interact strongly. The barrier X-point states modify the energies of the well states and increase the escape rate for carriers in the quantum well.

The results of several experimental studies of a novel class of tunnel devices

realized in the InAs/GaSb/AlSb material system are presented in Chapter 3. These interband tunnel structures involve transport between conduction- and valence-band states in adjacent material layers. These devices are compared and contrasted with the conventional AlAs/GaAs structures discussed in Chapter 2 and experimental results are presented for both resonant and nonresonant devices. These results are compared with theoretical simulations and necessary extensions to the theoretical models are discussed.

In chapter 4 experimental results from a novel tunnel transistor are reported. The measured current gains in this transistor exceed 100 at room temperature. This is the highest reported gain at room temperature for any tunnel transistor. The device is analyzed and the current conduction and gain mechanisms are discussed.

Chapters 5 and 6 are studies of the growth of structures involving layers with different anions. Chapter 5 covers the growth of InAs/GaInSb superlattices for far infrared detectors and time resolved, *in-situ* studies of their growth fronts. It was found that the bandgap of superlattices with identical layer thicknesses and compositions varied by as much as 40 meV depending on how their internal interfaces are formed. The absorption lengths in superlattices with identical bandgaps but whose interfaces were formed in different ways varied by as much as a factor of two. First the superlattice is discussed including an explanation of the device and the complications involved in its growth. The experimental technique of reflection high energy electron diffraction (RHEED) is reviewed, and the results of RHEED studies of the growth of these complicated structures are presented. The development of a time resolved, *in-situ* characterization of the internal interfaces of these superlattices is described. Chapter 6 describes the result of a detailed study of some of the phenomena described in chapter 5. X-ray photoelectron spectroscopy (XPS) studies of anion exchange reactions on

the growth fronts of these superlattices are reported. Concurrent RHEED studies of the same physical systems studied with XPS are presented. Using the RHEED and XPS results, a real-time, indirect measurement of surface exchange reactions was developed.

Contents

List of Figures

List of Tables

Chapter 1

Introduction

1.1 Introduction to Thesis

This thesis is concerned with the design, fabrication and characterization of novel semiconductor structures. By building up several layers of material with different electrical and optical properties, a wide range of novel semiconductor systems can be created. In order to create a truly new system, and not a simple superposition of the original subsystems, it is necessary for these layers to be extremely thin. Intuitively these layers would need to be on the order of the wavelengths of the charge carriers and/or light interacting with them. This translates into layers $\sim$10 Å thick For electronic devices and $\sim$1000 Å for optical devices. This process of layering materials with different electrical and optical properties is known as bandgap engineering. This thesis is a study of some of the new devices – and novel physics – that can be explored using semiconductor heterostructures.

The thesis can be divided into two parts. The first (chapters 2, 3 and 4) gives the results of design, growth, processing and characterization of novel tunnel devices. The purpose of this portion was to explore the range of behaviors exhibited by these devices, and to explicitly test our theoretical understanding of them. The second part (chapters 5 and 6) is devoted to understanding and improving the growth of these structures. Typical layer thicknesses in these devices are 10 to 100 Å, while the cubic lattice constants of the materials used range from 5.6 to 6.1 Å. Comparing these two length scales makes clear the level of control over the morphology and chemistry of the internal interfaces necessary to realize these devices. Fluctuations of only a few atomic layers can result in significant changes in device operation.

1.1.1 Summary of Results

The first two chapters of this thesis concern experimental studies of tunneling in semiconductor heterostructures. AlAs/GaAs resonant tunneling diodes (RTD's) are used to probe the interactions between quasi-bound states in coupled quantum wells and the effect of X-point barrier states on Γ-point well states. A series of AlAs/GaAs triple barrier structures were grown and fabricated into devices. By studying electrical transport in these structures, we conclude that if the barrier separating the two quantum wells is thin enough, then coherent electron states extend across both wells and the central barrier. In this case, electrons traveling through the device interact with both quantum wells simultaneously. For thicker barriers, the interaction between the wells decreases until eventually the states in the two wells can be thought of as independent. The electrons in the device become localized in the individual wells, and transport across the structure entails hopping between the wells. A set of double barrier structures were grown and their optical properties measured. By modulating the energy separation between states at the X-point of the AlAs barriers and states at the Γ-point of the GaAs well, interactions between these two type of bound states was studied. We find that the X- and Γ-point states do interact and that the presence of the barrier states have a profound effect on confinement energies in the well and carrier escape times. In addition, we report the first observation of optical transistions that are indirect in both space and momentum.

One of the main results of this thesis is the broad array of tunnel structures realizable in the InAs/GaSb/AlSb material system. This group of nearly lattice matched materials is possibly the optimal one for studying heterojunction devices. It has both type-I and type-II band offsets as well as the unique broken-gap alignment of InAs/GaSb, where the bandgaps of GaSb and InAs do not overlap. Nine distinct types of structures were designed, grown and electrically characterized. Each type had current-voltage curves which displayed negative differential resistance. Over sixty wafers were grown to explore the properties of these different structures. The devices possessed a broad array of electrical characteristics with peak current densities ranging from 15 A/cm^2 to 2×10^5 A/cm^2 and peak-to-valley current ratios ranging from 1.2 to 88. The most novel of these devices are structures where charge carriers move between conduction-band and valence-band states. Because of the unique broken gap band alignment in InAs/GaSb it is possible to study coupling and transport between the conduction- and valence-bands of adjacent layers. These unique structures were found to be fundamentally different from conventional AlAs/GaAs tunnel structures. Experimental studies along with complimentary theoretical studies of this novel class of heterostructures are reported.

A novel tunnel transistor based on the two terminal devices realized in the InAs/GaSb/AlSb material system was designed, grown, fabricated and characterized. Room temperature current gains as large as 100 were observed. This is the highest value reported for any tunnel transistor.

The second portion of this thesis deals with growth issues. *This work was* motivated by both the above tunnel devices and by InAs/GaInSb superlattices which are used as far infrared detectors. We found that the way in which the internal As/Sb interfaces are formed has a dramatic affect on the final bandgap of the detector. Structures with the same layer thicknesses and layer compositions can have bandgaps that differ by 40 meV depending on the details of the interface structure. For devices intended to operate beyond 10 μm, this can result in a significant change in the detector's cutoff wavelength. We have developed a system for characterizing this structure's internal interfaces as they are being formed. We have also developed a real-time technique for indirectly probing surface exchange reactions on the crystal's growth front.

1.1.2 Chapter Outline

Section 1.2 motivates this thesis work. Semiconductor crystal growth is covered in section 1.3. Heterojunctions are covered in section 1.4 including the importance of lattice constants, bandgaps and band offsets to device design. Section 1.5 explains the effect of heterostructures on band structure and discusses quantum confinement effects. The thesis is outlined in section 1.6.

1.2 Motivation

The motivations for studying these novel semiconductor systems are both pure and practical. Semiconductor heterostructures are one of the few areas where basic science and practical technological applications intersect. Among the practical devices dependent on bandgap engineering are visible lasers currently used in optical storage devices and compact disk players[1], infrared lasers which enable communication transmission over optical fibers[2] and solid state oscillators which operate at frequencies approaching 750 Ghz[5]. Fundamental studies which are dependent on heterostructures includes Coulomb blockade structures where the granular nature of electric charge can be observed[4], and investigation of quantum dots and wires[5, 6].

In terms of pure science, this is one of the few physical systems which exhibit room-temperature behavior that can only be described by quantum mechanics. As such, they provide a test bed for theory. The level of theoretical sophistication brought to bear ranges from straightforward application of first year quantum mechanics, which gives a good qualitative description of these devices, to extremely complicated constructions that attempt to account for the 'messiness' present in any physical system. The class of structures described in Chapter 3 is fundamentally different from conventional RTD's. These devices allows us to study a novel class of quantum transport issues.

As mentioned above, there are examples of heterostructure devices currently in use. In a more speculative vein, bandgap engineering could very well be the basis for the next generation of integrated circuits. The current technology of Si based complimentary metal oxide semiconductor (CMOS) devices was invented over 30 years ago. The vast increase in computer power and the sharp drop in price over the last 20 years has been due to constant and gradual refinement of this technology. This process can not continue indefinitely, and many manufacturers believe that shortly after the turn of the century they will have reached the limit of Si CMOS performance enhancement. Semiconductor-based computation will be forced to change course. Among the possible directions are concentrating on developing software to take full advantage of existing technology. A second option is to use Si CMOS in a different way: analog. The overwhelming majority of circuits today are digital, where devices and circuits are designed to force them to occupy one of two states which correspond to '0' or '1'. In this design paradigm, the vast majority of a device's electrical characteristics are ignored.

In analog circuits, the designer attempts to use the full phase space of existing devices and circuits to carry out computation.

The possibility that partially motivates this thesis is a complete design revolution starting with the basic circuit building blocks. Here, the individual devices at the designer's disposal may no longer be simply conventional transistors. To realize this, a wide ranging exploration of novel devices must be completed before settling on the components which could eventually be integrated in a future integrated circuit technology. We believe that a marriage of the devices discussed in Chapter 3 with both conventional and unconventional transistors could prove to be such a basis set. Ongoing work in our group is trying to obtain the final pieces to this puzzle (notably a good insulating layer) and to begin the process of integration.

1.3 Semiconductor Crystal Growth

As mentioned in section 1.1, precise control over a crystal's chemical composition, interface morphology and layer thickness are critical to realization of quantum effect devices. Given these constraints, a flexible, precise method of crystal growth is necessary.

1.3.1 Molecular Beam Epitaxy

Molecular beam epitaxy (MBE) is a physical vapor deposition technique where the constituent atoms of a crystal are directly deposited onto a substrate. If the fluxes and substrate temperature are correctly chosen, single crystal, thin films result. The growth fluxes are produced by evaporating ultrapure elemental or compound source materials with typical growth rates of 1 to 3 Å per second. Each of the source ovens can be individually shuttered in order to change the beam composition. Monolayer precision can routinely be achieved with MBE, and growth of nearly all of the most common III-V, II-VI and group IV semiconductors has been demonstrated.

Crystal growth is done in an ultra high vacuum (UHV) chamber with base pressures $\sim 10^{-10}$ Torr, where hydrogen is the largest typical background gas. Because of these low pressures, the mean free paths of the material in the growth beams is much larger than the separation between oven and substrate. As a result, liquid or gaseous flow patterns do not complicate MBE growth as can be the case in chemical vapor and liquid deposition techniques.

Fig. 1.1 shows the layout of a typical MBE chamber. It consists of stainless steel walls enclosing a growth volume of roughly a cubic meter. Nestled inside the chamber walls are hollow panels. During growth, liquid nitrogen is pumped through them to further reduce the base pressure. Our chamber is equipped with five effusion cells. Three of the cells hold group III material (Ga, Al, In) and two hold dopants (Si and Ge). Two cracker cells are used to produce As and Sb. These cells consist of two thermally isolated regions. In the first region, either As_4 or Sb_4 is sublimated off of a bulk charge. The cracking zone can be adjusted to be as much as 800 °C hotter than the sublimator. In the cracking zone, the group V species can be adjusted by cracking the tetramers down to dimers or monomers. Since the two zones are thermally isolated, adjusting the temperature of the cracker does not change the absolute group V flux. The flexibility of MBE is demonstrated by the fact that over 20 different compounds can be grown in this single chamber.

Two *in situ* analysis techniques are typically available on MBE chambers. Reflection high energy electron diffraction (RHEED) is a method for analyzing the surface structure of the substrate. RHEED will be covered in some detail in section 5.3.1, but suffice to say that growth rates, surface reconstructions and

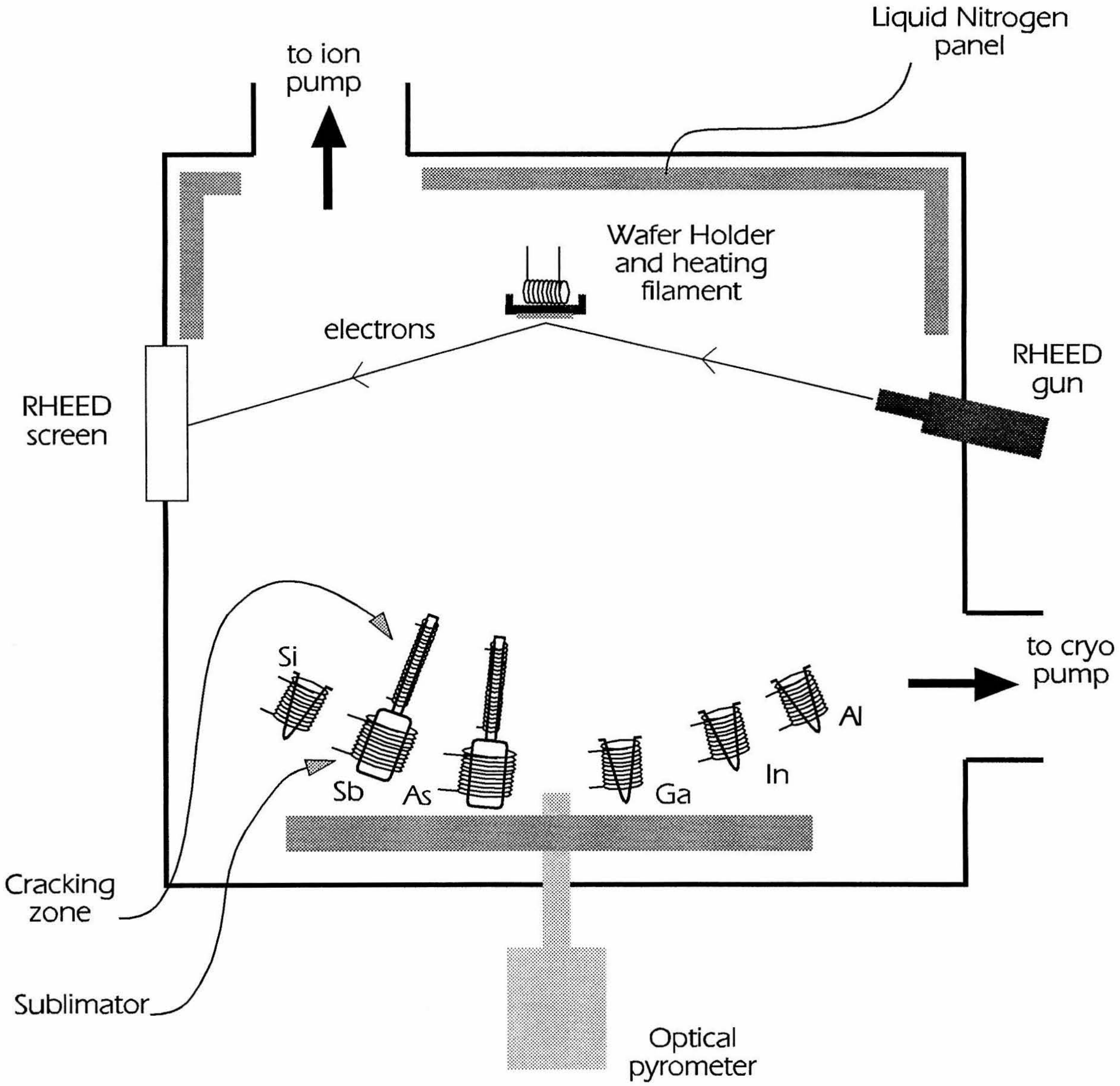

Figure 1.1: Layout of a typical MBE chamber.

surface morphology can be obtained with it. As the sketch in Fig. 1.1 shows, the RHEED geometry does not interfere with the beams fluxes so the wafer's surface can be analyzed during growth. Residual gas analyzers give information about the gaseous species present in the growth chamber and can be used to adjust beam fluxes and identify background impurities.

Given the assumption of UHV growth conditions, MBE is conceptually simple. In essence, there are only two variables that the grower can adjust: the growth fluxes and the substrate temperature. These two variables control the stoichiometry of the growth front and the surface mobility of physisorbed atoms which together determine the properties of the resulting epilayer. In general, substrate temperatures are as high as possible with the upper limit being determined by either the congruent sublimation temperature of the thin film or the temperature where bulk mobilities lead to interdiffusion of the individual layers. Given the substrate temperature, the incident fluxes are adjusted to achieve the proper stoichiometry at the growth front. The flexibility and conceptual simplicity of MBE make it an ideal tool to explore a wide range of novel semiconductor structures.

Fig. 1.2 is a schematic of the UHV growth system in the McGill lab. It consists of three separate growth chambers (III-V, II-VI and Si/Ge), a surface analysis chamber, a metallization chamber and a substrate heating and cleaning chamber. The chambers are connected by UHV transfer tubes so that wafers may be transferred between them without being exposed to atmosphere. This is done routinely. All of the heterostructures discussed in this thesis were grown in the III-V chamber shown in Fig.1.2.

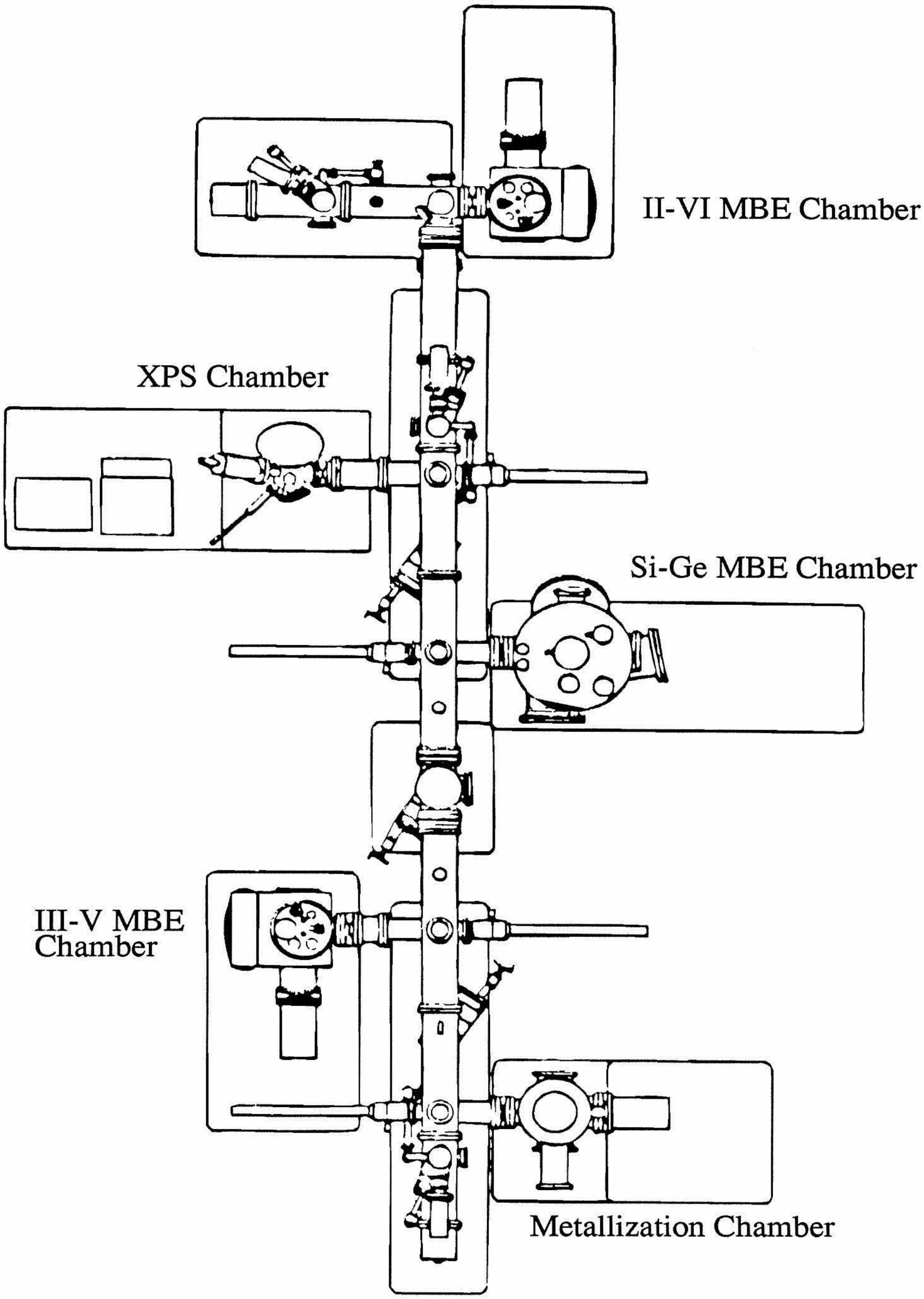

Figure 1.2: Schematic diagram of the MBE growth system. The system consists of separate III-V, II-VI and Si/Ge growth chambers and surface analysis and metallization chambers interconnected by UHV transfer tubes.

1.3.2 III-V Crystal Growth

While the growth conditions for each individual semiconductor is different, III-V materials share many general features. All III-V compounds preferentially desorb group V atoms. As a result, between three and ten times as many group V as group III atoms must be evaporated to grow a stoichiometric crystal. In addition, at growth temperatures, a constant group V flux is necessary to stabilize the surface. The group III flux controls the growth rate. At growth conditions, the group III ovens are 900 to 1200 °C depending on the specific materials being evaporated, while typical substrate temperatures are 400 to 700 °C. Because of this, the group III's have unity sticking coefficients; hence, their arrival rate determines the growth rate. III-V's exposed to atmosphere form a thin native oxide which must be removed before growth. This is done by heating the substrate to near its congruent sublimation temperature in a group V flux. Typically the oxide desorbs in two steps. The group V oxides desorbs first while at higher temperatures the group III oxides disassociate and the freed oxygen desorbs. Both RHEED and RGA give signatures for the desorption. The oxide desorption temperature is well defined, and is used to calibrate substrate temperatures.

The structures studied in this thesis consisted of $\mathrm{Al}_x\mathrm{Ga}_{1-x}\mathrm{As/GaAs}$, $\mathrm{InAs/Al}_x\mathrm{Ga}_{1-x}\mathrm{Sb}$ and $\mathrm{InAs/Ga}_x\mathrm{In}_{1-x}\mathrm{Sb}$ heterostructures. The growth conditions of the individual structures are given in the appropriate chapters. In general, their relative growth temperatures are:

$$InSb < InAs < GaSb \approx AlSb < GaAs \approx AlAs$$

As a result, the optimal As to group III to ratio is smaller for InAs than for either GaAs or AlAs. The sticking coefficient of Sb is much higher than that of As, hence the optimal group V to group III ratio is smaller for antimonide layers than arsenide layers. When layering materials with different optimal substrate temperatures, an intermediate temperature is chosen. The growths rates and flux ratios are then adjusted to compensate

1.4 Heterojunctions

The work in this thesis is based on the concept of bandgap engineering. Here, structures consisting of thin layers of dissimilar materials are grown to achieve novel optical and electrical properties. In order to design and realize an interesting heterostructure, a basic understanding of the relevant material properties is necessary. The most important of these are the lattice constant and bandgap of the individual materials, and the band offsets between materials.

1.4.1 Lattice Constants

Fig. 1.3 is a plot of bandgap vs. lattice constant for several common semiconductors. The crystal structure of each consists of intertwined face-centered cubic lattices. In Si and Ge, all of the atoms are identical resulting in diamond's crystal structure. For the compound materials the individual atomic species are located on the separate sublattices, resulting in a zincblend crystal structure*. When layering materials with different lattice constants, the material in the overlayer initially grows strained to the underlying layer. In the growth plane, the atoms in the two materials register. This distorts the overlayer which will adjust its lattice constant along the growth direction in an attempt to keep the volume of its unit cell constant. This imparts strain energy to the crystal, which if suffi-

---

*Note that the lattice constant used in Fig. 1.3 is the cubic lattice constant. For compound semiconductors it is common to quote the monolayer size which is the separation, projected onto one of the (100) crystal axes, between like atomic species. This distance is one half of the cubic lattice constant.

ciently large, will nucleate dislocations in the overlayer. If enough dislocations are present, the overlayer will relax to its natural lattice constant. Dislocations can scatter carriers and serve as recombination sites, hence their presence must be avoided, especially in minority carrier devices. In addition, strain modifies the crystal bandstructure which is critical to the operation of some devices. The thickness at which dislocations are generated depends on the elastic constants of the specific material. In general, the critical thickness decreases quite rapidly as the lattice mismatch between two materials increases. For mismatches of 1%, critical thicknesses are on the order of 1000 Å . As a result, it is important to choose materials that are very nearly lattice matched. As Fig. 1.3 shows, the lattice constants tend to cluster around 5.65 and 6.1 Å , making materials with these lattice parameters particularly suited to heterostructure investigation.

1.4.2 Bandgaps

The second important material parameter is the bandgap. For optical applications, the appropriate bandgap is obviously critical. For electrical applications, narrow gap materials are preferable. In general, the effective mass of a semiconductor scale inversely with the bandgap, hence narrow gap materials tend to have smaller effective masses and larger carrier mobilities. In the particular case of III-V's, the surface Fermi level tends to pin in the bandgap, one third of the way from the valence band. This gives a typical electron Schottky barrier of two thirds of the bandgap and a hole barrier roughly equal to one third of the bandgap. The smaller Schottky barriers typical of narrow gap materials facilitates the fabrication of ohmic contacts. Therefore, as long as optical constraints do not force the choice of a particular semiconductor, the materials clustered at a lattice constant of 6.1 Å are the logical choice to use when investigating

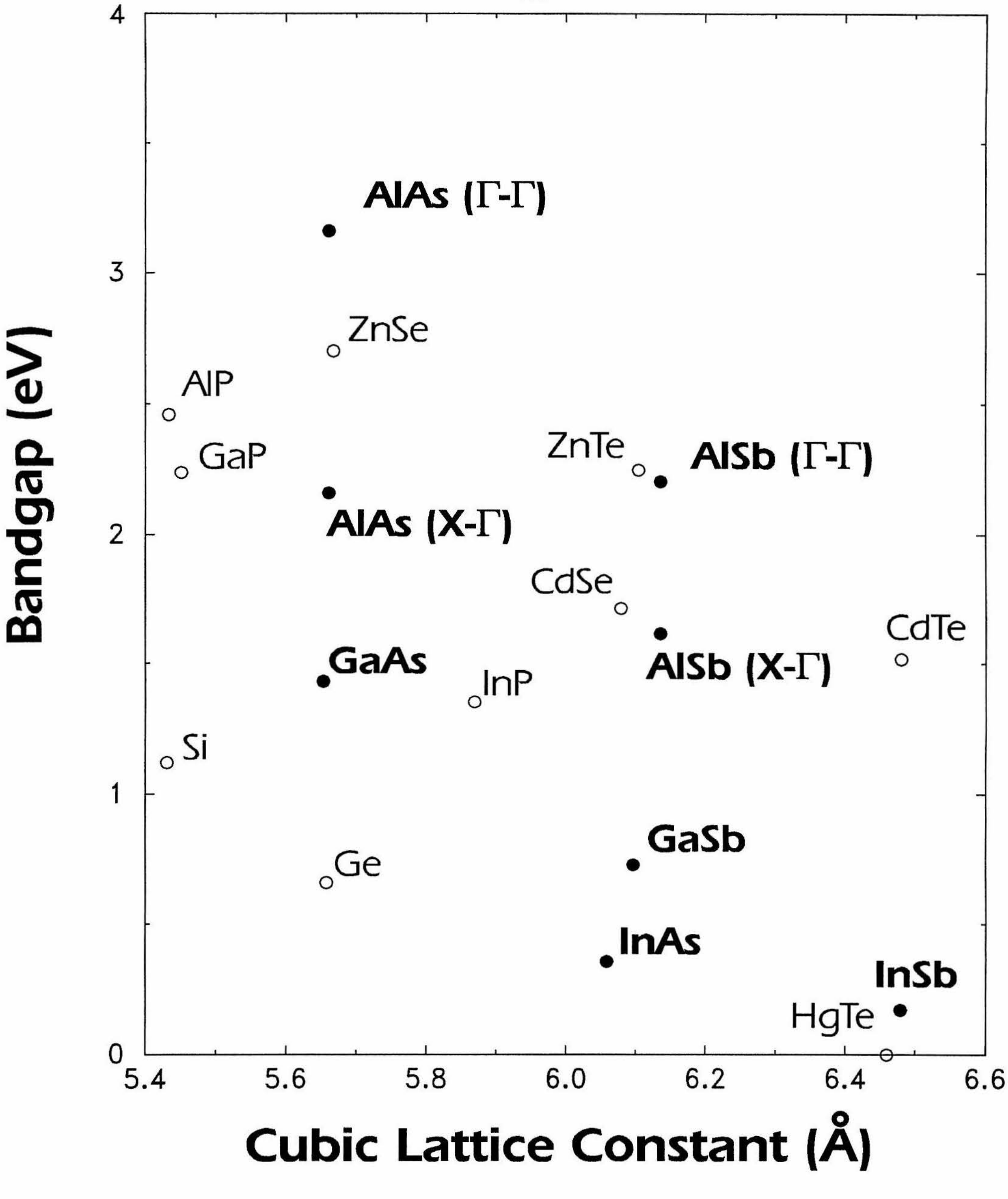

Figure 1.3: Plots of cubic lattice constant versus bandgap for several common semiconductors. The data shown in bold were investigated for this thesis. The parentheses attached to some of the materials denote whether the quoted bandgap is conduction-band Γ-point or conduction-band X-point to valence-band Γ-point separation in energy.

heterostructures. Not only is there a wider range of available bandgaps, the narrow gaps of InAs and GaSb suggest superior electrical performance compared to the materials clustered at 5.65 Å. InAs also has a negative Schottky barrier for electrons hence good ohmic contacts can be fabricated.

1.4.3 Band Offsets

When two materials with different bandgaps are placed next to each other, a discontinuity occurs in either the valence- or conduction-bands, or both. To first order, where the band discontinuity occurs and what its magnitude is can be estimated from the work functions of the two materials, though experimental measurements are necessary for actual device design. These band edge discontinuities are used to create potential barriers for carriers which can lead to quantum confinement effects. For some applications, certain band alignments are crucial, e.g., injection of a particular carrier type. In general, though, systems with the greatest range of band offsets are best suited to the study of heterostructures. This again points to the materials clustered near 6.1 Å. In addition, InAs and GaSb have a unique band offset in that their bandgaps do no overlap. This allows the investigation of a novel set of heterostructures which involve transport between the valence- and conduction-bands of adjacent layers.

The materials studied in this thesis are marked with closed circles in Fig. 1.3. As argued above, the cluster of materials with lattice parameters near 6.1 Å are particularly interesting, and the bulk of this thesis concentrates on them. Though no III-V/II-VI devices were grown, integrating them into the reported heterostructures can only increase the richness of structures obtainable in this nearly lattice matched material system.

1.5 Band Structure and Quantum Confinement in Heterostructures

Fig. 1.4 is a series of drawings intended to describe the effects of band edge discontinuities on heterostructure band structure. Fig. 1.4 (a) is a physical representation of a double barrier device. It consists of a thin layer of undoped GaAs, sandwiched between layers of undoped AlAs, between two doped GaAs electrodes. Layering two materials with different bandgaps modulates the potential seen by electrons and holes. In the case of GaAs/AlAs heterostructures, AlAs presents a barrier to both holes and electrons in GaAs. As a result, the carriers in the central GaAs layer in Fig. 1.4 (a) are in a potential well. If the GaAs layer is thin enough, then carriers in the well will simultaneously interact with both barriers. The length scale at which this occurs is on the order of 100 Å . When this happens the eigenstates in the well become quantized. Conceptually, the system is similar to the classic problem of a particle in a box covered in first year quantum mechanics.

Fig. 1.4 (b) is a sketch of the conduction-band energy diagram for an AlAs/GaAs double barrier. The continuous solid line represents the conduction-band minimum and the central solid lines bound well states. In this case the potential barriers that form the well have finite height, so the bound state probability density will leak into the barriers. The amplitude of a state's probability density decays exponentially with barrier thickness. For sufficiently thin potential barriers, the well state has a nonzero amplitude in the outer GaAs electrodes. When this happens the bound, well state can couple to continuum electrode states and transport between the electrodes and well can occur. Such a state is termed a quasi–bound state (QBS). Fig. 1.4 (c) sketches the amplitudes of the two lowest

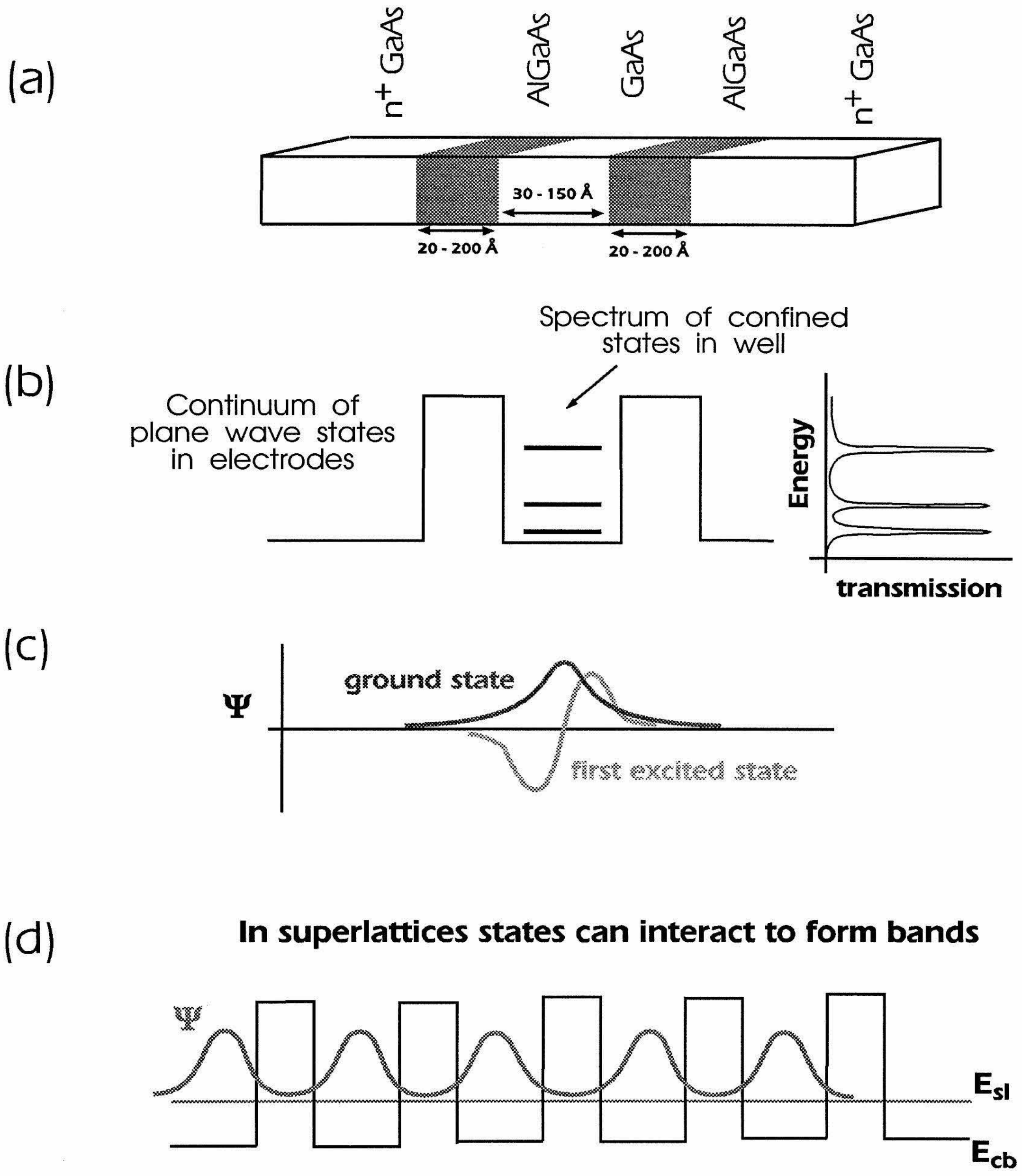

Figure 1.4: Quantum confinement in heterostructures.

states. Notice that both are nonzero in the AlAs barriers.

Now consider transport through the well states. Since the QBS energy is quantized, only electrons of a particular energy can elastically tunnel into the well. Transmission of electrons with energies that don't match that of the bound state are strongly suppressed. This leads to peaks in the electron transmission probability at QBS energies. This is represented in the sketch on the right hand side of Fig. 1.4 (b). In essence, the well acts as an energy filter on the incident electrons. When an electrical bias is applied across the device, the transmission resonances due to the confined well states can lead to current resonances. In high quality structures, these current resonances can be seen at room temperature.

The quantum confinement described above can also change the optical properties of the crystal. Due to the confinement energy, emission from the well region occurs at an energy higher than the bandgap of the bulk semiconductor. Likewise, the threshold at which the bound well state absorbs optical energy is modified by the quantum confinement. Fig. 1.4 (d) shows the the effect of butting several quantum wells up against each other. As in the case of a single well, if the barrier layers are thin, the confined states in the individual wells will leak out. If the states interact strongly enough, they will form an energy band. The new eigenfunctions of the system will be plane-wave like states with a fixed crystal momentum perpendicular to the barriers.

1.6 Thesis Outline

Chapter 2 covers tunneling studies of conventional AlAs/GaAs RTD's. A quick review of the theoretical basis of RTD's is presented. Then the growth, fabrication and characterization of these devices is discussed. The results of two studies are then presented: (*i*) A test of coherent vs. sequential tunneling in triple barrier heterostructures, (*ii*) An optical measurement of the effect of barrier X-point states on Γ-point well states.

The results of several experimental studies of a novel class of tunnel devices are presented in Chapter 3. These interband tunnel structures involve transport between conduction- and valence-band states in adjacent material layers. These devices are compared and contrasted with the conventional RTD's discussed in Chapter 2. Experimental results are presented for both resonant and nonresonant devices. These results are compared with theoretical simulations, and necessary extensions to the theoretical models are discussed. Finally, a summary of the experimental results and some rules-of-thumb for understanding this class of devices is presented.

In Chapter 4 experimental results from a novel tunnel transistor are given. The measured current gains in this transistor exceed 100 at room temperature. This is the highest reported gain at room temperature for any tunnel transistor. The device is analyzed and the current conduction and gain mechanisms are discussed.

Chapters 5 and 6 are studies of the growth of structures involving layers with different anions. Chapter 5 covers the growth of InAs/GaInSb superlattices for far infrared detectors and time resolved, *in-situ* studies of their growth fronts. First the superlattice is discussed including an explanation of the device and the complications involved in its growth. The experimental technique of RHEED is reviewed. The results of RHEED studies of the growth of these complicated structures are then presented. The development of a time resolved, *in-situ* characterization of the internal interfaces of these superlattices is described. Chapter 6 describes the result of a detailed study of some of the phenomena described in Chapter 5. X-ray photoelectron spectroscopy (XPS) studies of anion exchange reactions on the growth front of these superlattices are reported. Concurrent

RHEED studies of the same physical systems studied with XPS are presented. Using the RHEED and XPS results, a real-time, indirect measurement of surface exchange reactions was developed.

References

[1] A. Valster, J. Vanderheijden, M. Boermans and M. Finke, *Philips Jour. of Res.*, **45(3-4)**, 267 (1990).

[2] Y. Miyamoto, K. Hagimoto, F. Ichikawa, M. Yamamoto and T. Kagawa *Elec. Lett.*, **27**, 853 (1991).

[3] E.R. Brown, J. R. Söderström, C.D. PArker, L.J. Mahoney, K.M. Molvar and T.C. McGill, *Appl. Phys. Lett.*, **58**, 2291 (1991).

[4] J.E. Mooij and L.J. Geerligs, *Physica B*, **169** 32 (1991).

[5] J. Christen, E. Kapon, M Grundmann, D.M. Hwang, M. Joschko and D. Bimberg, *Physica B* **173**, 307 (1992).

[6] L. Eaves, *Nature*, **357**, 540 (1992).

Chapter 2

GaAs/AlAs Tunnel Structures

2.1 Introduction and Outline

The work covered in this chapter is slightly removed from the bulk of the thesis work which concentrated on mixed anion As/Sb heterostructures. The work in this chapter was undertaken as an introduction to the basic concepts of tunneling in heterostructures, MBE crystal growth and device processing and characterization. As a result the conceptually simpler AlAs/GaAs systems was investigated first. Likewise, because these crystals are composed of a single variety of anion, their growth and processing are more straightforward.

A brief overview of tunneling in heterostructures is covered in section 2.2. Section 2.3 covers the growth of GaAs/AlAs heterostructures. Results of electrical measurements of triple barrier devices are reported in section 2.4. Section 2.5 reports on optical measurements of the role of X-point states in tunneling. The chapter is summarized in section 2.6.

2.2 Tunneling in Heterostructures

A complete treatment of tunneling in heterostructures is beyond the scope of this thesis. However, an intuitive understanding of tunneling in necessary for understanding this and the following chapters.

Fig. 2.1 is a series of drawings intended to describe resonant tunneling. Fig. 2.1 (a) is a physical representation of a tunnel diode while below it is a sketch of the devices' bandedge profile. Fig. 2.1 (b) is a sketch of the conduction-band energy diagram for an AlAs/GaAs double barrier. The continuous solid line represents the conduction-band minimum, the central solid line, a bound well state and the grey line, the probability density in the well. As mentioned in Chapter 1, AlAs presents a barrier to both holes and electrons in GaAs. This leads to the formation of a spectrum quasi–bound states (QBS) in the GaAs well.

Now consider transport through the well states. Since its energy is quantized, only electrons of a particular energy can elastically tunnel into the well. Transmission of electrons with energies that don't match that of the bound state are strongly suppressed. This leads to a peak in the electron transmission probability at the QBS energy. This is represented in the sketch on the right hand side of Fig. 2.1 (b). In essence, the well acts as an energy filter on the incident electrons. When an electrical bias is applied across the device, the energy difference between the well QBS and the electrode Fermi level is changed. When the electrode Fermi level and QBS do not coincide, the device is very resistive due to the energy filtering of the quantum well. For biases that bring the Fermi level into resonance with the well state, the device is very conductive since the electrode electrons now have elastic access to the well state. This is represented in Fig. 2.1 (c). Past resonance the device again becomes resistive because they are no longer on the peaked portion of the transmission curve. This modulation of the device

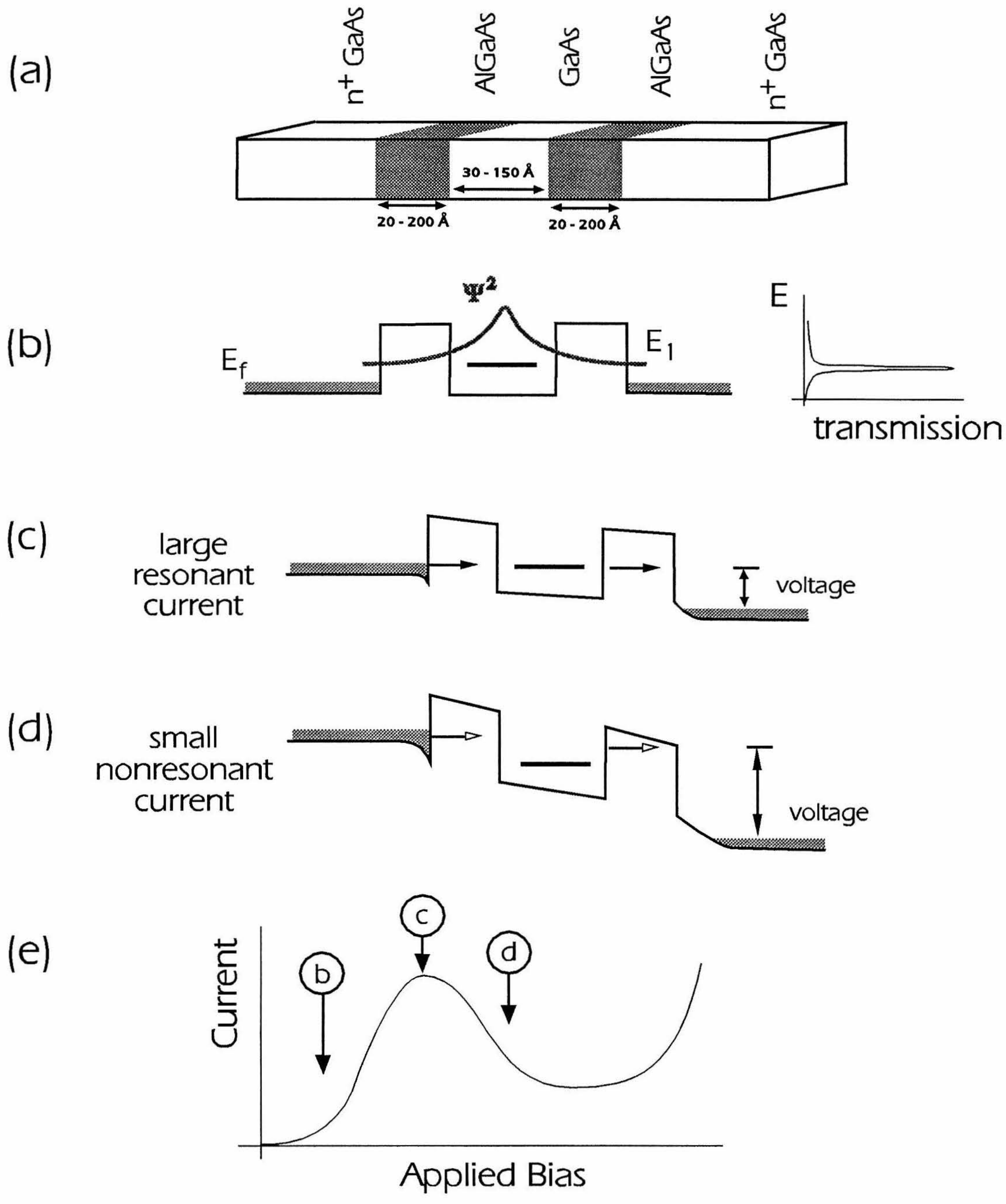

Figure 2.1: Resonant tunneling in a double barrier heterostructure.

resistance leads to a region of negative differential resistance (NDR) as sketched in Fig. 2.1 (e).

2.3 AlAs/GaAs Growth

All of the samples reported here were grown on (100) GaAs substrates. The substrates were successively immersed in warmed solvents – trichloroethane, acetone, isopropyl and deionized water – to remove organic contaminates from their surfaces. The substrates are then etched in 5:1:1, H_2SO_4:H_2O_2:H_2O for two minutes. This removes approximately 10 μm of material from the surface, eliminating any polish damage or near surface contamination that may be present. Following the etch, the wafers are cleaved and indium bonded to molybednum blocks. The wafers are then introduced into the MBE growth system via a load lock.

All of the samples were grown in a Perkin-Elmer 430 molecular beam epitaxy (MBE) system. The substrates are brought into the MBE chamber and heated in an As flux to remove the native oxide that forms when exposed to atmosphere. Oxide desorption is confirmed by monitoring the reflection high energy diffraction (RHEED) pattern from the crystal's surface. When the oxide desorbs, the RHEED pattern changes from a uniform background with a few diffraction spots, characteristic of the thin amorphous oxide layer, to a set of bright, streaky spots on a black background. The change in the RHEED pattern occurs at substrate temperatures of 600 °C and is used to calibrate the optical pyrometer and thermocouple used to measure the substrate temperature. Monitoring the residual gas analyzer (RGA) gives a warning that the oxide is about to desorb. Just prior to desorption, large bursts of CO and CO_2 from the oxide layer are observed on the RGA. These peaks fall back to their background levels after oxide removal.

At least 1 μm of GaAs is deposited before growing the active region of the device. This ensures optimal crystal quality and that no contaminants from the oxide incorporate in the active region. The devices in this chapter were grown at a nominal substrate temperature of 600 °C as calibrated by the oxide desorption point. It has been reported that higher quality AlAs and $\mathrm{Al}_x\mathrm{Ga}_{1-x}\mathrm{As}$ can be obtained at higher substrate temperatures. However, because of the short time needed to grow these thin layers, it was not possible to adjust the substrate temperature fast enough. To compensate for the lower substrate temperatures, the AlAs layers were grown more slowly than the GaAs layers: 0.25 μm for AlAs and 1.0 μm for GaAs. Lowering the AlAs growth rate partially compensates for the nonoptimal substrate temperature by giving the Al atoms more time to diffuse across the wafers surface before being buried by subsequent layers of material.

The GaAs layers were grown with an As-terminated growth front as determined by the 2×4 RHEED reconstruction. It is believed that the highest quality GaAs is that grown with slightly more As than necessary to maintain the 2×4 RHEED reconstruction. The ratio of the As and Ga peaks on the RGA was calibrated to the 2×4 to 4×2 reconstruction transition characteristic of the transition between an As terminated and a metal rich GaAs surface. Before growth, the As flux is adjusted to obtain the proper As to Ga ratio on the RGA. The same As flux was used for both the GaAs and AlAs layers since the thermal time constant of the bulk As evaporator is several tens of minutes. Since the congruent sublimation temperature of AlAs is higher than that of GaAs, a smaller As flux would probably be sufficient to stabilize the AlAs surface. This partially explains the improved AlAs layer quality observed at higher substrate temperatures.

The AlAs and GaAs growth rates were determined by a variety of methods. A tantalum wire was stretched across a portion of each substrate. This masked the substrate from the beam flux and created a trench in the epilayer. The trench depth was measured with a stylus profilometer. This allowed *determination of* the GaAs growth rate. RHEED intensity oscillations were also used to measure both the AlAs and GaAs growth rates. A computer program was written which digitizes a video signal of the RHEED pattern. The computer program automatically locates the specular RHEED spot and tracks any changes in its intensity. The program is able to deliver growth rates in real time from both stationary and rotating substrates. It was found that the growth rates obtained by RHEED were approximately 10% faster than those obtained by the shadow mask method. This was attributed to thermal transients in the source ovens due to shutter actuation. To correct this, 7/8 inch spacers were installed on the MBE chamber to increase the distance between the shutters and the ovens. This reduced the discrepancy between the growth rates to roughly 2%. The final method for determining the growth rate used x-ray diffraction. Two types of samples were prepared. AlAs/GaAs superlattices were grown and the superlattice period and the position of the zeroth order superlattice peak was measured. From the period, the total amount of material deposited is determined, while the position of the zeroth order superlattice peak gives the average atomic spacing in the superlattice which can be related to the average composition. Bulk AlGaAs layers were also grown. Since AlAs and GaAs have slightly different lattice constants, measuring the lattice constant of the alloy layer gave the ratio of the AlAs to GaAs growth rates. Interference fringes characteristic of the thickness of the AlGaAs layer were used to determine the thickness of the alloy film. The individual AlAs and GaAs growth rates could then be determined.

2.4 Triple Barrier Heterostructures

2.4.1 Sequential vs. Coherent Tunneling

Since the initial proposal[1] and demonstration[2] of resonant tunneling in semiconductor heterostructures, a large body of theoretical and experimental work has been aimed at understanding the relevant current transport mechanisms. One of the major unresolved issues is how the tunneling process that gives rise to negative differential resistance (NDR) should be treated. The early consensus was that the NDR seen in double barrier heterostructures was due to a resonant enhancement of the structure's transmission coefficient, analogous to the enhancement seen in the transmission of optical waves in a Fabry-Perot intefer-ometer. Recently, sequential processes, wherein the electrons tunnel through the individual barriers making up a double barrier structure in *independent* steps, have been proposed. It was suggested that the NDR seen in such structures was due solely to tunneling from a three dimensional system into a two dimensional system, with no need for a resonant enhancement of the structure's overall transmission coefficient.[3, 4] The major difference between these two pictures is the length scale over which the electronic wavefunction is coherent. In the first model the electrons traversing the device interact with the entire heterostructure simultaneously, while in the second it is assumed that scattering processes limit the spatial coherence of the electron's wavefunction so that it interacts with the various layers of the heterostructure individually.

In this section we examine the electron wavefunction coherence between two quantum wells. A series of double quantum wells separated by barriers of varying widths were grown. The devices' conduction band edge profile is shown in Fig. 2.2(a). In interpreting our current-voltage measurements we will consider two cases: coherence and incoherence in the electronic wavefunctions across the central barrier. If the wavefunctions in the two quantum wells are uncorrelated, NDR due to elastic tunneling can occur only if the Fermi level in the source electrode simultaneously lines up with the independent quasi-bound states in both the first and second quantum well. This coincidence does not generally occur except for a few specific choices of layer thickness. On the other hand, if the quasi-bound states in the two wells extend coherently across the middle barrier, the electrons interact with the entire structure as a whole, leading to multiple current resonances.

2.4.2 Experimental

Four structures were grown. Three consisted of two 54 Å quantum wells separated by a middle barrier of widths 3, 6 and 12 monolayers (ML). The fourth structure was a standard double barrier diode with a 108 Å well. In all four structures the outer barriers were 30 Å thick. Spacer layers consisting of 25 Å of undoped GaAs and 500 Å of GaAs Si-doped at 2x10^{16} cm^{-3} were grown on both sides of the active region to inhibit the diffusion of silicon atoms from the degenerately doped electrodes into the triple barrier region.[5] Device mesas with a surface area of 9.2×10^{-5} cm^2 were fabricated using photolithography and a wet etch. Current-voltage (I-V) curves were measured at 300 K and 77 K using an HP 4145A semiconductor parameter analyzer.

In Fig. 2.2 we display typical I-V curves taken at 77 K for the double barrier and the samples with 3 and 12 ML middle barriers (Fig. 2.2(b), (c) and (d), respectively). The samples showed as many as three distinct NDR regions, with the number and intensity of the current resonances decreasing for the sample with the thickest middle barrier. Fig. 2.3 shows the temperature dependence of the I-V curves of the structure with a 3 ML middle barrier. The PVR and, to a lesser extent, the peak current density are strong functions of temperature. The behavior shown in the figure is representative of all the devices investigated.

2.4.3 Electrical Characteristics vs. Middle Barrier Thickness

In Fig. 2.4 we plot the measured peak current densities of the second resonance versus middle barrier thickness. We show the data for the second peak only since it is present for all middle barrier thicknesses (for the 12 monolayer sample there is only one current resonance, but we designate it as the "second" peak on the basis of the applied bias at which it occurs). To show the range of device performance, we plot a cluster of points for each heterostructure corresponding to different devices on the same wafer. Within the range of samples, the current is only slightly affected when the middle barrier is introduced and actually increases when the thickness is increased from 3 ML to 6 ML even though the applied bias at which the second resonance occurs is very nearly the same. For the 6 ML sample, the total thickness of the structure's barriers has been increased by over 25% . If the electronic wavefunctions in the device do not extend coherently across the central barrier, the electrons would tunnel through each barrier separately and the current should decrease for thicker middle barriers rather than remaining constant as our data show. The data indicate that the thin central barrier modifies the position in energy at which the transmission resonances occur, but does not affect the probability for an electron to tunnel across the entire heterostructure.

Fig. 2.5 shows the range of measured peak-to-valley current ratios (PVR) at 77 K for the second peak versus middle barrier thickness. As in Fig. 2.4 the plotted points show the variation in device performance. The PVR shows

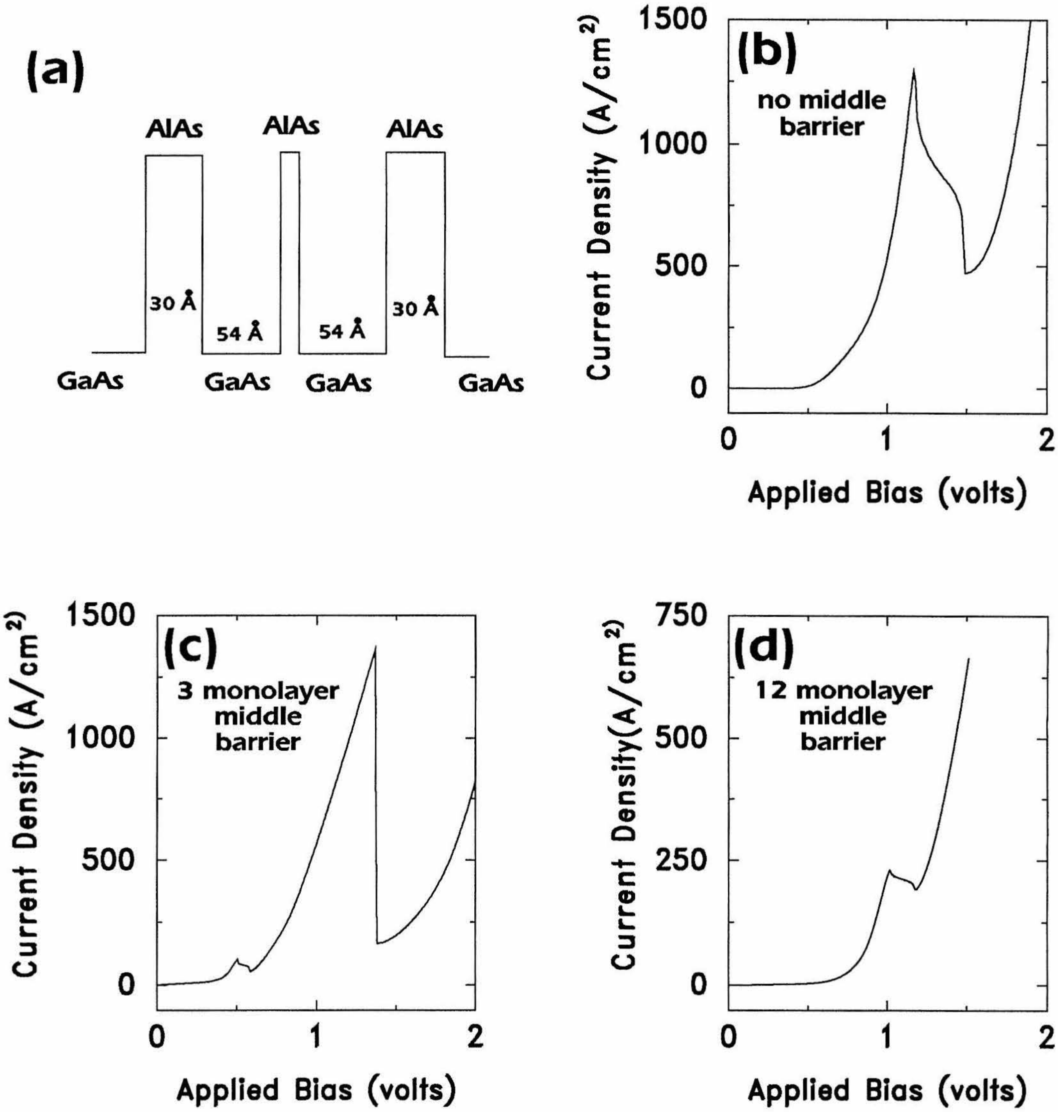

Figure 2.2: Conduction band edge profile and typical I-V curves taken at 77 K. A) Conduction band edge at zero bias. B) I-V curve for single well structure. C) I-V curve for a double well structure with a 3 ML middle barrier. D) I-V curve for a double well structure with a 12 ML middle barrier. There is a resonance at low bias in the I-V curve of Fig. (b) which is obscured by the figures' scale.

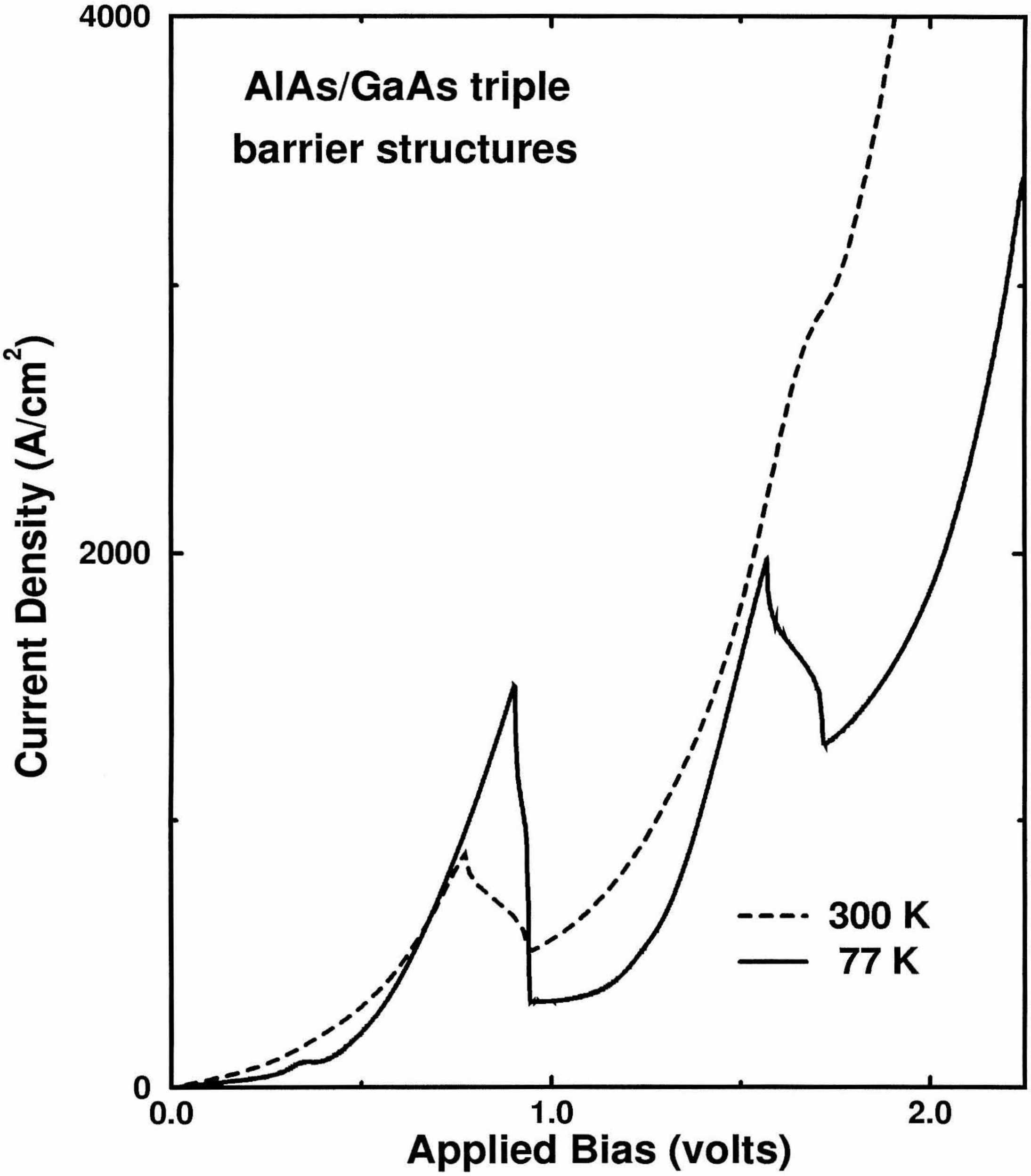

Figure 2.3: Current-voltage curves as a function of temperature. The curves were measured on a device with a 3 monolayer middle barrier. The dependence shown is representative of all the devices.

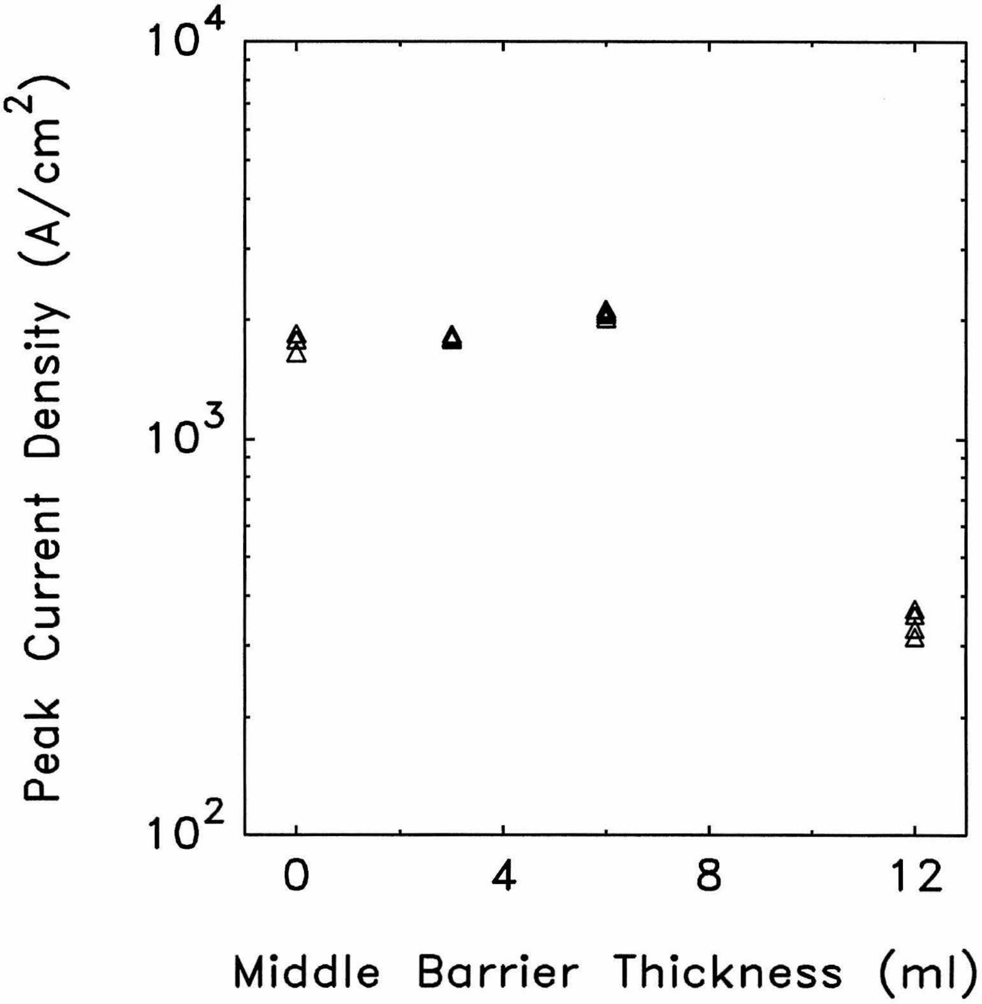

Figure 2.4: Current densities in the second peak versus middle layer thickness at 77 K. The plotted points represent the range of measured values.

a substantial increase when the 3 ML middle barrier is introduced and remains fairly constant when the barrier thickness is doubled. When the middle barrier thickness is increased to 12 ML, the PVR's drop sharply, indicating that different current transport mechanisms become important. For this sample the middle barrier is thicker than the first and third barriers and the I-V curves showed only one peak (see Fig. 2.2 (d)). The loss of two of the current resonances at the same central barrier thickness at which the peak current densities (see Fig. 2.4) and PVR's (see Fig. 2.5) drop dramatically indicates that phase coherence between the wells has been lost. With a thick AlAs barrier separating the wells, the low lying quasi-bound states no longer extend across both wells but are becoming more localized in the individual wells. (Our calculations show that in the sample with the 12 ML central barrier under an applied bias of 350 mV, over 98% of the probability density is located in a single well for the various calculated quasi-bound levels in the system.) Further, recent measurements have shown that tunneling times depend exponentially on the barrier thickness[6]. As the middle barrier thickness increases, the time for electrons to tunnel across the entire structure increases, enhancing the probability that scattering will randomize the phase of the electron's wavefunction as it traverses the heterostructure.

A summary of the measured resonance-peak voltages along with the calculated values is given in Fig. 2.6. The plotted points show the range of measured values, and the solid line shows the calculated positions of the first resonance. For the calculation, a resonance was said to occur when the energy of a quasi-bound state, with an appreciable probability density in both of the quantum wells, matches the Fermi energy in the source electrode. The energies of the resonant states in the biased heterostructure are computed with a one-band Wannier orbital model[7]. Spatial variations in the potential due to fixed and mobile charges were included; charge buildup in the wells was assumed to be small. The conduction band

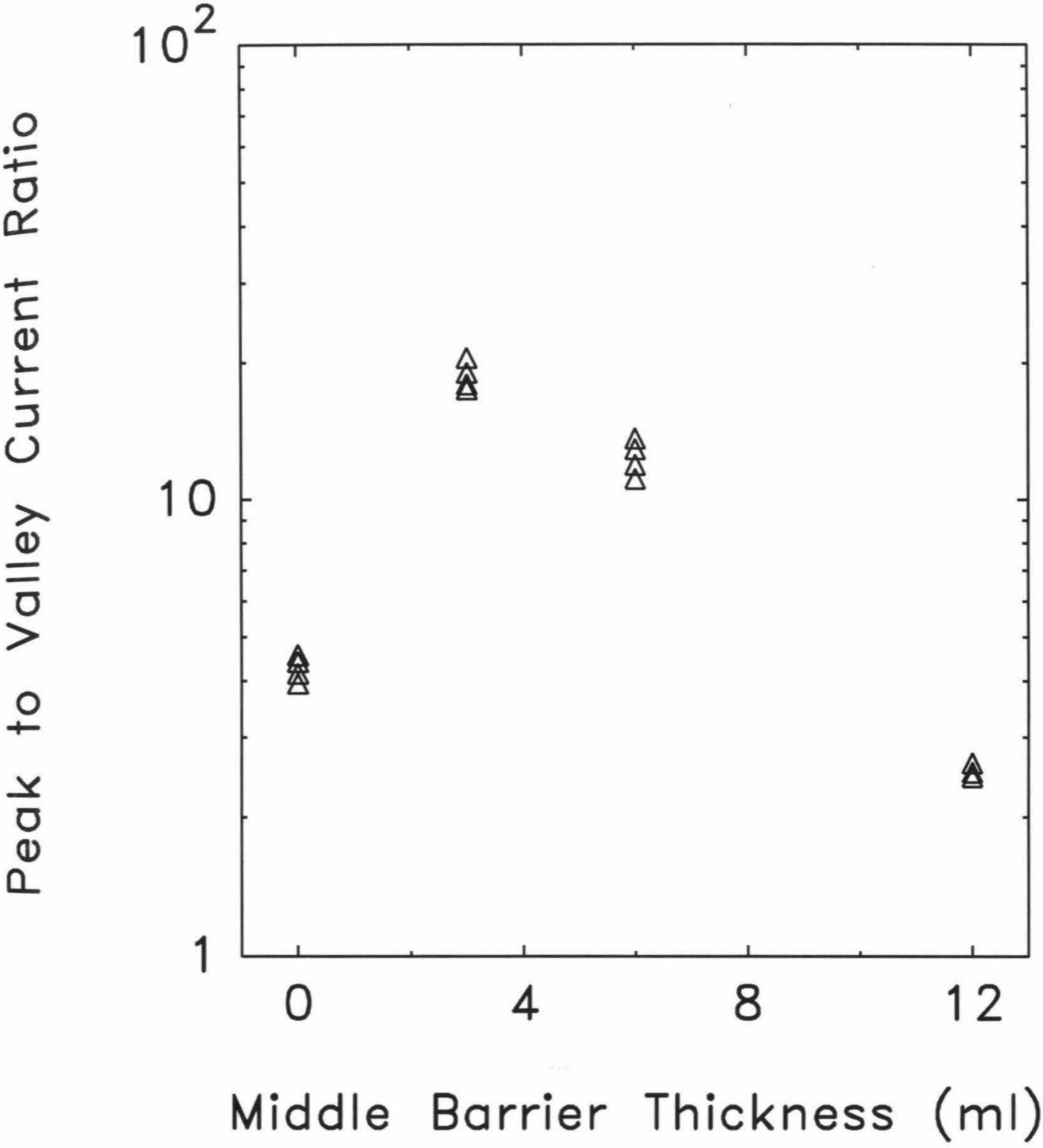

Figure 2.5: Measured peak-to-valley current ratios for the second resonance versus middle barrier thickness at 77 K. The plotted points show the range of device performance.

profile was computed by solving Poisson's equation across the device and requiring overall charge neutrality in the structure. Thomas-Fermi screening theory was used to relate the local carrier concentration to the conduction band edge position. We have not extended the calculation to cases in which the applied bias is large ($\geq$ 600 mV) because the assumptions made in computing the band profile become invalid: low charge densities in the well, low carrier temperatures, ect. The good agreement between the calculation, which assumes a coherent interaction between the wells, and the experimental data for thin middle barriers suggests that coherent processes play an important role in tunnel heterostructures.

The data in Fig. 2.6 show the effect of varying the central barrier width on the resonance positions. The difference between the voltages of the first peak for the double barrier structure and the sample with a 3-ML middle barrier can be understood by considering the wavefunctions of a particle in a box. Since the ground state wavefunction is peaked in the middle of the potential well, the introduction of a barrier in the center of the well significantly distorts the wavefunction raising the ground state energy. Doubling the central barrier's thickness to 6 ML had a minimal effect on the position of the first resonance indicating that the wavefunction still extends coherently across the middle barrier and both quantum wells. The data also show that the position of the second peak is insensitive to the thickness or even the presence of a middle barrier. This is as one would expect since the wavefunction of the first excited state of a particle in a box has a node where the central barrier is introduced and thus is not significantly perturbed. The effect of thin middle barriers on the measured resonance voltages is consistent with the quasi-bound states extending coherently across the central barrier.

In passing we report anomalously large PVR's for the heterostructure with a 3 ML central barrier (as high as 20.1:1 at 77 K as shown in Fig. 2.2(c)). It is

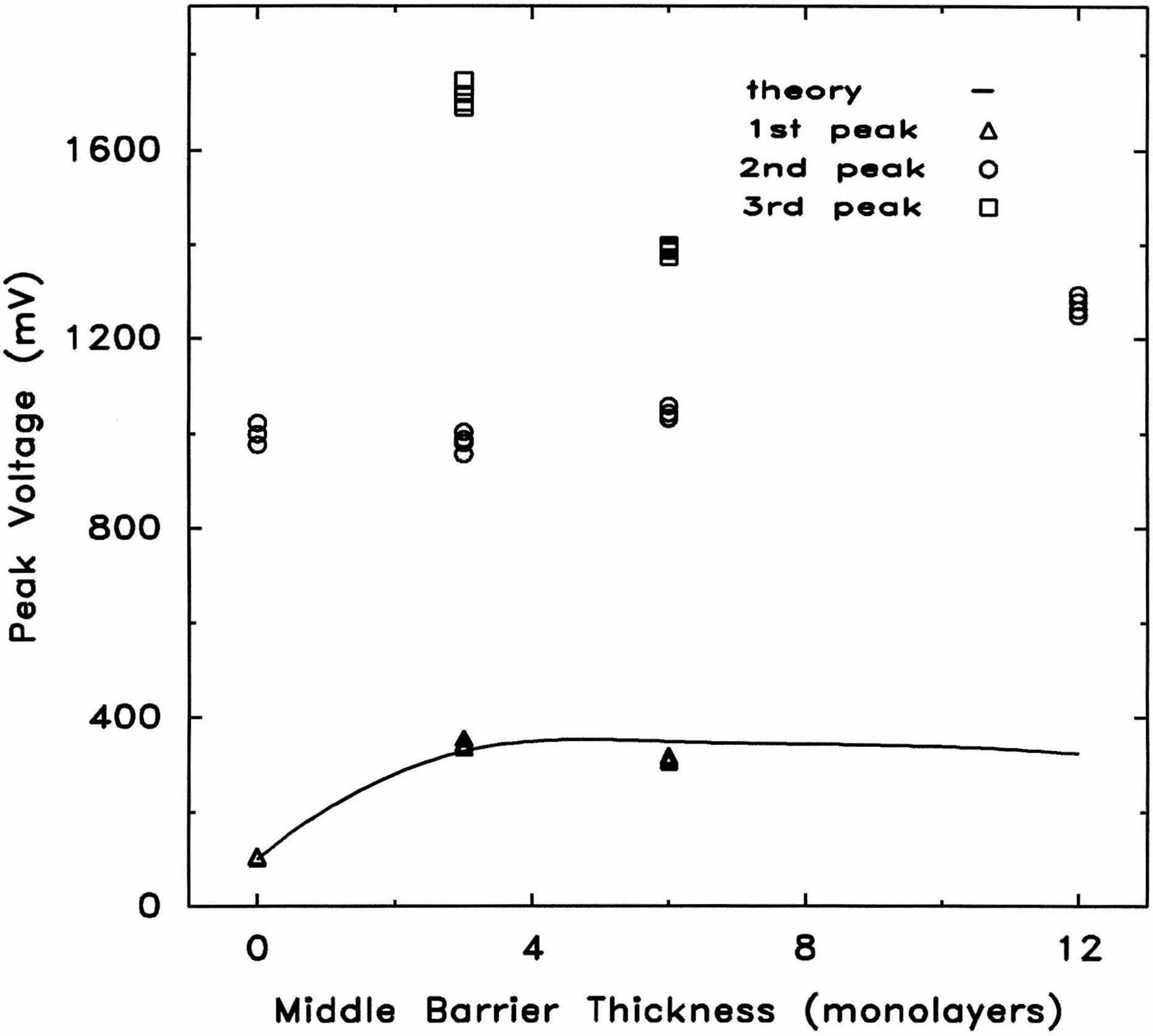

Figure 2.6: Positions of the current resonances versus middle barrier thickness at 77 K. The solid line is the result of a theoretical simulation. The plotted points show the range of measured values. The triangles, circles and squares correspond to the first, second and third peaks respectively.

possible that a more detailed study of this phenomenon could lead to a better understanding of nonresonant current transport mechanisms.

2.4.4 Conclusions

In summary we have grown a series of double quantum wells whose I-V curves show as many as three distinct NDR regions. These results are consistent with coherence between the electrons in the two quantum wells, since in the sequential model multiple NDR regions in a triple barrier structure are unlikely. The behavior of the peak current densities and PVR's as the thickness of the central barrier is increased provides further evidence that coherent tunneling plays a role in the observed NDR. The energies of the lowest resonances in the structures as a function of middle barrier width are in good agreement with values calculated using a coherent model of tunneling. The variation of the first and second current peaks is in qualitative agreement with a picture in which the eigenstates of the system extend coherently across thin middle barriers and both of the quantum wells. Finally, for thick middle barriers, the sequential picture of tunneling seems to be valid. For the sample with the thickest middle barrier, a single current resonance was observed. This single resonance was weaker than those in the other structures based on its peak current density and PVR.

2.5 The Role of the X-point in Tunneling

2.5.1 Introduction

The photoluminescence (PL) signal from a quantum well is proportional to $n \cdot p$, where n and p are the electron and hole concentrations in the well layer. If a nonequilibrium population of electrons and holes is placed in the well by a short optical pulse, then the PL signal will decay over time as the carriers leave the well. Measuring the decay of the quantum well's PL signal gives the tunneling time, if tunneling is the dominate escape mechanism. Because of the extremely short tunneling times present in RTD's, direct measurement of the PL decay is extremely difficult.

This section gives the results of measurements the intensity and energy of PL from a series of GaAs/AlAs double barriers with fixed barrier thickness and varying well widths. Studying the PL from such structures gives two kinds of information about the structures. The energy of the PL gives the confinement energy which can be compared to bandstructure calculations. The intensity of the PL at the bound state energy is related to the escape time for carriers in the quantum well. If the carrier escape rate is comparable to or shorter than the radiative recombination rate, then some of the carriers will be able to leave the well before they can recombine and give off PL. Because of this, all other things being equal, the PL signal from a structure with a short tunneling time will be less intense than from one with a long tunneling time.

Consider a double barrier device with a well width, L_w, and fixed outer barrier thickness. In a one-band effective mass approximation, the change in the PL energy will go as $1/L_w^2$, where L_w is the well width. However, the carrier escape rate should be a very weak function of L_w since the bound state lifetime, hence the tunneling time for our purposes, is not greatly effected until the quantum confinement energy becomes comparable to the barrier height. From this we would expect that the PL energy will be a strong function of L_w while the intensity should be rather insensitive to L_w. This is true as long as the confinement energy is not comparable to the barrier height. In certain situations, though, it is necessary to use a more detailed picture of the band structure of the device. In particular, examination of AlAs's band structure shows that the lowest conduction band minimum occurs at the edge of the Brillouin zone in the [100] direction. This place is called the X-point. By contrast, in GaAs the lowest conduction band minimum occurs at the center of the Brillouin zone, the Γ-point. The X-point of GaAs is at a higher energy than the X-point in AlAs. The opposite is true at the Γ-point. This means that at the Γ-point, AlAs is a barrier for GaAs electrons, while at the X-point, GaAs is a barrier for AlAs electrons. Fig. 2.7 shows both the Γ-point and X-point bandedge diagram for a double barrier structure. In appropriately grown AlAs/GaAs double barriers, it is possible for the GaAs Γ-point bound states to be close enough in energy to the AlAs X-point bound states for them to interact. The samples studied in this section were so grown.

2.5.2 Experiment

Continuous PL experiments performed on a set samples at 5 K. The PL peak positions were compared to a calculation of the devices' band structure. The calculation included the effect of the X-point states in the AlAs barriers. By comparing the PL peak positions to the theory and examining the peak PL intensity as a function of well width, the role of these X-point barrier states was investigated. The sample set consisted of double barrier heterostructures where the barrier thickness was fixed at 38 Å . Nine samples were grown with well widths varying between 26 and 58 Å . The double barriers were capped with 300 Åof GaAs, which is thin enough for optical energy to escape from the well, but thick enough to avoid quantum confinement in the cap layer.

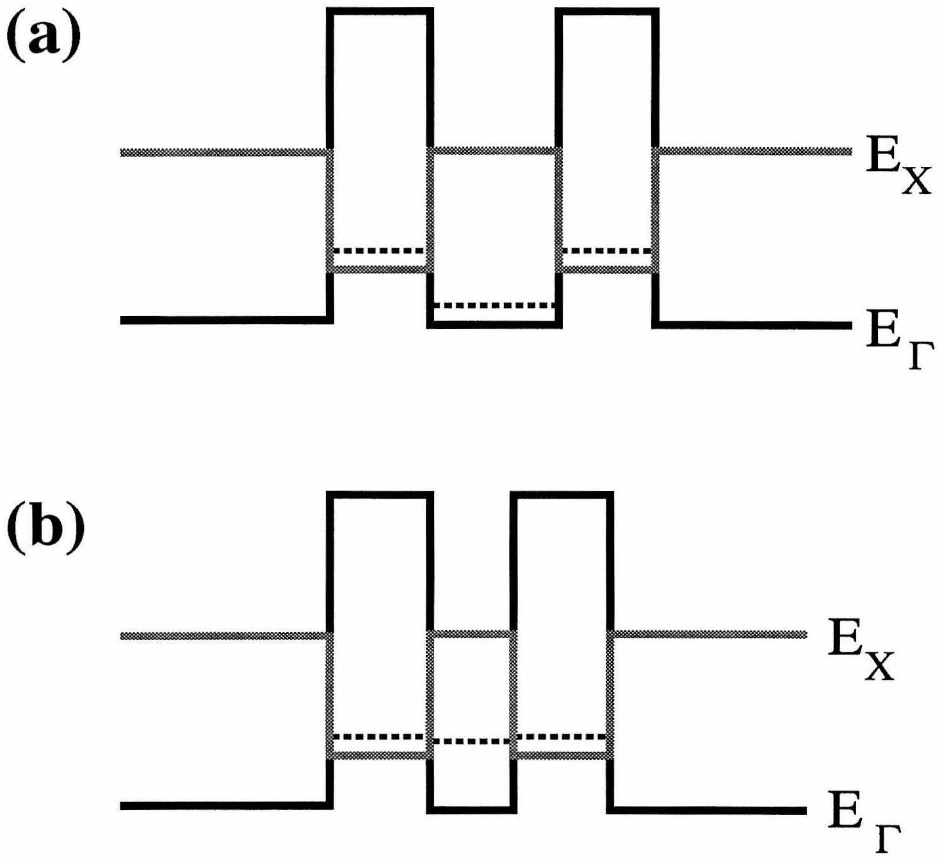

Figure 2.7: Conduction band edges at the X-point and Γ-point for a GaAs/AlAs double barrier. The position in energy of the lowest quasi-bound states are schematically shown with dashed lines. (a) Wide GaAs quantum well where the Γ-point state lies below the X-point state. (b) Narrow GaAs well where the Γ- and X-point states are at comparable energies.

2.5.3 Results

Fig. 2.8(a) shows the measured energies of the PL peaks. The appearance of a second peak in structures with $L_w < 14.7$ ML indicates that an additional bound electron or hole state is becoming important to the PL. Fig. 2.8(b) is a calculation of the energy of optical transistions between the ground state heavy-hole level and the lowest Γ-point state (Γhh_1), the lowest X-point state (X_1hh_1) and the first excited X-point state (X_2hh_1) which are labeled in the figure. Transitions from conduction-band states that are concentrated in the GaAs well are marked with an "$\times$" symbol, while those from states concentrated in the AlAs barrier are marked by the "+" symbol. Transitions from conduction-band states that have comparable probability densities in the well and barrier are marked by both symbols.

Comparing the experimental values to the calculation explains the origin of the PL peaks. For thick wells, the PL data is consistent with the calculated Γhh_1 transition. For wells with $L_w < 14.7$ ML, the high energy PL peak also corresponds to the Γhh_1 transition. The low energy PL peak for $L_w < 14.7$ ML is consistent with the calculated X_1hh_1 transition. This is the first observation of optical transitions that are indirect in both space and momentum. The presence of this second peak indicates that the Γ states in the GaAs well do indeed interact with the X-point states in the AlAs barrier. If so, then structures where the Γ- and X-point states overlap in energy are expected to have shorter carrier escape times since there is now an additional escape mechanism available.

The integrated intensities of the PL peaks are shown in Fig 2.9. For structures with well widths between 16 and 20.5 ML, the PL intensity is flat. This is consistent with the previous prediction of the quasi-bound well state lifetime based on a one band effective mass model. For $L_w < 16$ ML the PL drops sharply

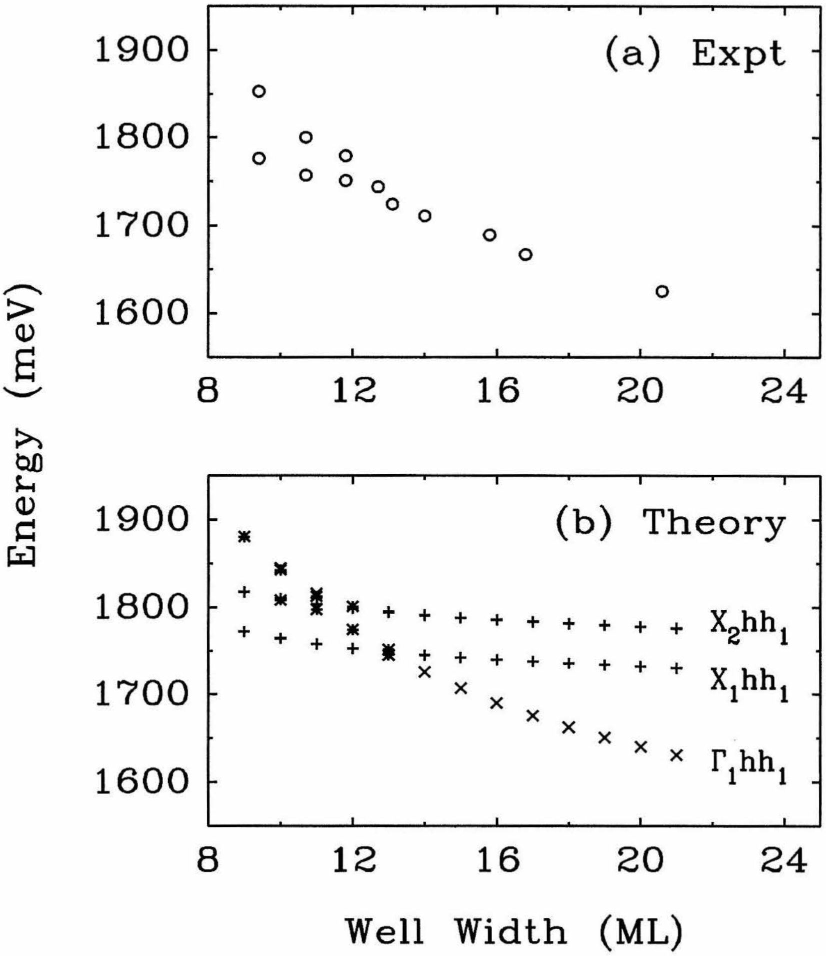

Figure 2.8: (a) Photoluminescence peaks at 5 K. The lower energy peaks observed for $L_w < 12$ monolayers are due to spatially indirect transitions between X-point electrons and Γ-point heavy-hole states. (b) Calculated energies of the lowest Γ-point state, Γ_1, and the two lowest X-point states, X_1 and X_2, to lowest heavy-hole (hh_1) transitions. Transistions involving electron states with significant probability density in the quantum well are shown by the "×" symbol. Transitions involving conduction-band states that are concentrated in the AlAs barriers are marked by "+."

as the well width decreases. The PL intensity begins to drop precisely where the data and calculation in Fig. 2.8 indicates the Γ- and X-point states begin to mix. The rate of decrease changes near $L_w = 12$ ML where PL from the X_1hh_1 transition is observed. These results strongly suggests that the decrease in PL intensity is caused by faster electron escape from the GaAs quantum well since the X-point states in the AlAs barrier are now available to them. In a sequential model of tunneling, the electrons would tunnel from the Γ-like bound state in the GaAs well into an X-like state in the AlAs barriers then out into the GaAs electrodes. In a coherent picture of tunneling, the eigenstates of the double barrier structure will consist of mixed Γ-X states with significant probability density in both the GaAs well and the AlAs barrier. This would lead to states which are wider in energy and hence have shorter lifetimes.

2.6 Summary

In summary we have conducted studies of tunneling in AlAs/GaAs heterostructures. Examination of the electrical characteristics of triple barrier devices with varying middle barrier thicknesses leads to the conclusion that the quasi–bound states in the system extend across both wells and the central barrier. Because of this, the electrons in the two wells maintain phase coherence. An optical study of AlAs/GaAs double barriers was also reported. The intensity and energy of photoluminescence from structures with fixed barrier thicknesses and varying well widths was studied. For narrow wells, a second photoluminescence peak was observed. Comparing this peak to a theoretical model which included X-point states in the barrier led to the conclusion that the second peak was due to recombination between X-point conduction band states in the AlAs barrier with valence-band states in the GaAs quantum well. The intensity of the photolumi-

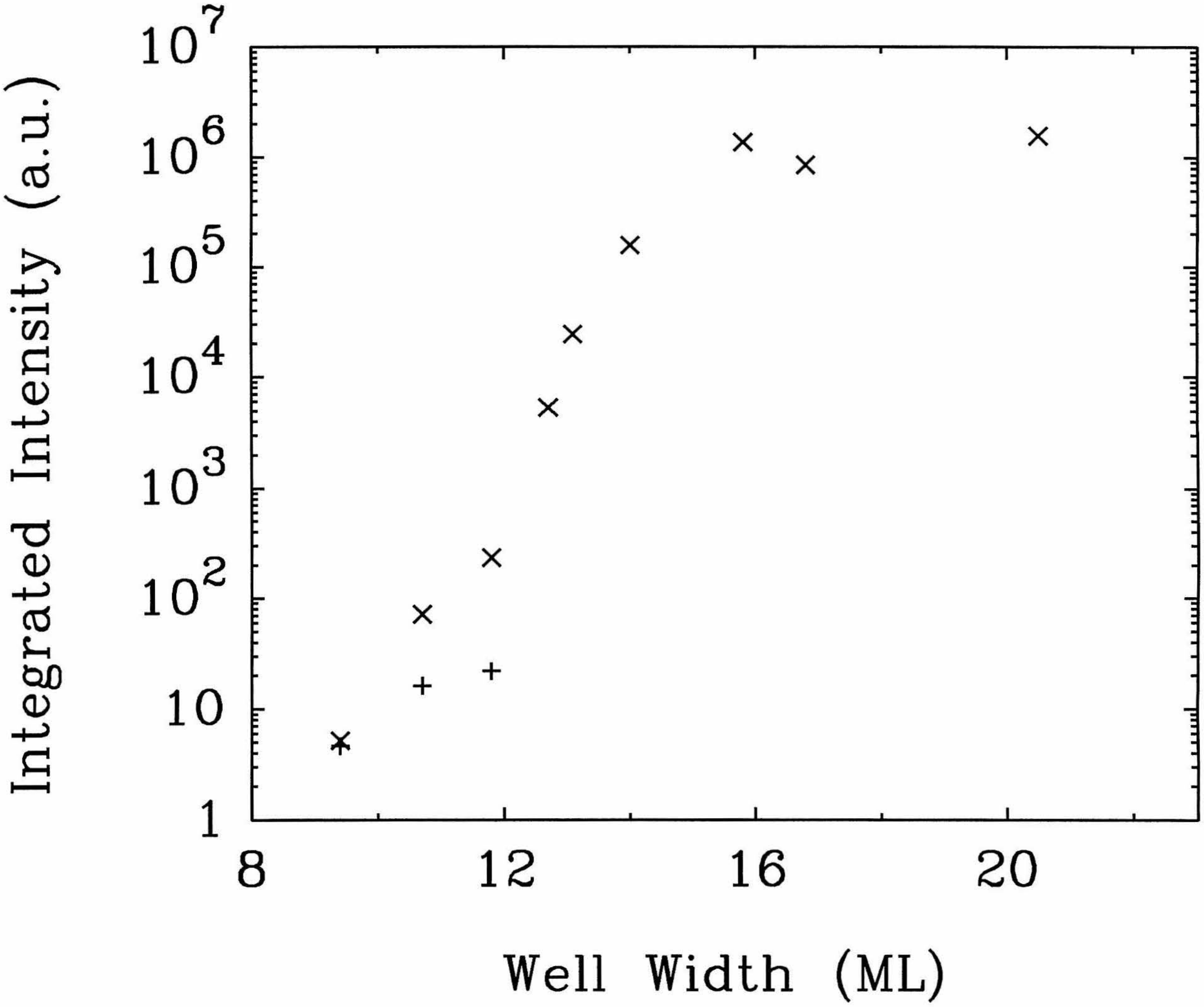

Figure 2.9: Integrated photoluminescence intensity under identical conditions, 5 K. The intensities of the Γ-point luminescence are marked with "×" and the X-point intensities are marked with "+" symbols. The drop in intensity with decreasing well width is attributed to escape of electrons from the GaAs quantum well via X-point states in the AlAs barriers.

nescence peaks was found to be a strong function of well width for sufficiently narrow wells. The intensity varied over five orders of magnitude between wells with 16 and wells with 9.5 monolayer GaAs quantum wells. This was attributed to faster carrier escape times in narrow quantum wells due to the availability of X-point states in the AlAs barriers.

References

[1] R. Tsu and L. Esaki, *Appl. Phys. Lett.*, **22**, 562 (1972).

[2] L.L. Chang, L. Esaki and R. Tsu, *Appl. Phys. Lett.*, **24**, 593 (1974).

[3] S. Luryi, *Appl. Phys. Lett.*, **47**, 490 (1985).

[4] S. Luryi, Tech. Dig. IEEE Int. Electron Devices Meeting, Dec. 2-4, Washington, DC , 66 (1985).

[5] C.I. Huang, M.J. Paulus, C.A. Bozada, S.C. Dudley, K.R. Evans, C.E. Stutz, R.L. Jones and M.E. Cheney, *Appl. Phys. Lett.*, **51**, 121 (1987).

[6] M.K. Jackson, M.B. Johnson, D.H. Chow, T.C. McGill and C.W. Nieh, *Appl. Phys. Lett.*, **54**, 6 (1989).

[7] D. Z.-Y. Ting and Y. C. Chang, Physical Review B, **36**, 4359 (1987).

[8] E.T. Yu, M.K. Jackson and T.C. McGill *Appl. Phys. Lett.*, **55**, 744 (1989).

Chapter 3

Interband Tunnel Structures

3.1 Introduction

3.1.1 Background

The nearly lattice-matched InAs/AlSb/GaSb material system is almost ideal for studying electron transport in semiconductor heterostructures, since Type I, Type II and broken-gap band alignments are obtainable. Fig. 3.1 shows the relative energies of the conduction and valence bandedges of InAs, GaSb and AlSb.[1, 2, 3] As shown in the Fig. 3.1, the band offset between GaSb and AlSb is Type I: the conduction and valence bandedges of GaSb lie within the band gap of AlSb. InAs and AlSb have a Type II alignment with the conduction band of InAs in the gap of AlSb and its valence band below that of AlSb. In this case AlSb is a large barrier for electrons in InAs and InAs is a small barrier for holes in AlSb. The final, and most interesting offset, is InAs/GaSb which has a broken gap alignment since the band gaps of the two materials do not overlap. Using AlSb and GaSb one can mimic almost any tunnel structure grown in GaAs/AlGaAs, the most intensely studied of all semiconductor heterostructure

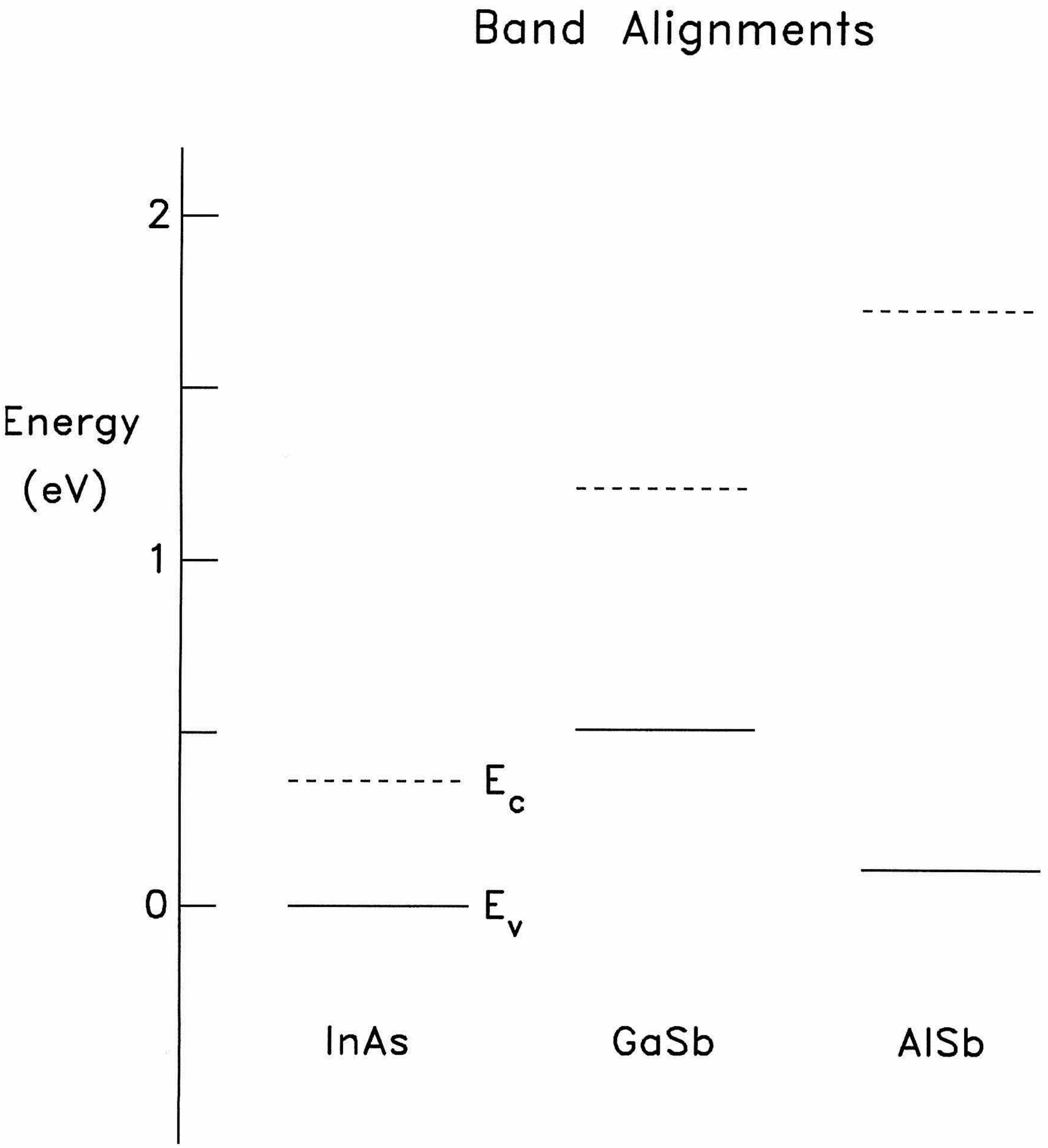

Figure 3.1: Conduction (dashed) and valence (solid) bandedges for the InAs/GaSb/AlSb material system. The energy gaps and band offsets allow the possibility of Type I, Type II, and Type II broken–gap band alignments. The indirect conduction band minimum is shown for AlSb.

systems. In addition, InAs/GaSb allows the study of transport and coupling between electron and hole states. These states can be either continuum or quasi-bound depending on the structure grown. The 'Interband Tunnel Structures' (ITS) of the title of this chapter are devices which involve transport between InAs conduction band states and GaSb valence band states.

Fig. 3.2 shows energy bandedge diagrams of some of the tunnel structures which were grown, processed and characterized for this work. Each of the panels is a sketch of band energy vs. position along the growth axis for several, multi-layered structures. The shaded regions represent the bandgap of the individual layers. The top and bottom of the shaded regions denote the conduction band minimum and valence band maximum respectively. A great many more devices are possible by adding more layers to the active region of the structure. However, all of the basic physics of interband tunneling is demonstrated by the structures in Fig. 3.2 with other devices being minor variations of these. Table 3.1 gives a summary of some of the devices' electrical properties. Most of the structures in Fig. 3.2 will be dealt with in detail later in the chapter so the reader need not panic at the number of devices shown. The purpose of Fig. 3.2 and Table 3.1 is to show the tremendous variety of structures and device characteristics that can be realized in this single material system.

3.1.2 Outline of Chapter

Section 3.2 sketches out the growth and processing of InAs/GaSb/AlSb tunnel devices. (A more complete treatment is contained in appendix ARG.) In sections 3.3 through 3.8 we present (in rough chronological order) the results of experimental and theoretical studies of the structures shown in Fig. 3.2. The experimental results in sections 3.3 through 3.8 are summarized in Table 3.1. Sec-

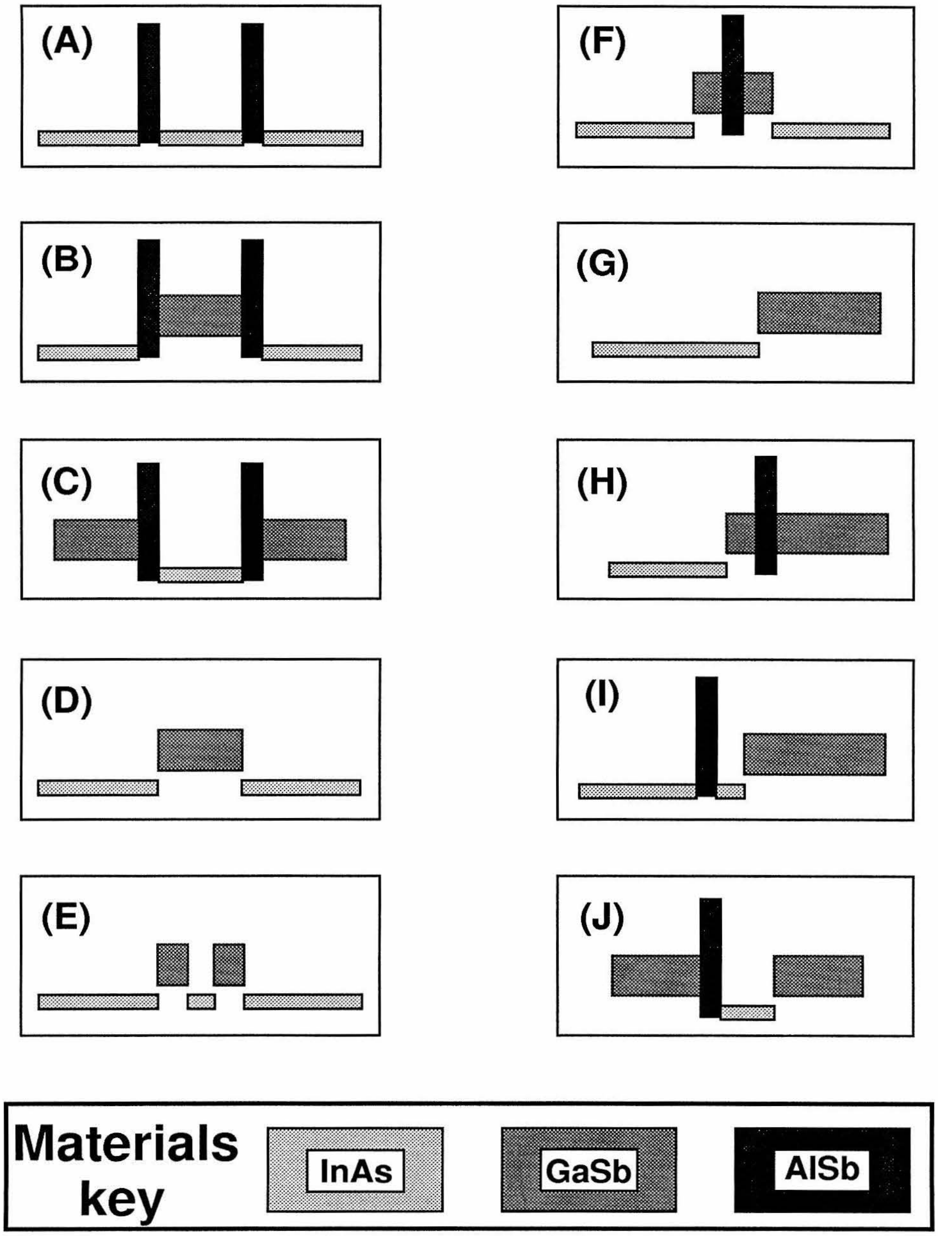

Figure 3.2: Schematic energy band diagrams (energy vs. position) for ten different tunnel structures realized in the InAs/GaSb/AlSb material system. Energy gaps for each material are shaded, so that the top (bottom) of each shaded region represents the conduction (valence) bandedge in the heterostructure.

Material Sequence	Temp. (K)	Peak-to-Valley Current Ratio	Peak Current Density (A/cm^2)
InAs(n)/AlSb/InAs/AlSb/InAs(n)	300	4.0	3.7×10^5
	300	13.0	4.0×10^3
InAs(n)/AlSb/GaSb/AlSb/InAs(n)	300	12.0	950
	300	21.0	50
	77	60.0	1.7×10^3
	77	88.0	90
GaSb(p)/AlSb/InAs/AlSb/GaSb(p)	300	8.0 – 10.0	450 – 500
	77	16.0	450 – 500
InAs(n)/GaSb/InAs(n)	300	2.2	5.1×10^3
	300	1.2	1.2×10^5
InAs(n)/GaSb/InAs/GaSb/InAs(n)	300	2.2	1.2×10^4
InAs(n)/GaSb/AlSb/GaSb/InAs(n)	300	3.5	1.4×10^4
InAs(n)/GaSb(p)	300	1.7	4.2×10^4
	300	1.2	8.4×10^4
InAs(n)/GaSb/AlSb/GaSb(p)	300	1.5 – 1.8	1.6×10^5
	300	1.5 – 1.8	3.5×10^4
InAs(n)/AlSb/InAs/GaSb(p)	300	1.5 – 1.7	3.1×10^3
InAs(n)/AlSb/GaSb/InAs(n)	300	$15.0 - 18.0^{(R)}$	$2.7 \times 10^{3\,(R)}$
		$1.6 - 2.2^{(F)}$	$1.52 \times 10^{4\,(F)}$

Table 3.1: Summary of two-terminal device performance. When more than one set of electrical characteristics are given, the different sets correspond to different device layer thicknesses. The superscripts ‘R’ and ‘F’ refer to reverse and forward bias respectively.

tion 3.9 gives some rules-of-thumb which are helpful in understanding interband devices, and the chapter is summarized in section 3.10.

3.2 Growth and Device Processing

All of the samples reported on in this chapter were grown on [100] GaAs substrates in a Perkin-Elmer 430 molecular beam epitaxy system using cracked arsenic and antimony. The lattice constant of GaAs is about 7.0% smaller than that of the InAs/GaSb/AlSb material system. As a result, a buffer layer at least 1μm thick of either InAs or GaSb was deposited before the active region of the tunnel structure. This relaxed buffer layer had $\sim 10^7$ dislocations per cm^2 as estimated from transmission electron microscope images. Devices grown on lattice matched substrates showed no substantial improvement in either peak-to-valley current ratios (PVR) or peak current densities (J_p) over devices grown on relaxed buffer layers deposited on GaAs substrates. Because of this, GaAs substrates were used for subsequent studies due to their cheaper cost. The details of growing high quality InAs, GaSb and AlSb layers on GaAs are given in appendix *ARG.* Unless otherwise stated, the films were deposited at a substrate temperature of 480 °C for InAs, 500 °C for GaSb and 520 °C for AlSb at a rate of 1.0, 0.5 and 0.25 μm/hr respectively. When forming an InAs/$\mathrm{Al}_x\mathrm{Ga}_{1-x}\mathrm{Sb}$ (for all values of x) interface, the InAs growth rate was lowered to 0.5 μm/hr. The lower deposition rate helps to smooth the growth front and requires a smaller arsenic flux, leading to less arsenic incorporation in the antimonide layer.[4] At the heterointerfaces the growth was usually interrupted for 5 seconds, and the growth front was soaked in an antimony flux to achieve a smoother interface. If a doped layer was desired, codeposition of Si resulted in p-type GaSb (up to p $\sim 4\mathrm{x}10^{18} cm^{-3}$[5]) and n-type InAs (up to n $\sim 8\mathrm{x}10^{18} cm^{-3}$.)

During growth, the crystal's surface was monitored using reflection high energy electron diffraction (RHEED). The InAs ($Al_xGa_{1-x}Sb$) surfaces showed a 2×4 (1×3) RHEED pattern indicating an anion rich surface reconstruction. However, during growth interrupts when the InAs surface sat in an Sb flux the RHEED pattern changed to a 1×3 reconstruction similar to that of InSb indicating As and Sb were exchanging on the surface. The results of subsequent studies of this and similar phenomenon are presented in Chapters 5 and 6.

After growth, circular device mesas, ranging from 6 to 120 μm in diameter, were formed using conventional photolithography and wet etches. A solution of H_2SO_4:H_2O_2:H_2O = 1:8:80 was used to etch the InAs layers and Br:HBr:methanol = 1:100:100 to etch the $Al_xGa_{1-x}Sb$ layers. Ohmic contacts to the devices were formed using thin Au/Ge layers. Current-voltage (I-V) curves were typically measured at both room temperature and 77 K by probing the mesas with a thin gold wire.

3.3 Resonant Interband Tunneling (RIT) Structures

3.3.1 Introduction

The first type of ITS that was experimentally studied was the resonant interband tunneling (RIT) device. RIT's come in two flavors which correspond to the devices in Fig. 3.2 (b) and 3.2 (c). Fig. 3.3 gives a more detailed description of their band energy diagrams. Even though band bending is ignored in Fig. 3.3, following the Fermi level across the device gives a basic understanding of the current conduction path. For the upper, or p-well RIT, charge carriers tunnel across an AlSb barrier from continuum, conduction band states in the InAs electrode layer into the GaSb valence band well. Once the charge carriers are in the valence-band well, they then tunnel through the second AlSb barrier into the conduction-band of the second InAs electrode. Of course the preceding is not intended to suggest that the tunneling process is sequential, but merely to trace out the current path. Depending on the thickness of the well, the valence band states can be either continuum or confined by the AlSb barriers. In our studies we restricted ourselves to well layers which gave rise to confined states. For n-well RIT's sketched in the lower portion of Fig. 3.3 the conduction path is similar. Charge tunnels from continuum valence band states into confined or continuum conduction band states in the InAs well and back into the valence band of the second GaSb electrode.

Because of the quasi–bound state (QBS) in the well layer, there is a sharp peak in the I-V curves of these devices. Off resonance, the bandgap of the well layer combines with the AlSb barriers to suppress current conduction. This thick barrier leads to RIT valley currents which are much smaller than in the conventional intraband devices discussed in Chapter 2. A more detailed discussion of RIT's is given in section 3.3.3 following an examination of some experimental I-V curves.

3.3.2 Experimental I-V Curves

Fig. 3.4 shows representative RIT I-V curves taken at room temperature. The upper (lower) I-V curve in Fig. 3.4 corresponds to the upper (lower) band energy diagram in Fig. 3.3. When comparing these I-V curves to those of AlAs/GaAs RTD's shown in Fig. 2.2, one thing is readily apparent: the PVR's of RIT's are much larger than those of intraband RTD's. The comparison is especially striking since the RIT I-V's were taken at room temperature. Typical RIT PVR's are

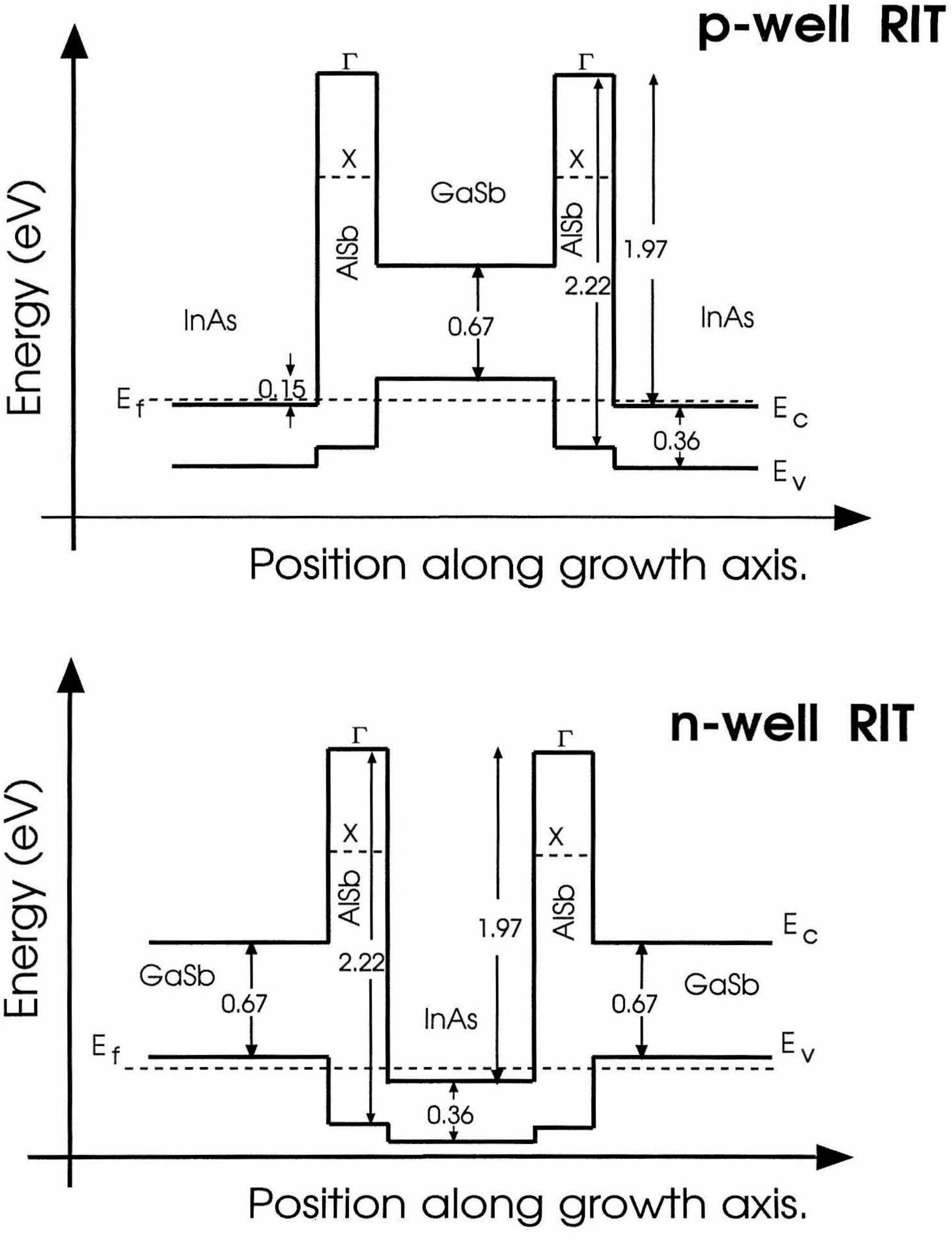

Figure 3.3: Band energy diagrams of the two types of RIT's. In the upper device, electrons move from the conduction-band of the InAs electrode into a bound state in the GaSb valence-band and back into the InAs conduction-band. For the device shown in the lower diagram, a complimentary current path is taken.

better than 20:1 at room temperature and 100:1 at 77 K. AlAs/GaAs RTD's have PVR's which are typically 3:1 at 300 K and 10:1 at 77 K. The reason for the vast improvement in PVR is discussed in detail in Section 3.3.3.

Besides the dramatic difference in PVR, there are other differences between RIT and intraband I-V curves as a direct result of their different current conduction paths. Among then are:

1. Intraband devices (Fig. 2.2) have an exponential current onset and the current drops sharply at the onset of NDR. RIT's by contrast (Fig. 3.4) are ohmic at small applied biases and the current saturates just before the NDR region.

2. The temperature dependence of interband and intraband I-V characteristics are very different. Fig. 3.5 shows I-V curves of the same RIT device taken at 300 K, 77 K and 4.2 K. The data is not a strong a function of temperature. However, as discussed in section 2.3, temperature has a dramatic effect on intraband devices (see Fig. 2.4.2).

3. The current valley is much broader in RIT's than in conventional RTD's.

These differences are a direct result of the fact that both valence and conduction band states are involved in resonant conduction in RIT's. This is discussed in sections 3.3.3 and 3.4. Finally the large PVR's, temperature insensitivity and wide current valleys make RIT's especially suited for use in logic applications. While the foregoing is incomplete, hopefully it has suggested that interband tunnel devices are a new class of structures, distinct from conventional AlGaAs/GaAs RTD's.

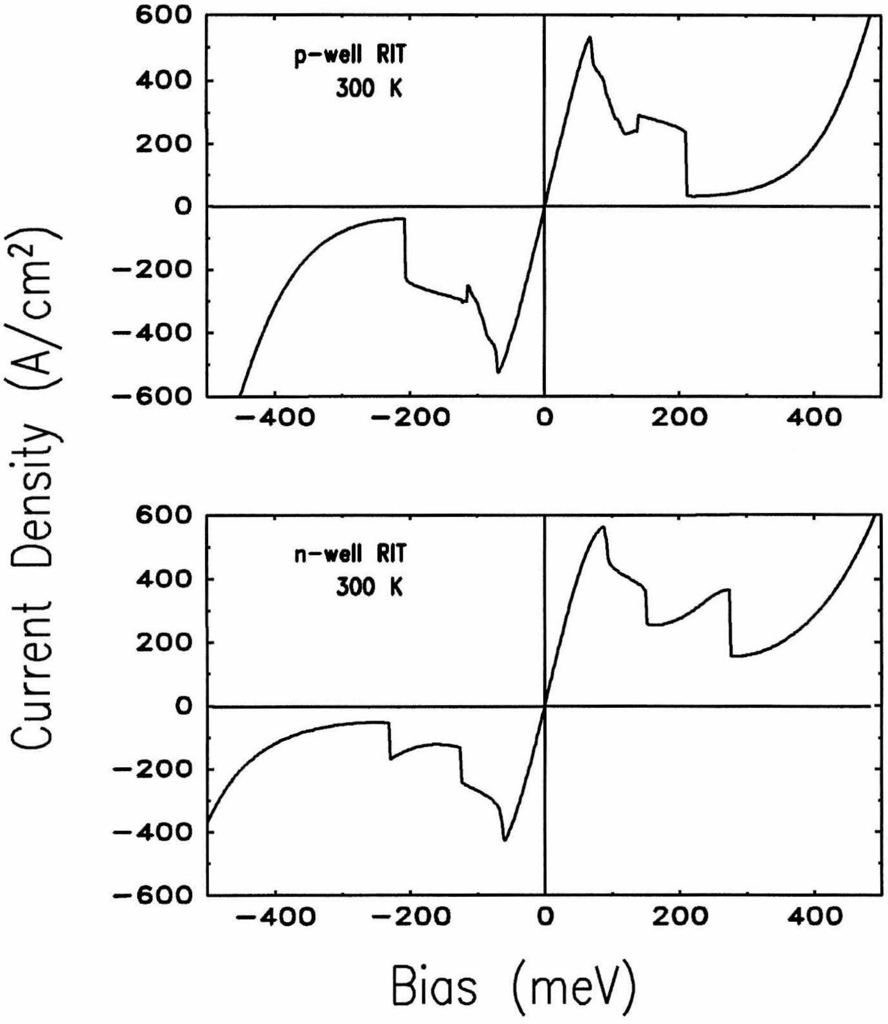

Figure 3.4: Current-voltage characteristics of both types of RIT structures at room temperature.

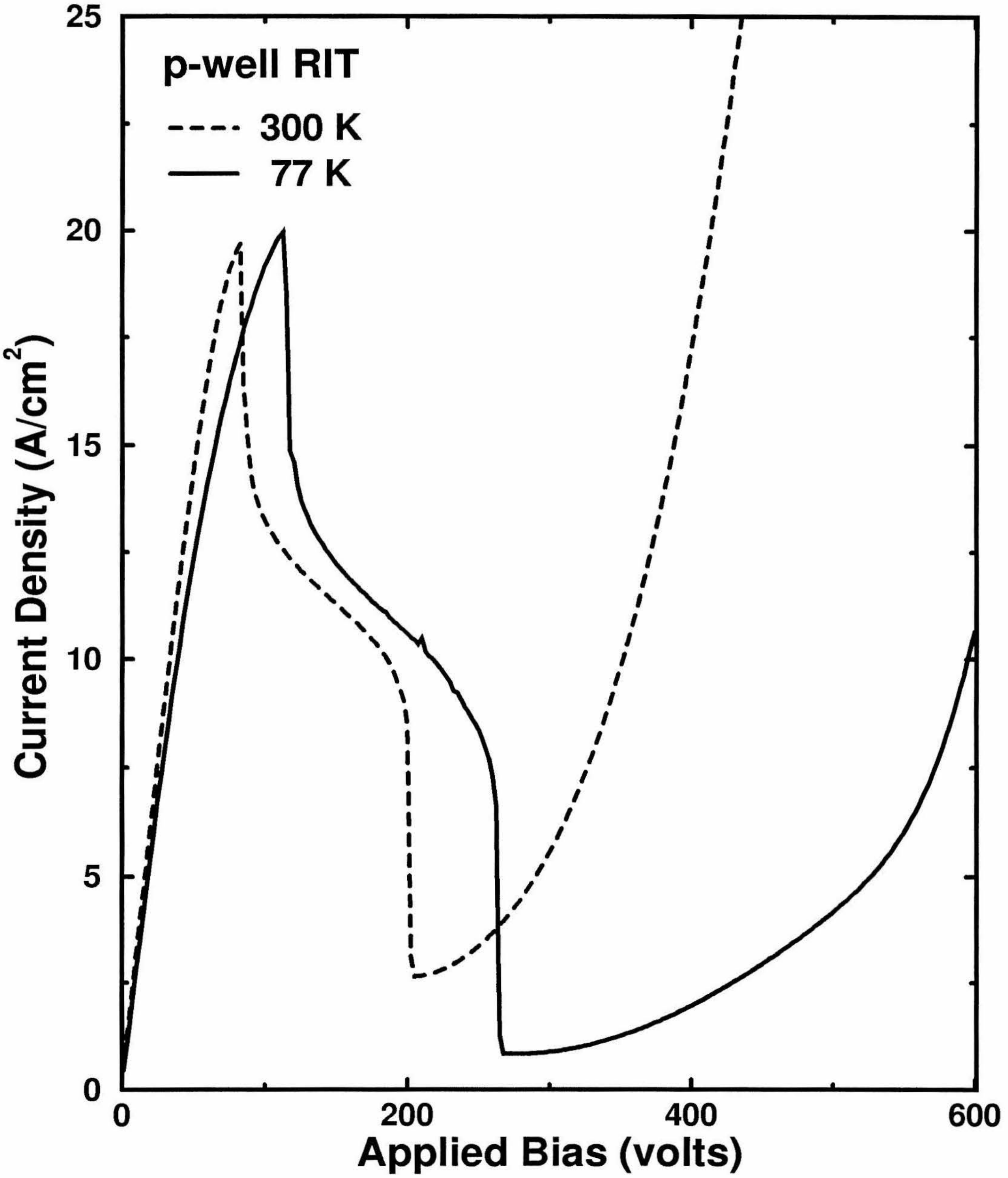

Figure 3.5: A series of experimental I-V curves taken from RIT's at various temperatures. The data show that the peak-to-valley ratios and peak current densities of RIT's are much less sensitive to temperature than intraband RTD's (see Fig. 2.2).

3.3.3 Origin of NDR in the RIT Structure

Before examining the operation of these devices, two points need to be covered: the nature of the mobile charge in these devices and an intuitive picture of transport between conduction and valence bands. When considering ITS it is helpful to think of only one type of charge carrier. Attempting to track both holes and electrons leads to an unnecessarily confusing picture of these structures. For the purposes of this thesis, we will view these devices in terms of electron conduction only, meaning that the valence-bands will be thought of as electron states that are almost full. Of course, the structures could be analyzed just as well by considering only holes.

Developing an intuitive picture of transport between conduction and valence band states can be awkward, though less so if only one type of charge carrier is considered. One way to view current flow in a semiconductor crystal is in the tight-binding (TB) formalism. In the limit of widely separated atoms, TB treats conduction as hopping between atomic states on adjacent atoms. The probability for an electron to jump from one atom to a neighbor is proportional to the integral of the wavefunction overlap between the initial and final states. This matrix element is inversely proportional to the effective mass of the charge carrier: large wavefunction overlaps give rise to small effective masses. In the TB picture, the conduction-band is due to the interaction of s-type atomic states and both the light-hole and heavy-hole valence-bands come from p-type atomic levels. Suppose the coordinate system in the crystal is chosen so that current is flowing in the $\hat{z}$ direction. In the limit of widely separated atoms, the light-hole band corresponds to electrons hopping between P_z orbitals on adjacent atoms. Hopping among the P_x and P_y atomic orbitals give rise to the heavy hole band. Since the effective mass of a band is inversely proportional to the overlap integral between atomic states, the light-hole mass will be much smaller than the heavy-hole mass. Now consider coupling between bands. In the limit we are considering, the coupling between electrons and heavy-holes will be exactly zero due to the relative symmetry of the S, P_x and P_y atomic orbitals. Similarly, light and heavy holes will not couple. However, there are no symmetry restrictions on coupling between electrons and light-holes. If the S and P_z atomic orbitals do have a spatial overlap, electrons can move between them.

Now consider the case where the atoms are brought close together as in a semiconductor crystal. It is no longer valid to think of the carriers in the crystal as being localized in atomic orbitals. The electron eigenstates are now delocalized plane waves. The S orbitals interact to form the conduction band, the P_z atomic orbitals give rise to the light-hole band and the P_x and P_y atomic orbitals form the heavy-hole band. Eventhough the underlying atomic orbitals are no longer eigenstates of the system, their symmetry does effect the bands they give rise to. From our consideration of the case of widely separated atoms, we would expect that the conduction and light-hole bands will couple but that neither will interact with the heavy-hole band. In addition, the electron and light-hole mass will be comparable while the heavy-hole mass is much larger. This picture is valid for a bulk material.

The above picture is inadequate for heterostructures. Once the crystal's spatial symmetry has been broken, it is possible that the conduction and valence-bands of adjacent layers will overlap in energy. If this happens, as it does for InAs and GaSb, than electrons can move between the conduction and valence-bands of the different materials. In addition, the breaking of the crystal's symmetry leads to mixing of the various bands at an interface. Because of this, the individual bands in the crystal lose their exclusive S or P_j nature, and the coupling between the conduction and both valence-bands increases. Finally, for electrons with crystal momentum parallel to a heterostructure, the distinction between light-hole and heavy-hole bands is blurred. This also increases the coupling between the valence and conduction bands of adjacent layers.

For our purposes, we will only consider the coupling between the conduction and light-hole bands of adjacent layers. From the symmetry of the underlying atomic wavefunctions, this should be much stronger than electron/heavy-hole coupling. A theoretical treatment confirms that the majority of current conduction is due to electron/light-hole coupling[8]. The major effect of the heavy hole states is to modify the energy and dispersion of the light hole bands. In order to see directly the effect of heavy holes, it is necessary to study these devices in the presence of a magnetic field.

Once these devices are viewed only in terms of electron conduction and the nature of the electron/light-hole coupling has been demystified, understanding how RIT's work is rather straightforward. Panel (a) Fig. 3.6 shows a typical RIT I-V curve. Three regions of the curve are marked and correspond to Figs. 3.6 (b), 3.6 (c) and 3.6 (d). At low bias, in the ohmic onset region of the I-V curve, electrons resonantly tunnel between the InAs electrodes via the QBS in the GaSb valence-band as indicated in Fig. 3.6 (b). Fig. 3.6 (c) sketches the RIT's band structure near the current peak. Here, the number of available states in the GaSb well decreases, hence the current saturates. Finally, when enough bias has been applied to move the quasi–bound well state past the Fermi level of the electrode, current is blocked by the bandgap of the well as shown in Fig. 3.6 (d). Since an actual bandgap is blocking conduction, the inelastic and thermionic processes which give rise to valley currents are strongly inhibited. This explains the extremely large PVR's and broad current valleys observed in RIT's.

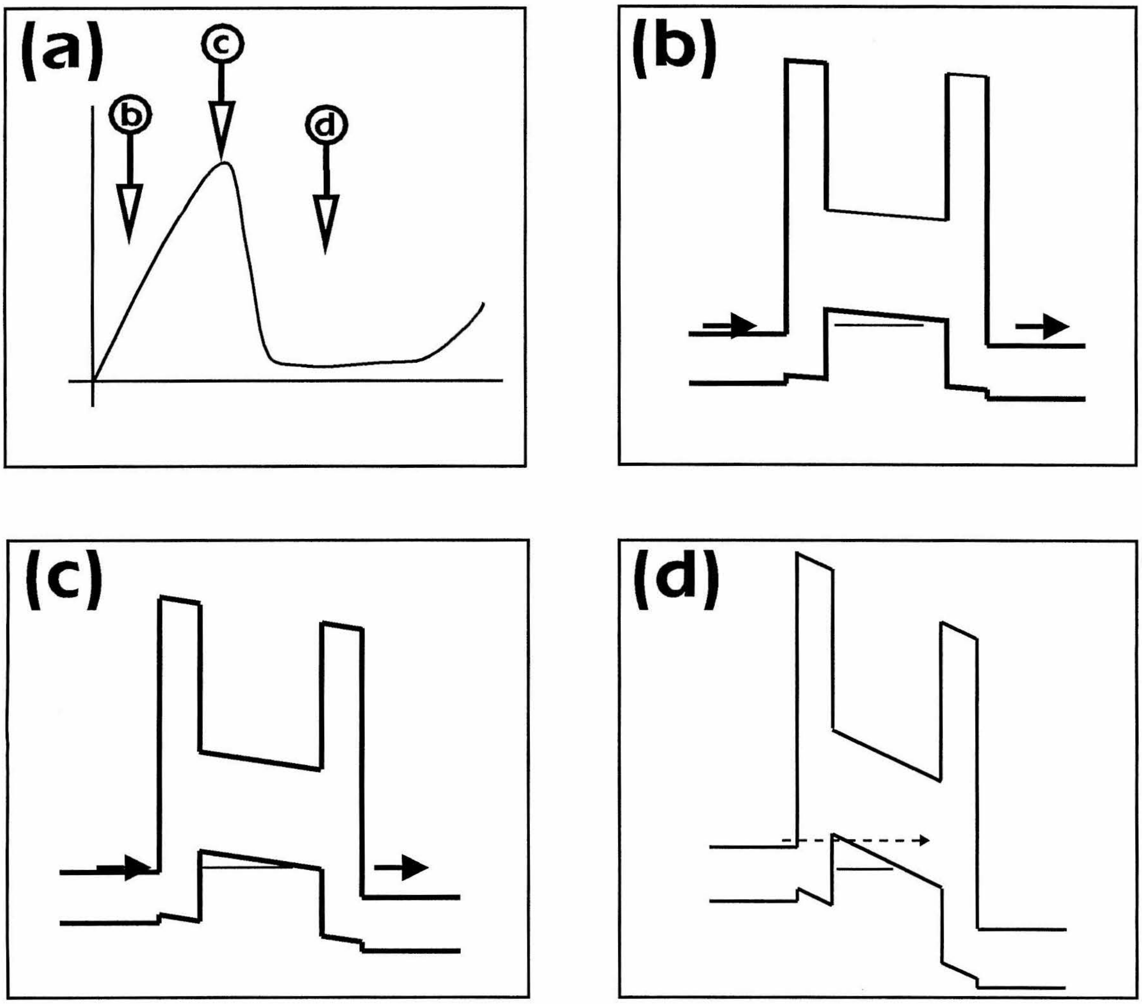

Figure 3.6: A sketch of the NDR mechanism of RIT's. Panel (a) shows a typical I-V curve. Panels (b), (c) and (d) show the device's band structure under three different applied biases. The markers on the I-V curve correspond to the three band-bending profiles.

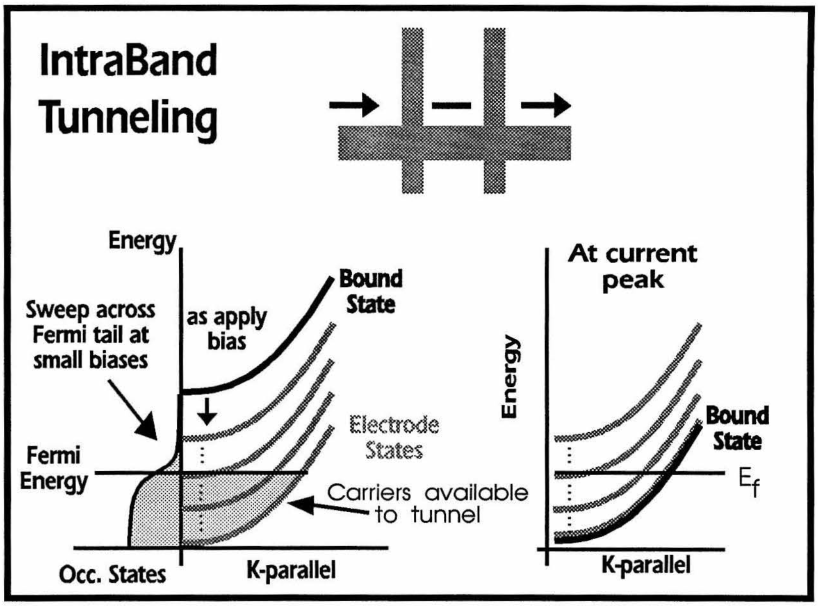

Figure 3.7: Sketch of the band structure for an intraband tunnel device.

3.4 Differences Between Interband and Intraband Tunneling

To understand the different shapes of AlAs/GaAs RTD's and RIT's, it is necessary to consider the details of their respective band structures. First consider the intraband case sketched in Fig. 3.7 and representing the I-V curves shown in Fig. 2.2. In the upper portion of the figure is a sketch of a typical, intraband device bandedge diagram. The shaded regions signify the bandgaps of the materials and the central, solid line represents a QBS. The arrows are intended to suggest the current path in the structure. Below the band diagram are two drawings of the dispersions in the well and source electrode layers. The leftmost drawing is for small applied biases, and the rightmost drawing is for voltages just past the current peak. The solid dispersions represent a quasi–bound well state while the gray curves signify the continuum of electrode states.

Since both the cladding layer and well states are in the conduction band, the sign of their curvature will be the same. If the well and electrode have the same material composition, then to first order their dispersions will be identical except for an energy offset due to quantum confinement. The band structure of the device will consist of a continuum of parabolas in the electrode and a single parabola in the quantum well. The continuum parabolas will be populated according to the Fermi distribution. At small biases the source electrons that have access to the quasi–bound well state are those in the high energy tail of the Fermi distribution. As the applied bias is increased, a series of electrode parabolas are swept in and out of resonance with the quasi–bound well state. A 'single' state in the electrode continuum resonates with the well. The population of the resonant electrode state is given by the Fermi function. Therefore, as the applied bias is increased, the Fermi tail of the source electrode is swept across the bound state, causing the exponential current onset shown in Fig. 2.2. Once the QBS in the well dips below the Fermi level, the number of source electrons available to tunnel will depend on how far below the Fermi level the resonanting electrode state is. However, typically the Fermi level is very near the conduction-band edge, hence this is a small effect. At the current peak, the most populated electrode state resonates with the well state and a large resonant current is carried though the structure. For biases slightly past resonance, the current drops sharply since there are no longer any elastically accessible well states. The voltage needed to shift the device from resonant to nonresonant conduction is on the order of the energy width of the well state: a few meV's. Past resonance, the current conduction will be the sum of any thermionic currents, electrode electrons that are scattered into the well state, and carriers in the Fermi tail that overlap any higher lying QBS. This sudden change in the number of accessible well states is

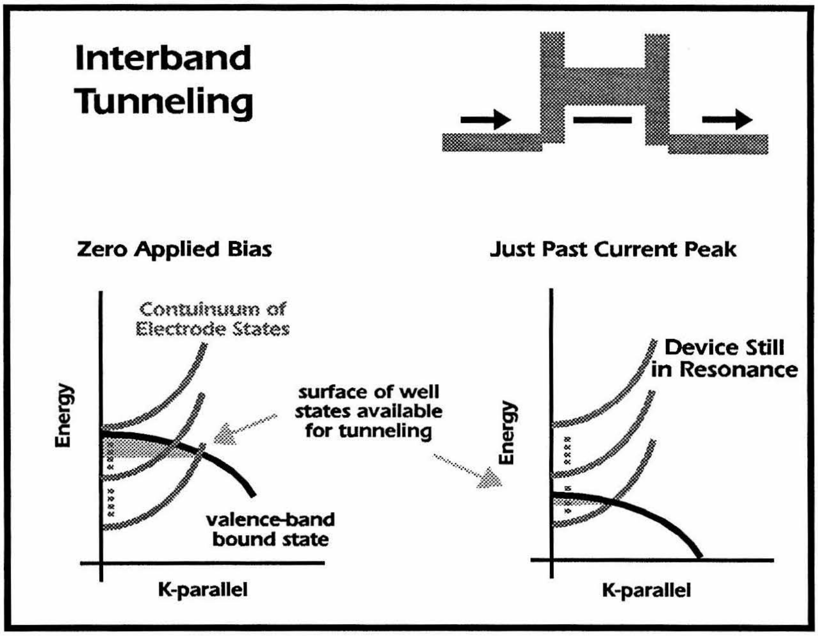

Figure 3.8: Sketch of the band structure for an interband tunnel device.

what causes the sharp onset of NDR in intraband devices. This also explains the strong temperature dependence of intraband devices. At high temperatures, the populations of the electrode states are smeared out. This has the effect of broadening the measured current resonance. Lowering the temperature reduces this Fermi smearing, increasing the peak current and reducing the magnitude of the onset current. Past resonance, the thermionic valley currents and inelastic currents due to phonon scattering are suppressed at low temperature. In intraband devices, lowering the temperature sharpens the measured current resonance and reduces the valley currents.

RIT's (and interband devices in general) work substantially differently. Fig. 3.8 is a sketch of the dispersion curves of the well and electrode states that contribute to the resonant tunneling. The diagram on the left represents the case of a small applied bias while that on the right is for a voltage just past the device's current peak. There are a continuum of parabolic electrode states and a single well state. Here the analysis departs from the intraband case. Since the masses of electrons and holes have different signs, the curvature of the allowed states will change sign when moving across the AlSb barriers. Because of this, an entire range of electrode states will simultaneously resonate with the well state. As the applied bias is increased, the overlap between the well state and the continuum of electrode states decreases. As a result the portion of the well state that is available for resonant conduction monotonically decreases as the applied voltage is increased.

By examining the energy and momentum overlap between the well and electrodes states, the number of well states that are available for conduction goes as $(K - V_{app})^{3/2}$. Here K is a constant related to the geometry of the conduction and valence-band parabolas and V_{app} is the applied bias. Now, as the bias is increased the electric fields in the cladding layers build up which increases the electron velocity. If we assume that the lifetime of the QBS is small compared to the transit times in the cladding layers, then the electron velocity $\propto V_{app}$ given that the electron velocity has not saturated. To first order the current will be proportional to the product of the number of well states contributing and the electron velocity: $I \propto (K - V_{app})^{3/2} \cdot V_{app}$. Fig. 3.9 shows a fit of this equation to an experimentally measured I-V curve. The curves match very closely up to the NDR region. When the device's differential resistance goes to zero, the parasitic inductances and capacitances in the circuit used to measure the I-V curve have a dramatic effect on the measured data. This continues throughout the NDR region. In addition, at the current peak, the current is observed to oscillate wildly at very high frequency. Because of this the simple equation described above is not expected to match the data after the onset of NDR. However, the equation derived does match the data very well before the NDR region. In fact, this simple equation describes the pre-NDR I-V curves of all the devices listed in Fig. 3.1. Examining the equation in the NDR region leads to the conclusion that interband devices are still resonanting in the NDR region. The current peak occurs at a bias where the overlap between well and electrode states begins to decrease faster than the electron velocity is increasing. The voltage at which NDR occurs is directly related to the shape of the well and electrode dispersions, not just the confinement energy of the well state as in intraband tunneling.

From the preceding discussion it should be clear that interband tunnel devices are qualitatively different from conventional AlGaAs/GaAs resonant tunnel diodes. The difference between them is not simply that the bandgap of the well blocks the nonresonant current leading to extremely large PVR's. Because the effective mass of the mobile charges changes sign as they move across the structure, ITS are fundamentally different from conventional RTD's. In intraband structures 'individual' electrode states move in and out of resonance with the well as the voltage is increased. By contrast, a wide range of electrode states simultaneously resonate with the well in the interband case. As the bias is increased the overlap between the well and electrode states monotonically decreases. This leads to the conclusion that in interband devices the structure is still resonanting in the NDR region.

3.5 Barrierless Resonant Interband Transmission (BRIT) Structures

In this section we discuss barrierless resonant interband transmission (BRIT) structures. BRIT's consist of thin, undoped GaSb layers sandwiched between

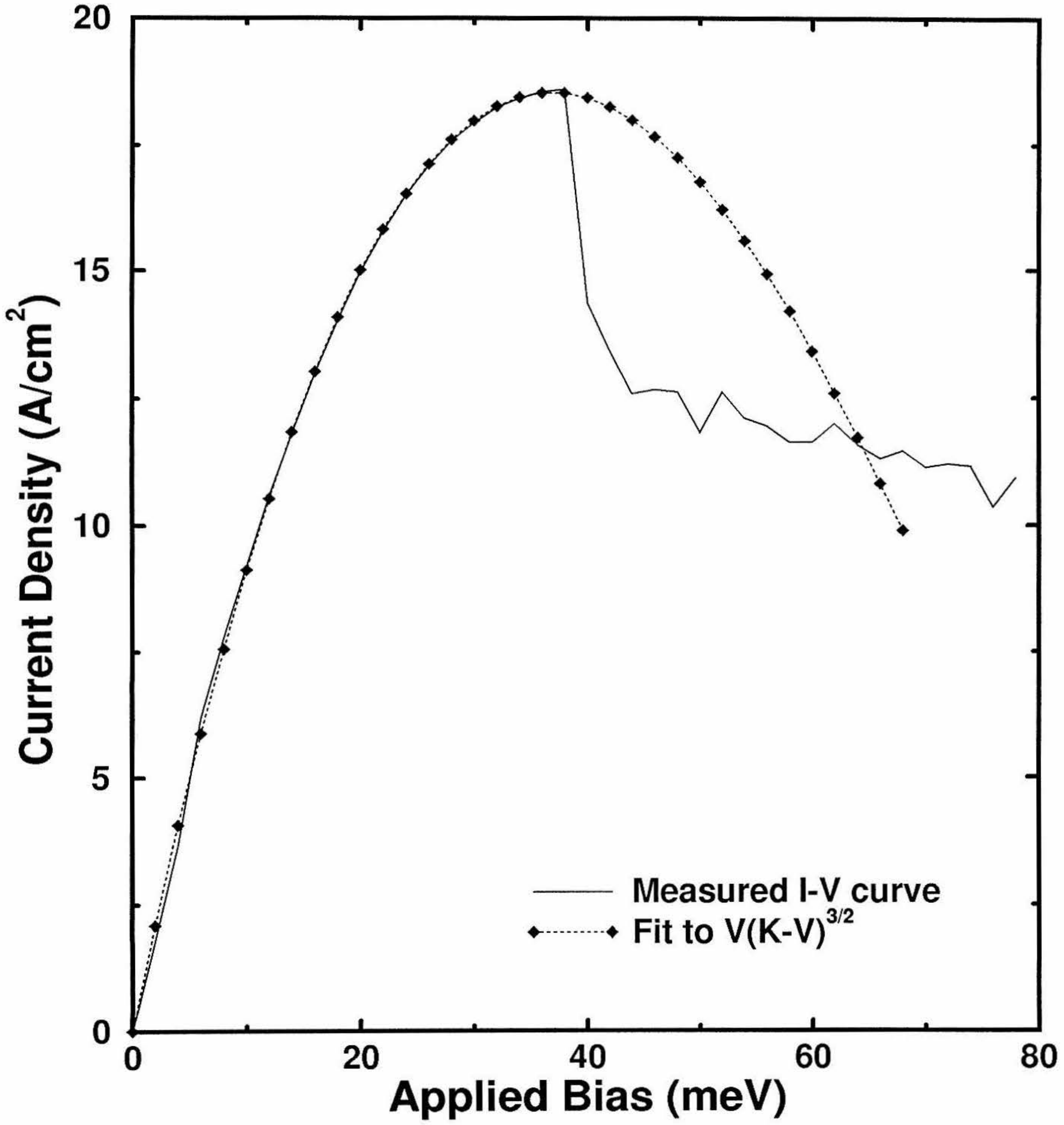

Figure 3.9: Plot of measured current density and data fit.

heavily doped InAs cladding layers. The central, GaSb, layers were 50 Å to 300 Å thick. These devices are a natural extension of the RIT's discussed in section 3.3; the difference being that the AlSb barriers are not present in BRIT's. Fig. 3.10 shows an energy bandedge diagram for a BRIT. The current transport mechanism in this device has been claimed by some investigators to be simply ohmic conduction between the InAs electrodes through the GaSb valence band[6]. However, our study of BRIT structures indicated that because of the different symmetries of the electronic wavefunctions in the InAs conduction band and the GaSb valence band, the charge carriers are partially confined in the GaSb. This confinement is due to the two partially reflecting InAs/GaSb interfaces in the structure in the same way that an optical resonator can be constructed from two half-silvered mirrors. These QBS in the GaSb valence band can give rise to resonances in the devices' transmission probability and hence NDR. In this section we present experimental evidence demonstrating the formation of these QBS, despite the absence of classically forbidden barrier regions in these structures, due to the imperfect coupling between the InAs conduction–band states and the GaSb valence–band states.

3.5.1 Experimental I-V Curves

Representative BRIT I-V curves taken at 300 K and 77 K are shown in Fig. 3.11. Approximately a dozen devices were grown, and the I-V curves of all the BRIT structures are qualitatively similar to this one. BRIT's with GaSb layers thicker than 70 Å showed NDR at room temperature with PVR's ranging from 1.6:1 to 3:1 and J_p's ranging from 1.5 to 6 $\times$ 10^4 A/cm^2. None of the device's I-V characteristics changed significantly between room temperature and 77 K indicating that thermionic currents are not important in these structures. The

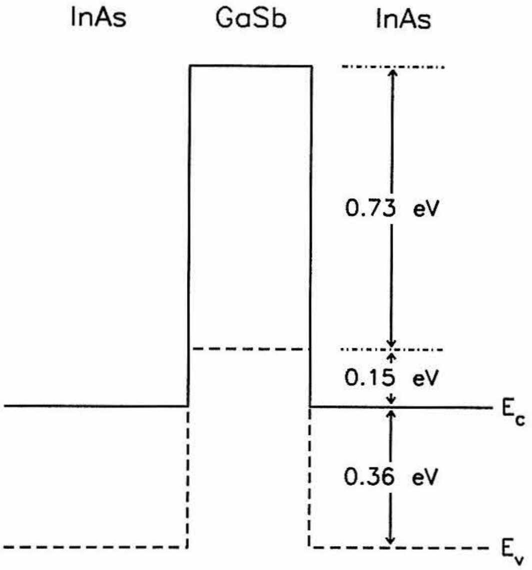

Figure 3.10: Schematic energy band diagram for the InAs/GaSb/InAs interband tunneling device. The conduction bandedge is indicated by the solid line, and the valence bandedge by the dashed line. The InAs/GaSb valence band offset is taken from Ref. [1].

increase in voltage of the position of the current peak at lower temperatures is due to an increase in parasitic and contact resistances as the devices are cooled. All of the devices had the asymmetric I-V curves shown in Fig. 3.11: higher J_p and lower PVR when electrons were injected into the crystal's surface and the opposite when electrons were extracted from the crystal's surface.

3.5.2 Origin of NDR in the BRIT Structure

An analysis of these devices reveals a number of interesting features. Because interband tunneling devices involve both conduction and valence band states, any model for these structures must include both bands and must correctly account for the interactions between these bands. A simple two–band tight–binding

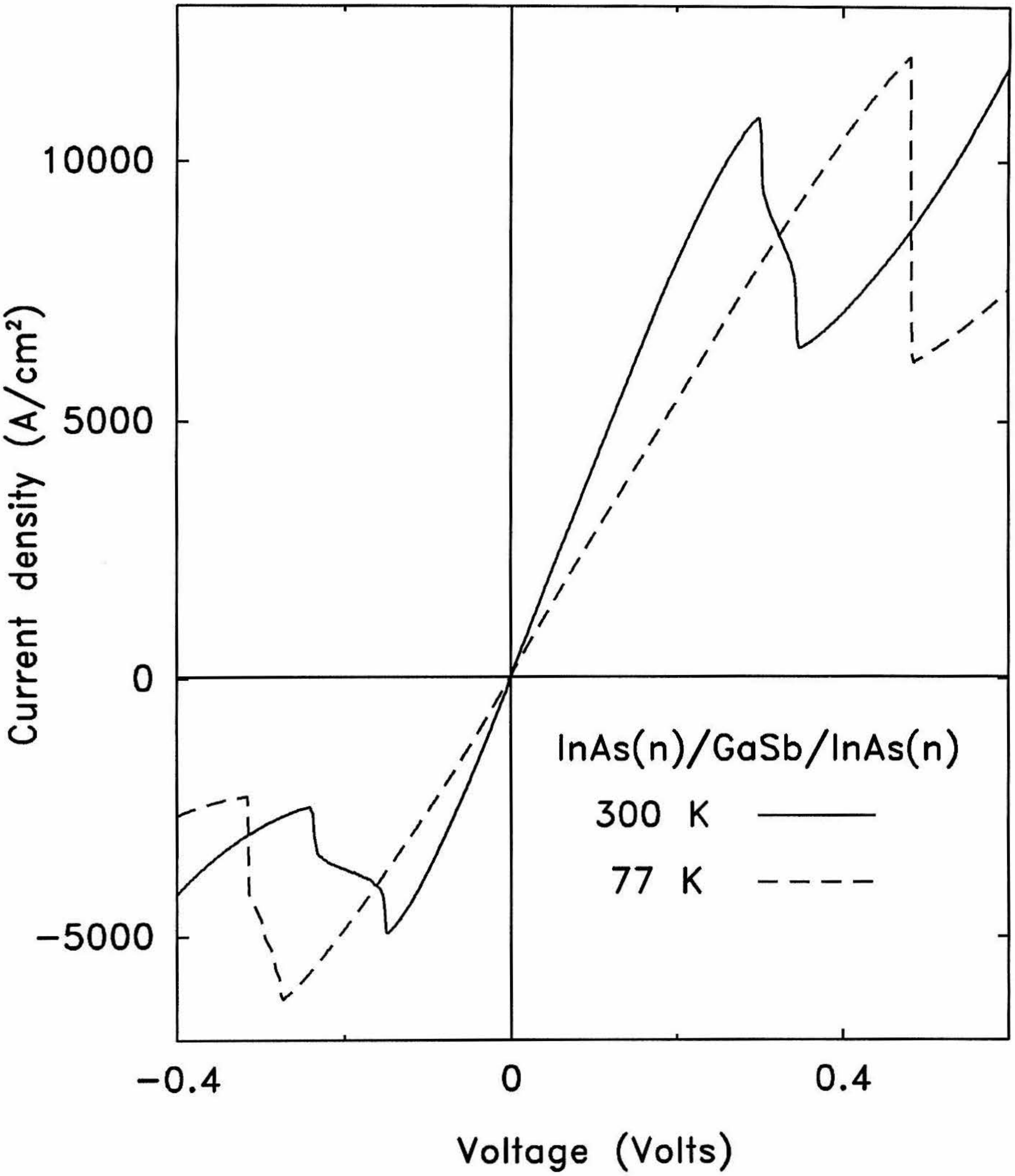

Figure 3.11: Current-voltage characteristics of the BRIT structure at room temperature and at 77 K.

model, incorporating the conduction and light–hole bands, that satisfies these requirements was developed by collaborators in order to understand better the experimental data.[7] The heavy–hole valence band was neglected, based on the assumption that the coupling between the conduction and heavy–hole bands was small. Later work by Ting *et al.* verified this assumption but showed that the strong interaction between the light and heavy–hole bands, away from the center of the Billion zone, meant that heavy–holes play an important role in current conduction across BRIT structures since they modify the energy and dispersion of the light hole band[8]. However, the two–band model, in conjunction with realistic band bending calculations, allows us to simulate quickly and semi-quantitatively the I-V characteristics of a wide variety of interband tunneling devices.

Growth, processing and measurement of a series of BRIT's with varying GaSb layer widths, and subsequent simulations of these devices provides strong evidence that current transport through the GaSb layer is indeed resonant. Fig. 3.12 shows calculated transmission coefficients in the energy range between the InAs conduction bandedge (0 eV) and the GaSb valence bandedge (0.15 eV) for devices with three different GaSb layer widths. The most striking feature is that, despite the absence of any classically forbidden barrier regions, transmission resonances are formed due to the two partially reflecting InAs/GaSb interfaces. For the 45 Å GaSb well (Fig. 3.12(a)), the quantum confinement energy places the QBS below the InAs conduction bandedge where it is inaccessible to electrons in the InAs electrodes. In this case, resonant transport cannot occur. For the 90 Å GaSb well (Fig. 3.12 (b)), a single broad resonance is present in the transmission coefficient. The 300 Å GaSb well (Fig. 3.12 (c)) has five narrower resonances between the InAs conduction band edge and the GaSb valence bandedge. This variation in the transmission coefficient leads to a strong dependence of J_p on the GaSb layer width. The absence of an accessible resonance should lead to very small currents

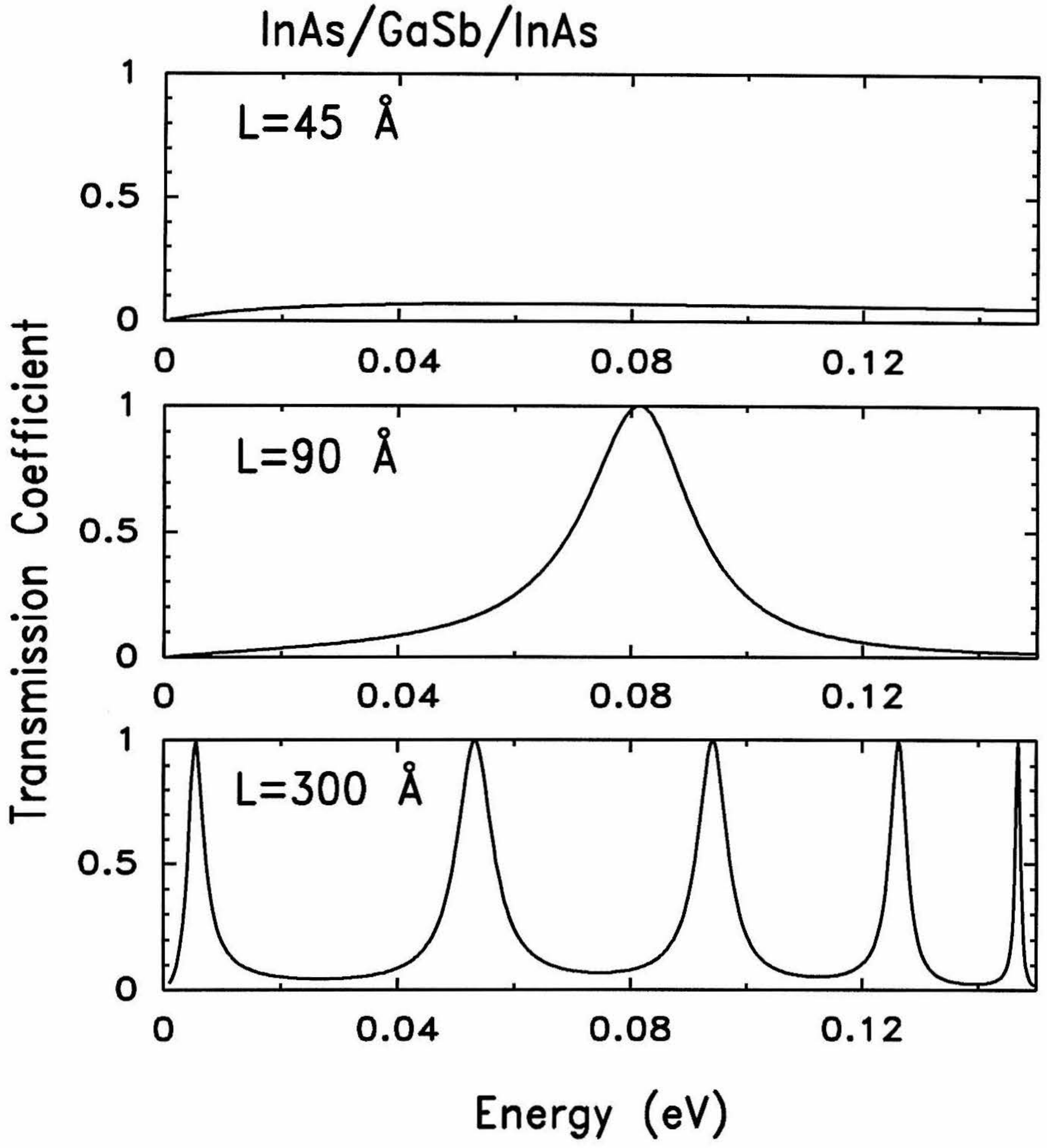

Figure 3.12: Theoretical transmission coefficients for InAs/GaSb/InAs interband tunneling devices for GaSb layer widths of (a) 45 Å, (b) 90 Å, and (c) 300 Å. On the energy scale shown, the InAs conduction bandedge is at 0 eV, and the GaSb valence bandedge is at 0.15 eV.

for devices with thin GaSb wells. Structures with intermediate GaSb layer widths should exhibit much higher resonant current densities, due to the presence of the single broad resonance. For wide GaSb layers J_p should decrease because the resonances are significantly narrower than for GaSb layers of intermediate width and therefore allow less of the incoming electron distribution to be transmitted across the GaSb layer.

Fig. 3.13(a) shows the calculated J_p's for BRIT's of varying GaSb layer thicknesses. Fig. 3.13(b) shows the difference between the peak and valley current densities experimentally measured for devices with different GaSb layer widths. The difference between the peak and valley current densities, rather than simply J_p, has been used in order to eliminate contributions to J_p from inelastic transport mechanisms, which were not included in calculations. Thermionic currents were ignored since Fig. 3.11 indicates their contribution to the non–resonant current is relatively small.

Both the experimental and the theoretical curves in Fig. 3.13 show the qualitative dependence on GaSb layer width expected from our analysis of the individual transmission coefficients of these structures. In particular, the sharp drop in the resonant current for narrow GaSb layers is strong evidence that the current flow in these devices is due to transport through a resonance in the GaSb layer, rather than simple ohmic conduction through the GaSb valence band that is eventually blocked by the GaSb band gap. If the transport mechanism were simply ohmic conduction, the current would not decrease sharply in devices with narrow GaSb layers. The quantitative discrepancy between the theoretical and experimental curves could arise from a number of factors. The calculated J_p's are quite sensitive to the separation between the InAs conduction bandedge and the GaSb valence bandedge, meaning that uncertainties of a few hundredths of an eV in the InAs/GaSb valence band offset, or small amounts of As incorporated into

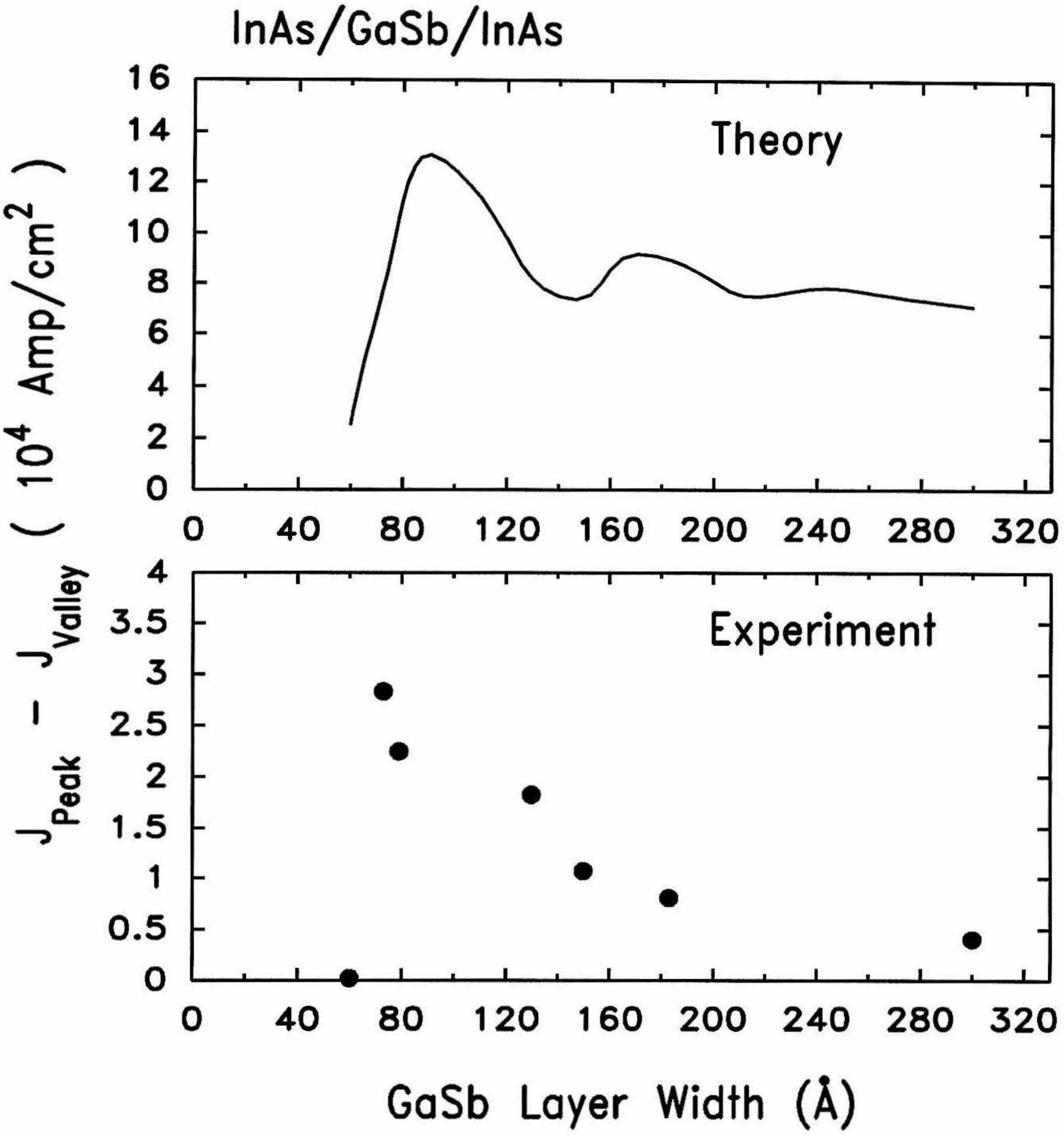

Figure 3.13: Theoretical calculations and experimental values for the difference between the peak and valley current density in BRIT's as a function of GaSb layer width. The sharp drop in current density for narrow GaSb layer widths is a result of the quasi–bound state in the GaSb layer moving below the InAs conduction bandedge in energy, and demonstrates the resonant nature of the current transport mechanism in this structure.

the GaSb layers, will significantly affect the quantitative agreement between theory and experiment. The qualitative behavior that we observe, however, should not be affected by these uncertainties. Taken together, the experiments and calculation show that a QBS is formed in these structures even though no classical barrier is present.

3.6 A Hybrid RIT/BRIT Structure

3.6.1 Experimental I-V Curves

In this section we will consider a structure which is a hybrid of the RIT and BRIT devices discussed in sections 3.3 and 3.5. The device consists of a GaSb well sandwiched between two InAs electrodes. A single AlSb barrier layer is grown between the GaSb well and one of the InAs electrodes. The band structure of the device corresponds to Fig. 3.2 (j). For convenience we will call this device the HYB or hybrid device.

The HYB is a hybrid of a RIT and a BRIT in the sense that the bound state in its GaSb valence band well is confined on one side by an AlSb barrier (which is RIT like) and by the mismatch between valence and conduction band states on the other (BRIT like). The difference between RIT-like confinement and BRIT-like confinement is important. For the case of a true barrier, the bound state is only a few μV wide, which is less than the Fermi spread of the cladding layer electrons. As a result, only a portion of the incident electrons can access the bound state. This reduces the device's resonant current. Inelastic currents are suppressed for the same reason. The net result of narrowing the resonance is to decrease the device's J_p's but to increase its PVR. BRIT's on the other hand have extremely broad resonances ($\sim$ 10 meV), which explains their much larger J_p. BRIT PVR's are much smaller, however, since the broad transmission resonance is not as effective at suppressing nonresonant currents. The HYB was grown in order to explore the effect of the resonance width on current conduction.

Two HYB's having the same well width were grown. In one of the devices the AlSb barrier was placed on the substrate side of the GaSb well. In the other HYB, the AlSb barrier was grown on the surface side of the well layer. Both geometries were grown to ensure that we could distinguish between asymmetries in the devices' I-V curves due to the barrier placement and those due to doping asymmetries or the phenomena of inverted interfaces.

Fig. 3.14 shows the room temperature I-V curves for the two structures. For both I-V curves, positive applied bias is defined as the top of the device mesa being at a higher potential than the substrate. In other words, positive applied bias means that electrons are extracted from the top of the device mesas. Negative bias means that electrons are injected into the surface of the crystal and extracted from the substrate. For the upper I-V curve, whose AlSb barrier is on the surface side of the GaSb well, a positive applied bias transports electrons from the substrate side InAs electrode, into the GaSb well, across the AlSb barrier and back into the conduction band of InAs. When a negative bias is applied to the device in Fig. 3.14, electrons encounter the AlSb barrier before the GaSb well. In the lower curve, the AlSb barrier is on the substrate side of the GaSb well. Applying a positive bias to this device means that the electrons encounter the barrier before the well layer.

Both of the I-V curves are asymmetric as might be expected since the device itself is asymmetric. However, the two I-V curves are virtually identical if reflected about the line $y = -x$. This indicates that any growth asymmetries that may be present have a small effect on the I-V curves. After examining the curves in Fig. 3.14 the real motivation for considering these devices to be RIT/BRIT hybrids is apparent. Both of the I-V curves look RIT-like (see Fig. 3.4) in one bias direction, and BRIT-like (see Fig. 3.11) for the opposite applied bias. Because this behavior is evident in both structures, it is not an artifact of the growth. The shape of the I-V curve depends on whether the electrons encounter the AlSb barrier before or after the GaSb well.

3.6.2 Origin of the Asymmetry in the I-V Curves

To understand the origin of the asymmetry in the I-V curves it is necessary to look at the devices' transmission coefficients. In Fig. 3.15 we plot the transmission probability through a HYB. The zero of the energy scale is chosen to be the conduction bandedge of InAs. Two transmission curves are shown for devices under an applied bias. The lower energy resonance corresponds to the case of the barrier side of the GaSb well being at a higher potential than the GaSb/InAs interface. The high energy resonance is for the opposite case. Simple sketches of the band structure of the two calculated cases, along with the direction of electron travel, are inset in the figure. From the plotted curves, it is clear that the transmission probability across the device depends on the direction of electron travel once a bias is applied. (Of course, with no bias the transmissions must be identical or there would be current conduction without an applied voltage.)

The magnitudes of the calculated resonance curves are consistent with the asymmetric I-V's shown in Fig. 3.14. The calculation shows that the magnitude of the transmission probability is smaller and the resonance occurs at lower voltages when the electrons tunnel across the barrier into the well. This corresponds to negative applied bias in the upper and positive voltages in the lower panels of Fig. 3.14 respectively. When the electrons must tunnel across the barrier to leave the well, the device is more conductive and the resonance occurs at larger

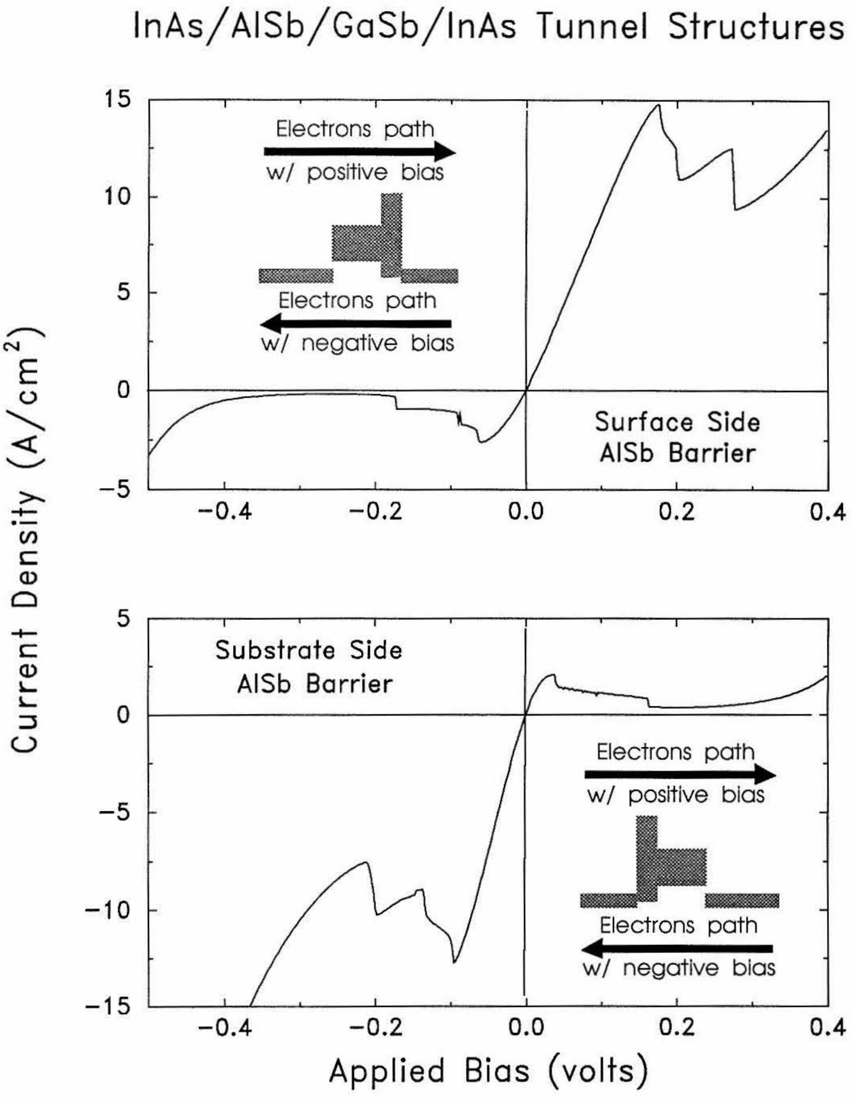

Figure 3.14: Room temperature I-V characteristics for the hybrid RIT/BRIT device. The device consists of a GaSb well between a pair of n-InAs electrodes. An AlSb barrier layer is inserted between one of the electrodes and the InAs well. Positive applied bias corresponds to electrons being extracted from the top of the device mesa. Negative bias corresponds to electrons being injected into the surface side of the crystal.

applied voltages. This corresponds to positive (negative) voltage in the upper (lower) panel in Fig. 3.14. The experimental I-V curves qualitatively agree with the conduction asymmetry predicted by the calculation.

An examination of the device's band diagram under bias leads to an intuitive understanding of the conduction asymmetry shown in both the experimental and theoretical curves. The voltage difference between the current peaks in the two cases is a result of the bias that is dropped across the AlSb barrier. In the calculation, the effect of the applied bias is approximated by a linear voltage drop across the barrier and well. This is a reasonable assumption since both the barrier and well are undoped, and lifetime of the QBS in the GaSb well is a few picoseconds.[8] Therefore, in the case of the left-hand inset in Fig. 3.15 the energy difference between the InAs conduction bandedge and the QBS will be decreased by the voltage that is dropped across the barrier. For the right-hand inset, the voltage across the AlSb barrier will not affect the conduction-band edge, bound state energy separation. This means that the current peak will occur at lower applied voltages for the bias corresponding to the left-hand inset in Fig. 3.15 as shown in the data. The separation between the peaks is much larger in the experimental data than in the calculation. This is partially due to series resistance. In the more conductive bias direction, which has the higher energy bound state, the increased current leads to a larger voltage drop across the parasitic series resistance that is present in all real devices. This magnifies the energy shift in the resonance position.

The difference in PVR's shown in Fig. 3.14 is attributed to the leaky InAs/GaSb interface. The large valley currents when the device is biased as in Fig. 3.16 (b) are due to nonresonant processes. Since there is not a true barrier between the source electrode and the bound state, electrons are easily scattered between them leading to large inelastic currents. Once carriers are in

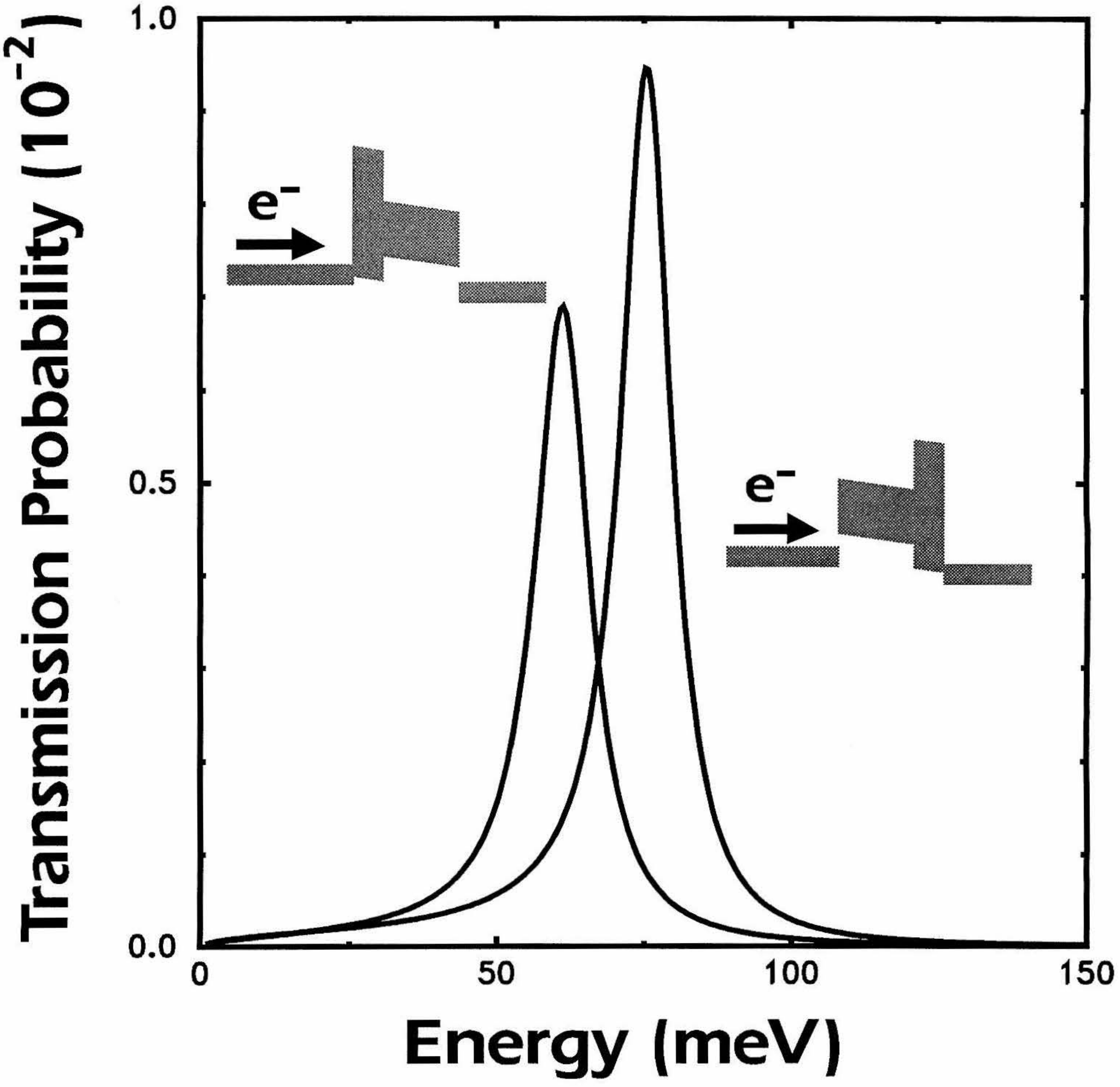

Figure 3.15: Calculated transmission coefficients, under an applied bias, for the hybrid structure whose I-V curves are shown in Fig. 3.14. The magnitude and position of the calculated transmission resonances depends on the direction the electrons are traveling. The transmission asymmetry matches and explains the corresponding I-V curves.

the bound state, they can easily continue across the device since by definition they are on resonance. This leads to small PVR's for voltages corresponding to Fig. 3.16 (b). For bias leading to Fig. 3.16 (a), however, the AlSb barrier strongly suppresses scattering between the source electrode and well state. This greatly reduces the valley current and leads to the large PVR's shown in the data. The above analysis suggests that in a general resonant tunneling device, the barrier between the source electrode and well largely determines the structure's PVR. More directly, this says that once carriers get "into" a well, it is easy for them to get "out" the other side.

The asymmetry in the J_p's is partly a result of the larger inelastic currents present in Fig. 3.16 (b). However, both the calculated resonance and the experimentally measured change in current density across the NDR region are larger for Fig. 3.16 (b). Both the calculation and measurement suggests that when the device is biased as in Fig. 3.16 (b), it is more conductive than Fig. 3.16 (a). Inspection of the two band diagrams under bias suggests that in Fig. 3.16 (a) the bandgap of the GaSb well partially impedes conduction at resonance. In summary, while the HYB structure is not fundamentally different from the RIT and BRIT structures, a detailed analysis of its I-V curves helps in understanding the basic properties and mechanisms of interband tunneling.

3.7 Heterojunction Esaki Diodes (HED)

In this section we report the experimental observation of NDR in a device consisting of a single InAs/GaSb interface which we call a heterojunction Esaki diode (HED). Two types of HED's were grown. The first consisted of 2000 Å of p-type GaSb grown on 7000 Å of n-type InAs which was deposited on an insulating GaAs substrate. The second device was identical expect that 100 Å

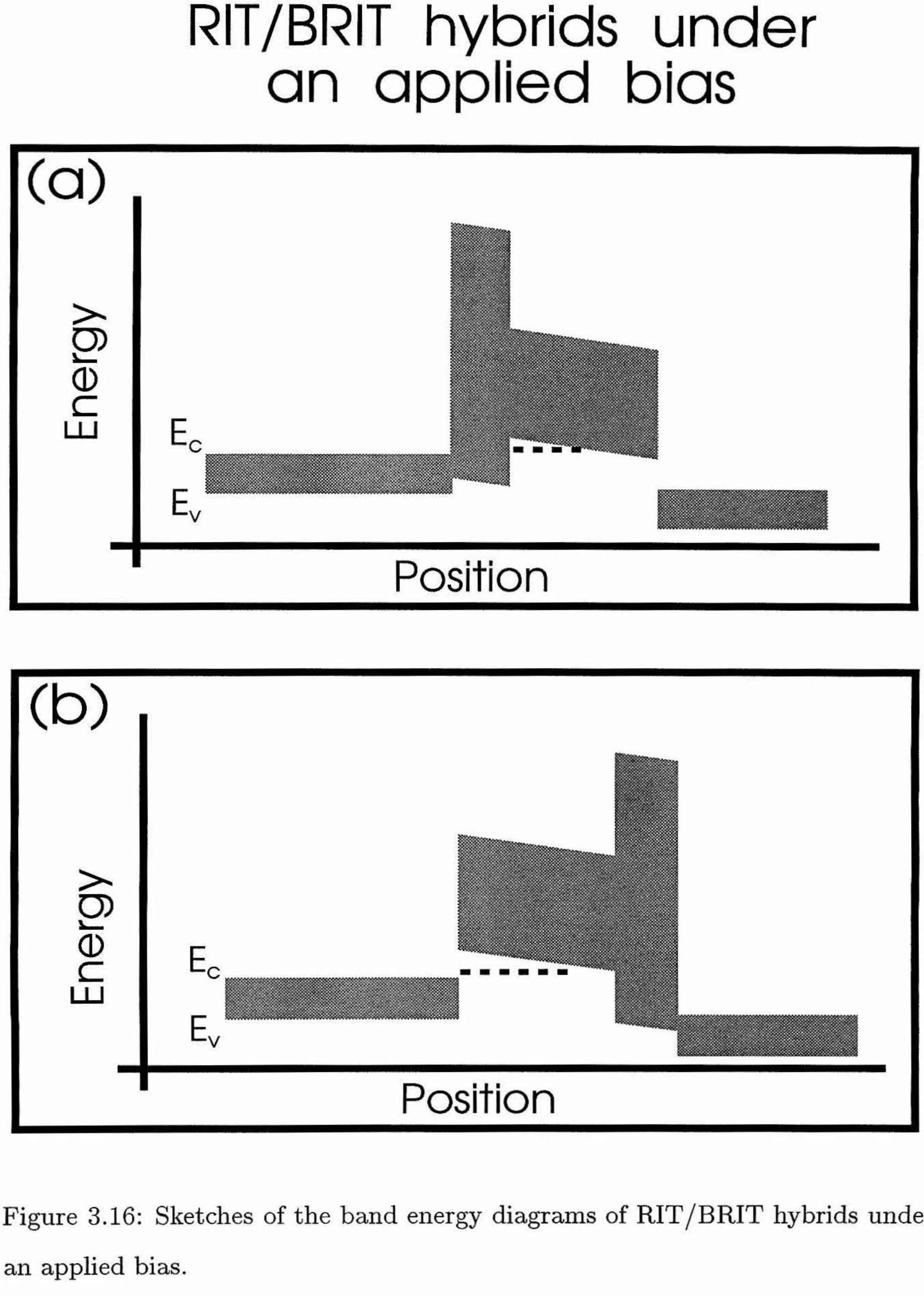

Figure 3.16: Sketches of the band energy diagrams of RIT/BRIT hybrids under an applied bias.

of undoped material was grown on either side of the InAs/GaSb interface. The structures were terminated with GaSb so that after processing, lateral conduction will be through the lower resistance InAs. The devices had room temperature NDR in forward bias, with J_p's of 8.2x10^4 A/cm^2 and 4.2x10^4 A/cm^2 for structures with and without undoped spacer layers on each side of the heterointerface, respectively. These J_p's represent an average over 25 randomly chosen devices, with a standard deviation in the measured value of ~0.2x10^4 A/cm^2. The room temperature PVR ranged from 1.1:1 to 1.5:1 with the doped interface giving the higher value. In 1977 Sakaki *et al.* measured the I-V curves of a structure with an $In_{.84}Ga_{.16}As/GaSb_{.9}As_{.1}$ interface, but did not observe NDR.[9] We believe that this was due to the fact that the mesas they fabricated had a device area over 250 times larger than the ones reported here. Because of the large current densities found in these structures (which are comparable to those measured by Sakaki *et al.*) it is essential to fabricate small area devices so that ohmic heating due to contact and parasitic series resistance does not destroy the device before it can be biased into the NDR region.

3.7.1 Origin of NDR in the HED Structure

The mechanism that causes NDR in this structure is identical to that of an Esaki diode (hence its name.) The difference between a HED and a conventional Esaki diode is the depleted region that separates the n-type and p-type portions of the crystal. Figs. 3.17(a) and 3.17(b) are respectively a band edge diagram for the structure and the calculated transmission coefficient at flat band. The transmission probability is found from a two band model incorporating electrons and light holes.[7] The calculated transmission coefficient does not have a Lorentzian lineshape, showing that the device does not have a QBS, as in traditional resonant tunneling structures. However, the modulation of the structure's transmission coefficient as shown in Fig. 3.17(b) indicates that current conduction in the device is not merely ohmic in nature. The calculation also shows that the InAs/GaSb interface is reflective as the results of section 3.5 indicated. The NDR observed in the structure is due to the GaSb band gap blocking the current channel in a manner similar to that of a forward biased, p^+-n^+ junction tunnel diode.

3.7.2 Experimental I-V Curves

In Figs. 3.18 and 3.19 we show representative I-V curves for the structures with and without the undoped spacer layers, respectively. Both devices show NDR at room temperature with peak current densities greater than $8.2\text{x}10^4$ ($4\text{x}10^4$) A/cm^2 for the structure with (without) undoped spacer layers at the heterointerface. I-V curves are shown at both 77 K and room temperature. The fact that the device's performance is virtually unchanged at the lower temperature indicates that thermionic emission plays only a minor role in the large valley current. The low temperature I-V curves are shifted to slightly higher bias due to the higher contact and cladding layer resistances present at 77 K.

The valley currents in these structures are surprisingly large considering that they should be blocked by the GaSb bandgap. However, because there is not a true barrier between the InAs conduction band and the GaSb valence band (see Fig. 3.17(b)), there is little to suppress inelastic processes from scattering electrons from the InAs conduction band into the GaSb valence band. The lack of a barrier layer causes the small PVR's observed in this device.

It is interesting to note that for the two different devices shown in Figs. 3.18 and 3.19, the difference between the peak current and the minimum valley current is almost identical. The absolute size of the current change in the NDR region

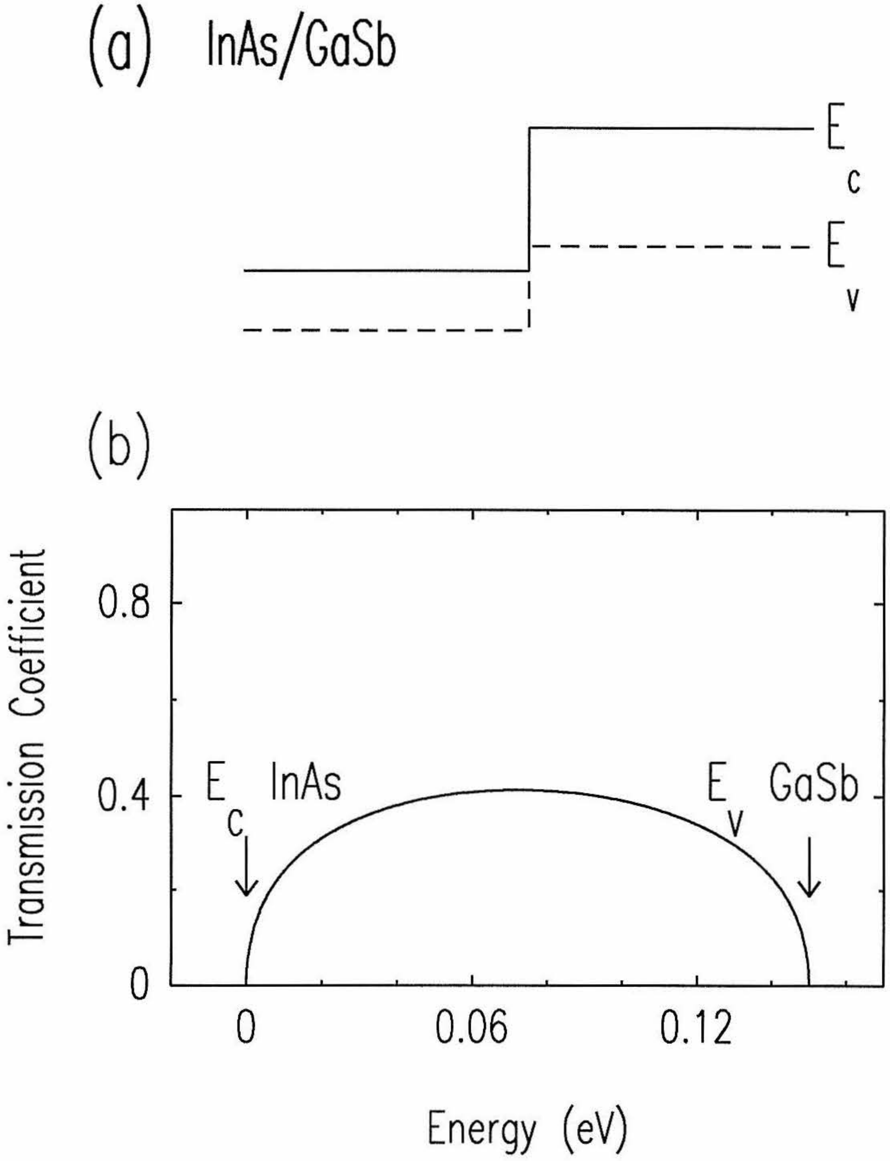

Figure 3.17: a) Schematic bandedge diagram (neglecting band bending) of a heterojunction Esaki diode (HED). b) Theoretical calculation of the transmission coefficient across the structure. The zero of energy is taken to be the InAs conduction band.

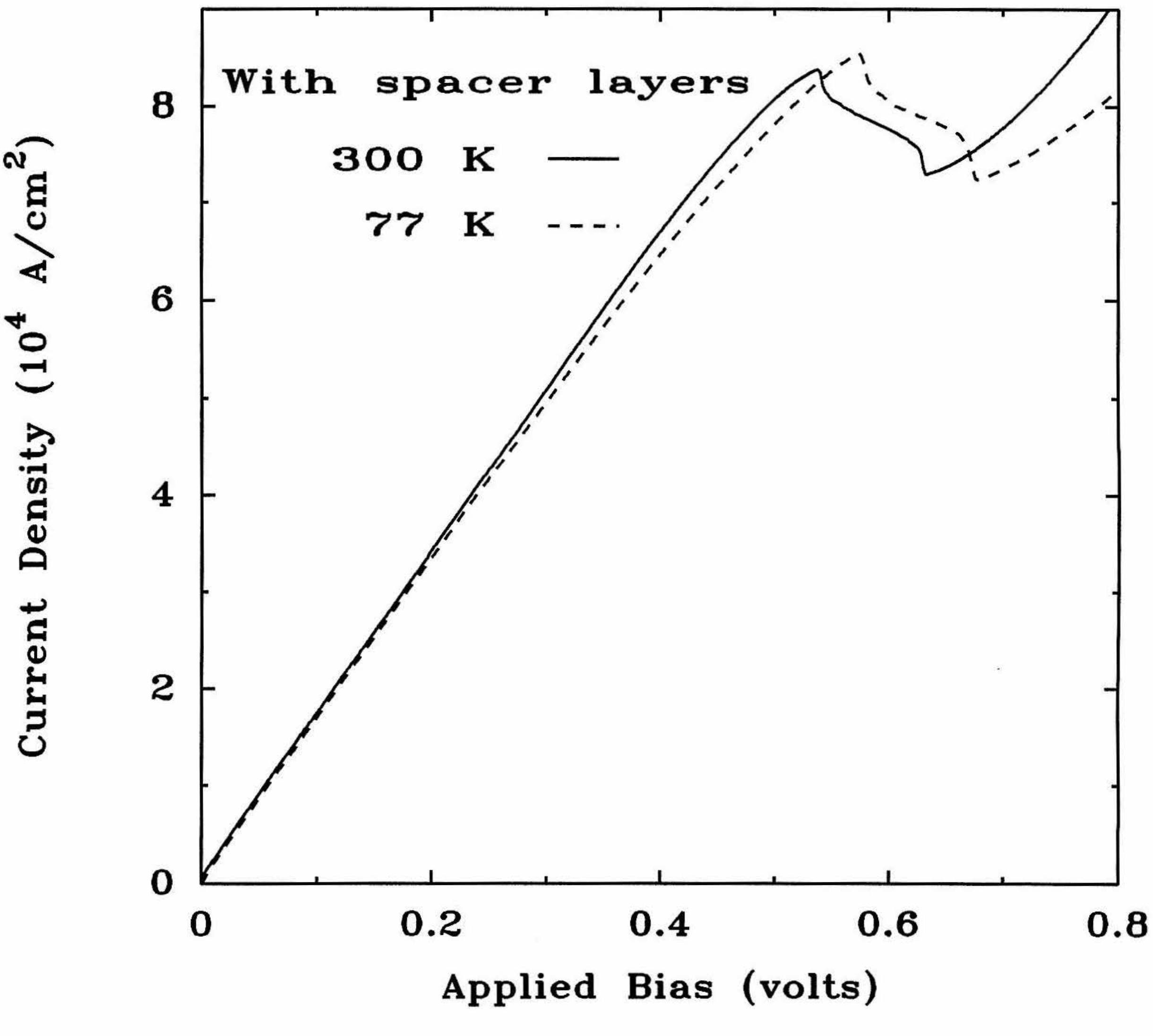

Figure 3.18: Representative I-V curves from a HED structure with undoped spacer layers on both side of the InAs/GaSb interface. The solid line was taken at room temperature and the dashed at 77 K.

seems to be fixed. The difference between the I-V curves of the two devices is the value of the small bias resistance and the applied voltage at which NDR occurs. The device in Fig. 3.19, which has undoped layers, is more conductive and NDR occurs at a larger applied bias. This is due to the different doping profiles of the two structures which changes the band bending at the InAs/GaSb interface.

Because the NDR observed in these devices is not associated with a QBS which may have a long lifetime, this device holds promise for the fabrication of high frequency oscillators. The intrinsic upper limit of this structure's oscillation frequency will be determined by the transit time across the heterointerface and the inherent frequency response of the materials. Furthermore, because this device can be grown without undoped spacer layers, limiting processes such as transit time delays across depleted regions which are important in conventional double barrier structures will be eliminated in this device.[10] For this structure to prove useful, however, it will be necessary to improve the PVR to 2 or greater. It may be possible to achieve this by optimizing the structure's doping profile or by tuning the bandgaps and offset at the heterointerface by using $\mathrm{Al}_w\mathrm{Ga}_{1-w}\mathrm{As}_x\mathrm{Sb}_{1-x}/\mathrm{In}_y\mathrm{Ga}_{1-y}\mathrm{As}_z\mathrm{Sb}_{1-z}$. Further, it should be pointed out that there is ~ 0.6 % lattice mismatch between InAs and GaSb. From this we estimate that the critical thickness for GaSb grown on InAs will be on the order of several hundred angstroms which is much less than the thickness of the GaSb epilayers reported on here. Due to this we anticipate misfit dislocations at the InAs/GaSb interface and threading dislocations in the GaSb epilayers which may degrade device performance. By growing thinner layers it should be possible to reduce or even eliminate the number of these interfacial misfit dislocations and potentially enhance device performance.

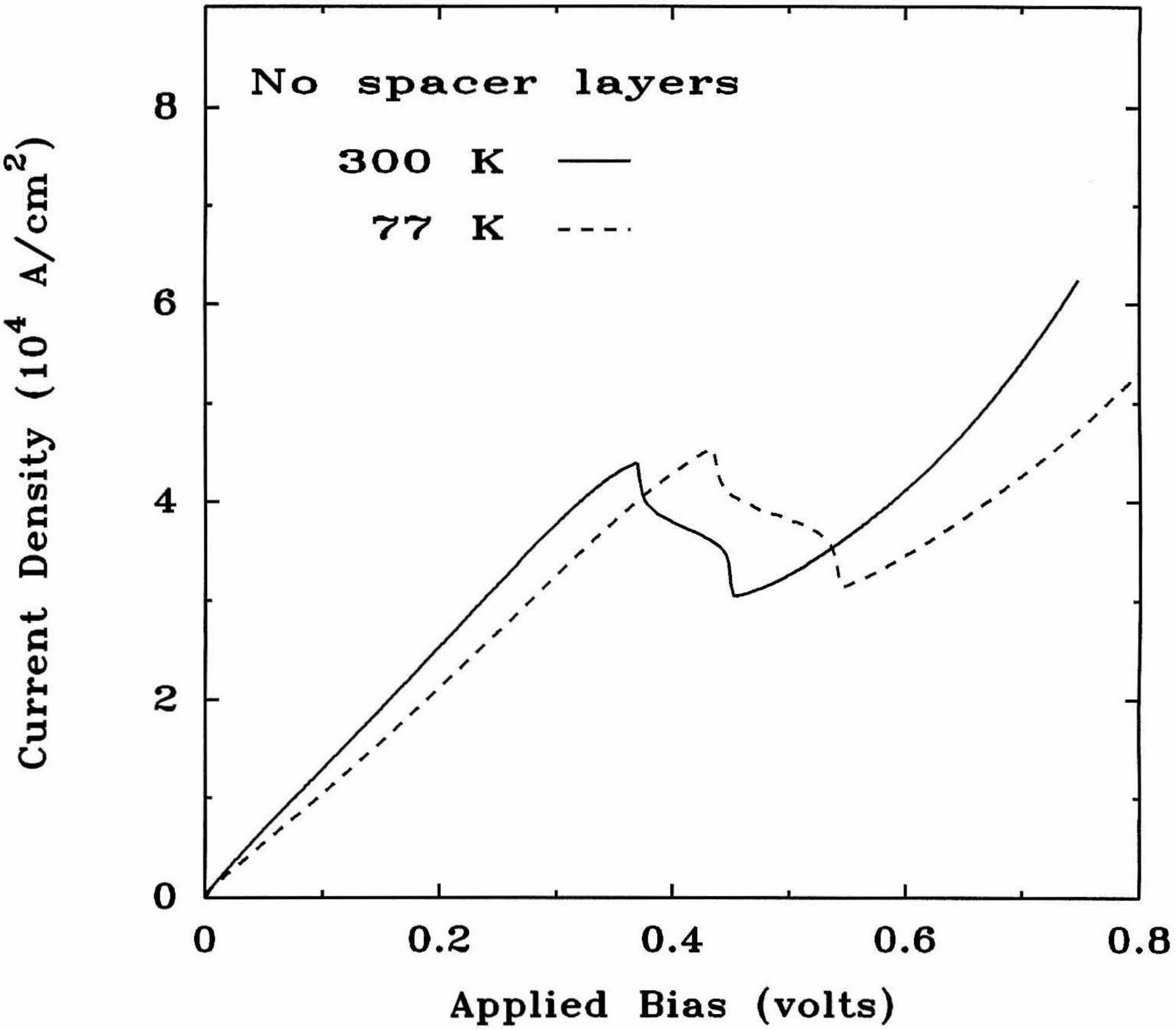

Figure 3.19: Representative I-V curves from a HED structure which did not have any undoped regions. The solid line was taken at room temperature and the dashed at 77 K.

3.8 Resonance Enhanced Heterojunction Esaki Diodes

The structures discussed in this section can be thought of as modified HED's. Fig. 3.20 shows schematic bandedge diagrams of the HED structure from section 3.7 (Fig. 3.20(a)), and the devices covered here (Figs. 3.20(b) and 3.20(c)). The three structures in Fig. 3.20 are very similar. In the two lower energy band diagrams, a thin AlSb barrier layer is inserted into the device away from the InAs/GaSb interface. Based on the results of the previous section, all three structures depicted in Fig. 3.20 would be expected to display NDR when sufficient positive bias is applied to the GaSb(p) electrode to shut off elastic transport of electrons from the InAs(n) electrode into available GaSb states. In this section, we give evidence for the formation of a QBS between the InAs/GaSb interface and the AlSb barrier. This quantum effect results in a resonant enhancement of current transport as compared to the HED structure depicted in Fig. 3.20(a). For this reason the devices in Figs. 3.20(b) and 3.20(c) will be referred to as resonant heterojunction Esaki diodes (RHED).

Table 3.2 gives the layer sequences and thicknesses for the samples discussed in this section. Sample D1 corresponds to the bandedge diagram in Fig. 3.20(a). Fig. 3.20(b) corresponds to sample D2 and samples D3 and D4 are shown in Fig. 3.20(c). In all the samples, the InAs electrode is degeneratly doped n-type while the GaSb electrode is p-type. In samples D2, D3 and D4, the AlSb layers, quantum wells, and an additional 100 Å spacer layer on the InAs sides of the active regions were undoped. There were no undoped layers in sample D1.

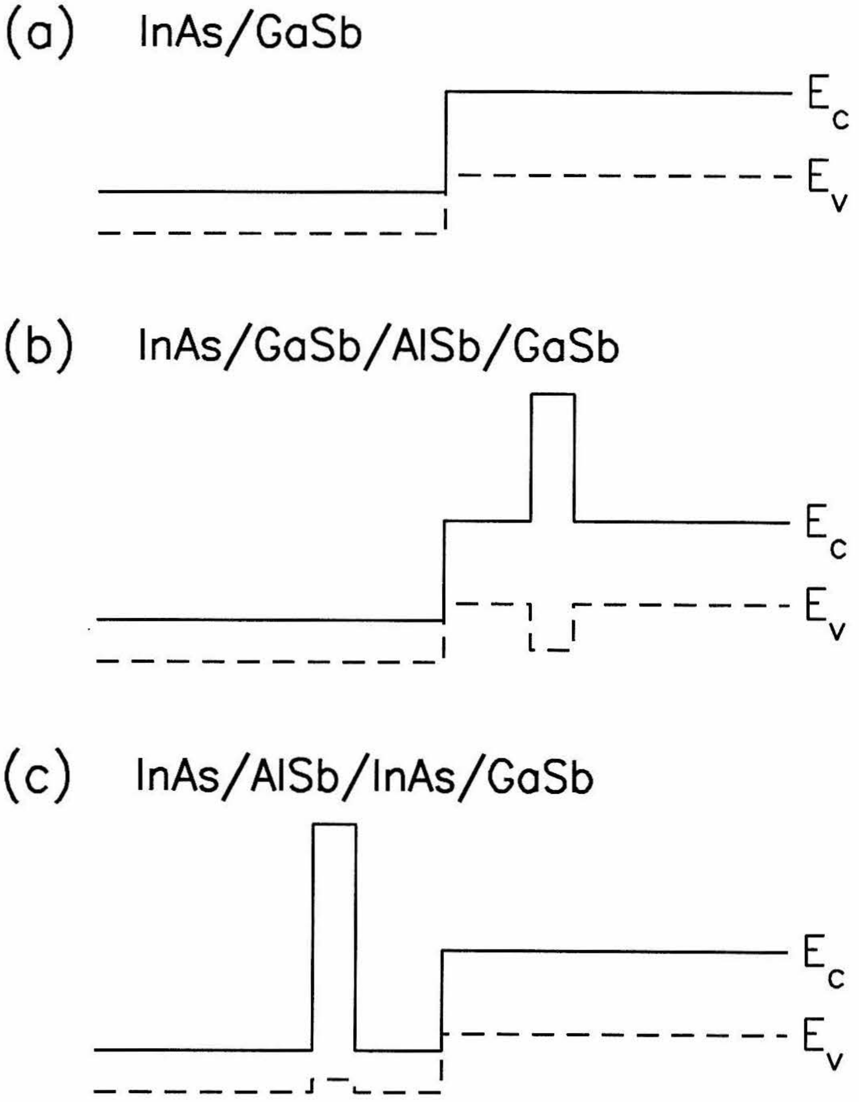

Figure 3.20: Schematic bandedge diagrams for (a) an InAs(n)/GaSb(p) interface (HED), (b) an InAs(n)/GaSb/AlSb/GaSb(p) heterostructure (RHED), and (c) an InAs(n)/AlSb/InAs/GaSb(p) heterostructure (RHED). In all three diagrams, the conduction (E_c, solid) and valence (E_v, dashed) bandedges are shown. The insertion of the AlSb barrier layers in (b) and (c) is hypothesized to create quasi–bound states in the regions between the AlSb barrier and the InAs/GaSb interfaces leading to a resonant enhancement of the current.

Sample Number	Band Diagram	Layer Sequence
D1	Fig. 3.20(a)	InAs(n)/GaSb(p)
D2	Fig. 3.20(b)	InAs(n)/GaSb(51 Å)/AlSb(12 Å)/GaSb(p)
D3	Fig. 3.20(c)	InAs(n)/AlSb(21 Å)/InAs(120 Å)/GaSb(p)
D4	Fig. 3.20(c)	InAs(n)/AlSb(21 Å)/InAs(80 Å)/GaSb(p)

Table 3.2: Material sequences and layer thicknesses of the samples discussed in this section.

3.8.1 Experimental I-V Curves

Fig. 3.21 shows representative I-V curves (positive bias on the GaSb(p) electrodes) taken at room temperature for samples D1 (dashed) and D2 (solid). The peak current density is much larger in sample D2 ($\approx 1.6 \times 10^5$ A/cm^2) than in sample D1 ($\approx 0.4 \times 10^5$ A/cm^2) even though a barrier layer has been added to sample D2. RHED's complimentary to D2 were also grown and characterized. Room temperature I-V curves from D3 and D4 are shown in Fig. 3.22. Here the AlSb barrier is placed on the opposite side of the InAs/GaSb interface as compared to D2. As shown in Fig. 3.22, D3 shows NDR with a PVR of 1.5:1 and a J_p of 6.7×10^3 A/cm^2. (The AlSb layer in D3 and D4 is thicker because of the complications involved in growing the mixed anion InAs/AlSb interface. This issue is covered in detail in Chapters 5 and 6.) The different I-V characteristics of D3 and D4 and their lower J_p as compared to D2 is due to the resonant nature of current transport in RHED's. This is explained in Section 3.8.2. For now the important thing is that, as Figs. 3.21 and 3.22 show, RHED's show room temperature NDR and can have current densities larger than HED's eventhough they have an additional AlSb barrier. This result suggests that adding the barrier layer creates a QBS in these devices.

3.8.2 Origin of NDR in the RHED Structure

Fig. 3.23 displays transmission coefficients for samples D1 (dashed) and D2 (solid), calculated at flat band conditions using a two-band model which incorporates electrons and light holes[7]. In the figure, the zero of energy is taken to be the InAs conduction bandedge. At resonance, the reflection coefficient for the carriers in sample D2 nearly vanishes. In contrast, significant reflection occurs at all energies for a single InAs(n)/GaSb(p) interface, due to the imperfect coupling of InAs conduction-band states with GaSb valence-band states. Fig. 3.23 shows that sample D2 possesses a wide transmission resonance which peaks well above the maximum transmission probability for the single InAs(n)/GaSb(p) interface. The formation of this QBS in the RHED explains why it is more conductive than a simple InAs/GaSb interface. The observed enhancement in J_p in sample D2 again indicates that reflection coefficients at the InAs/GaSb interface are not negligible (see sections 3.5.2 and 3.6.2). The formation of a QBS in the quantum well of this structure is dependent upon non–negligible reflections at the interfaces (a Fabry–Perot effect).

It may not be obvious that the enhanced current density observed in sample D2 is due to a resonant state. The difference between the peak and valley currents in D1 and D2 is rather small, and it could be argued that the difference in current density between D1 and D2 is caused by an inelastic process. However, as pointed

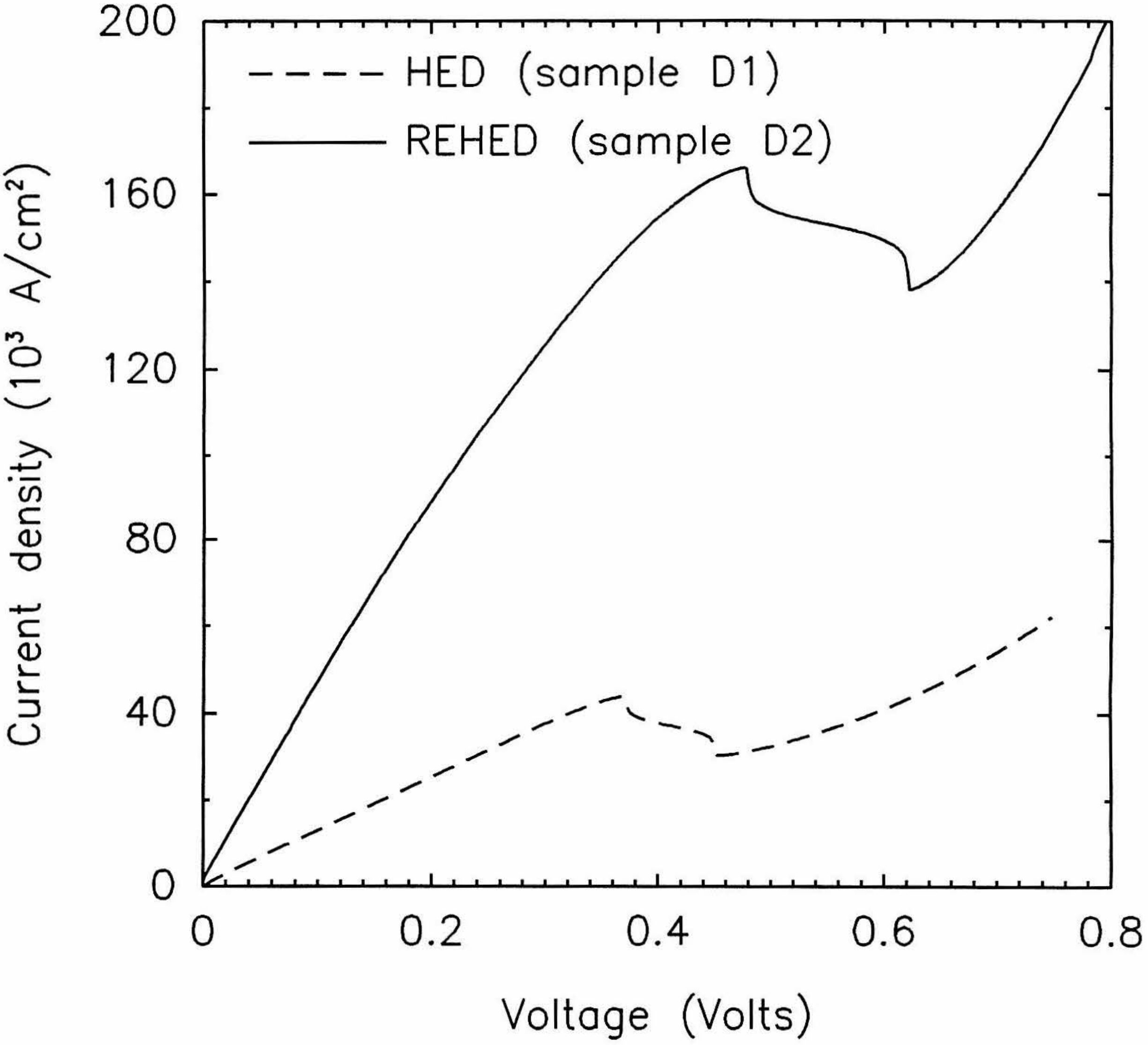

Figure 3.21: Current density vs. applied bias for samples D1 (dashed) and D2 (solid). The enhanced current density in sample D2 is consistent with resonant tunneling via a quasi–bound state in the GaSb quantum well.

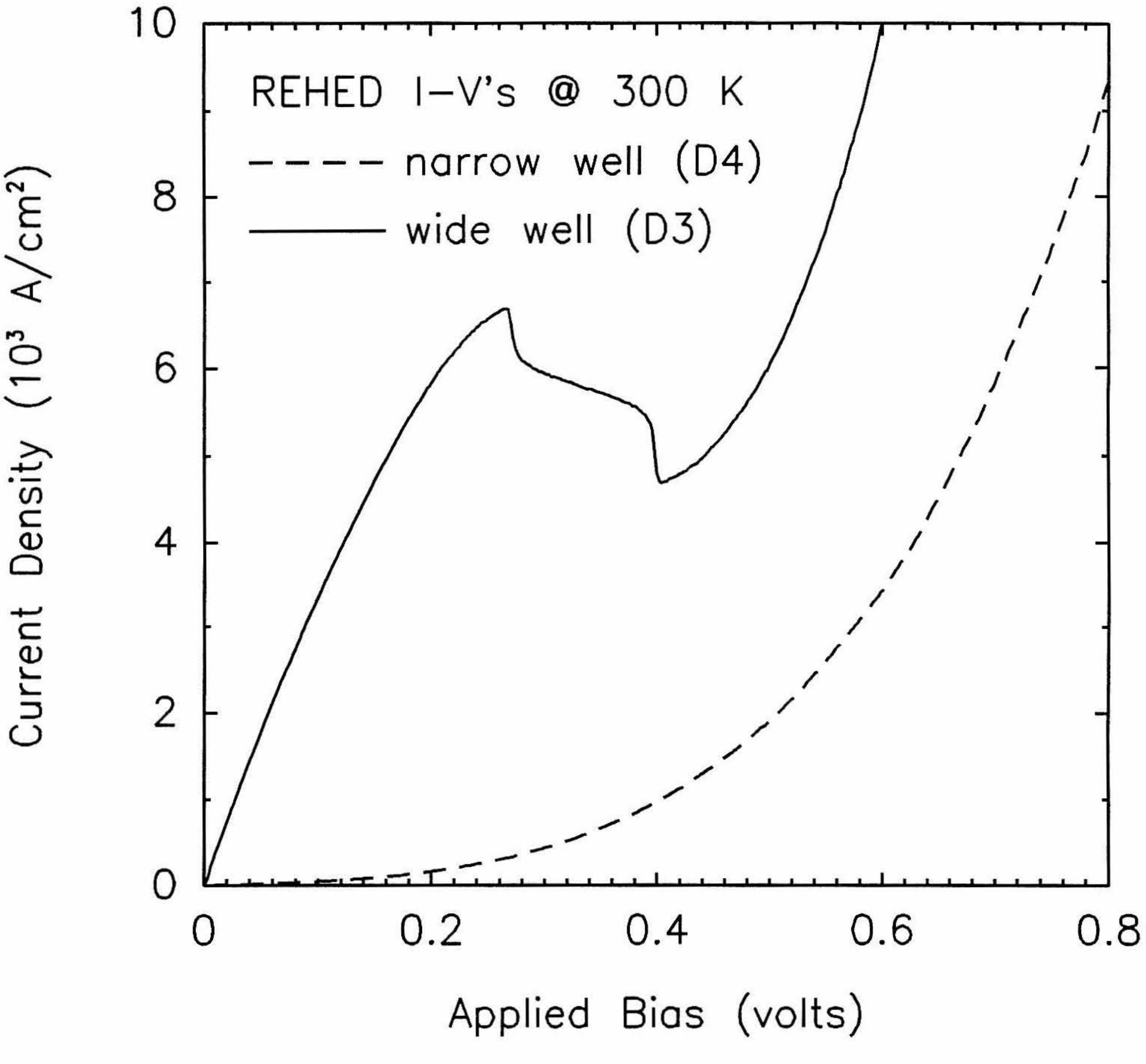

Figure 3.22: I-V curves for RHED devices with different well widths. The only difference between the two devices is the width of the InAs well. A resonance forms between the AlSb barrier and the InAs/GaSb interface in both structures. In the case of the narrow well, the confinement energy of the quasi-bound state pushes it above the GaSb valence bandedge where it is not accessible to electrons in the InAs electrode.

out in section 3.4, because the sign of the effective mass in valence-band and conduction-band states is different, interband tunnel devices are on resonance at zero applied bias. All of the RHED's grown had smaller resistances at low bias than the HED's. This is true even in devices that had J_p's less than that of sample D1. Further, the difference between the peak and valley currents in all of the RHED's that showed NDR was greater than the change in current observed in the HED's investigated. Taken together, these indicate that a QBS does form in the RHED's.

The data shown in Fig. 3.22 is a further test of whether a QBS does form in RHED's. Samples D3 and D4 are identical except for the separation between the AlSb barrier and the InAs/GaSb interface. If a resonant state does form in this region, these devices will be very sensitive to the size of this separation. To first order, the confinement energy of a bound state will vary as $1/L^2$, where L is the dimension of the confined region. If the size of this region – in the InAs conduction band for samples D3 and D4 – is too small, then quantum confinement will increase the energy of the state to the point where it is no longer accessible. For samples D3 or D4, this would mean pushing the QBS in the InAs conduction-band up above the valence-band minimum of the adjoining GaSb layer. In this case the AlSb layer and the InAs layer sandwiched between it and the GaSb electrode will function as a thick barrier for electrons in the InAs electrode since there will not be any available states in the InAs well. Because of this, devices with sufficiently thin InAs wells will not show NDR while devices with wider InAs wells will. This is exactly the result shown in Fig. 3.22 and similar to the change in BRIT current density as a function of GaSb well width discussed in section 3.5.2.

Fig. 3.24 shows plots of the calculated J_p for the structures depicted in Figs. 3.20(b) and 3.20(c) as functions of the separation between the AlSb barrier layer

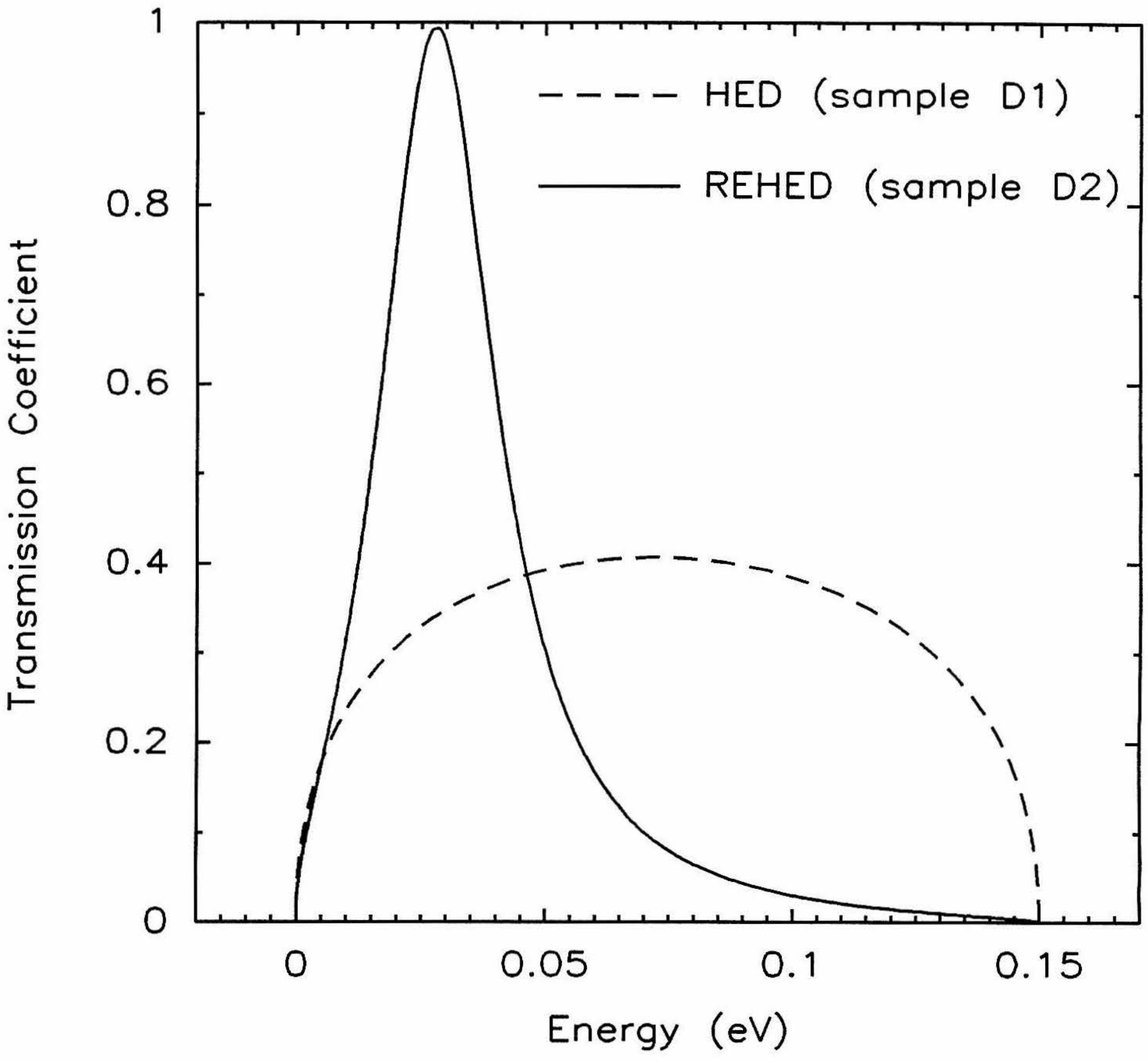

Figure 3.23: Transmission coefficients for samples D1 (dashed) and D2 (solid), calculated at flat band conditions, using a two–band model which incorporates electrons and light holes. The InAs conduction bandedge is taken to be the zero of energy.

and the InAs/GaSb interface. The AlSb barriers were taken to be 24 Å thick. The curves in Fig. 3.24 have similar shapes, with the maximum current density occurring at narrower widths for GaSb quantum wells than for InAs quantum wells, due to the difference in the effective masses of the two materials. For relatively thick GaSb layers ($\approx$ 170 Å), Fig. 3.24(a) shows a current density enhancement due to the appearance of a second QBS. Because of the sensitivity of the calculation to the input parameters (such as band offset values), we have not attempted to compare the calculated current densities to those measured experimentally. However, the calculation does show that there is an optimal position for placement of the AlSb barrier. This position corresponds to a single QBS with an energy in overlap between the InAs conduction band and the GaSb valence band.. (Conceptually, this is identical to the result for BRIT's shown in Figs. 3.12 and 3.13). Fig. 3.24 also explains the different J_p's observed in samples D2 and D3. As Fig. 3.24 shows, the RHED sketched in Fig. 3.20 (b) should have a larger maximum J_p than the RHED shown in Fig. 3.20 (c). This is consistent with the experimental result. In addition, the J_p in RHED's is a strong function of either the InAs or GaSb well width which will also effect the size of J_p in D2 and D3.

3.9 An Experimentalist's 'Theory' of Interband Tunnel Structures

After reading this chapter the wide variety of interband devices should be clear. While the shear mass of data and interpretation may seem overwhelming, interband tunneling is actually rather simple. Much of it can be understood using the concepts of conventional tunnel device theory with a few extensions. Below

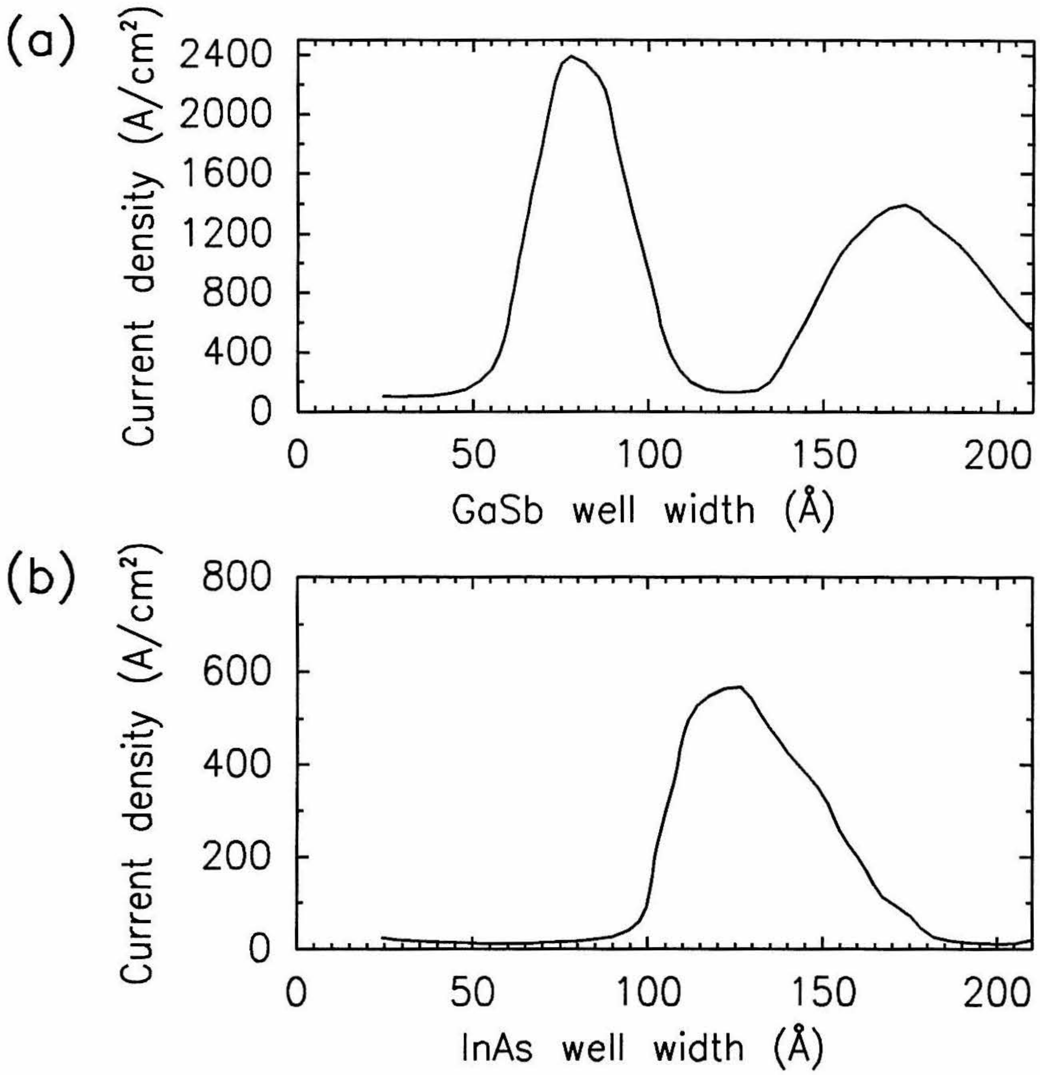

Figure 3.24: Calculated current densities vs. quantum well width for (a) the heterostructure depicted in Fig. 3.20(b), and (b) the heterostructure depicted in Fig. 3.20(c). Both figures show enhanced current densities corresponding to QBS in the region of overlap between the InAs conduction band and the GaSb valence band.

are a few simple rules-of-thumb for analyzing this new class of structures. The following list of concepts is by no means complete. However, applying them to interband devices give a broad, qualitative understanding of these structures.

- When considering interband structures it is helpful to restrict your analysis to one carrier type.
- Carriers can freely move between the conduction and valence bands of adjacent materials as long as there are no energy restrictions.
- The InAs/GaSb interface partially reflects carriers moving between the InAs conduction-band and GaSb valence-band. This is due to the mismatch in wavefunction symmetry between the two bands. Because of this partially reflecting interface, it is possible to form a quasi-bound state without a barrier layer.
- Because there is no classical barrier at the interface, devices with InAs/GaSb tend to have large nonresonant currents associated with them. This leads to small PVR and large current densities.
- The first highly reflecting interface the carriers encounter, whether a classical barrier or an InAs/GaSb interface, tends to determine the device's I-V characteristics.
- Because the mass of the electrode and well layers have different signs, interband devices are ohmic at small bias and have a soft onset of NDR.
- Interband devices without InAs/GaSb interfaces have large PVR's since the well layer acts as a barrier when the device has been biased past resonance.

- The I-V curves of interband devices are rather insensitive to temperature changes since they are on resonance from zero bias until past the current peak where the well suppresses thermionic current.

3.10 Summary

Interband transport structures are a general class of semiconductor heterostructure devices realized in the lattice-matched InAs/GaSb/AlSb material system. These structures involve carrier transport between conduction-band states in InAs and valence-band states in GaSb. The unusual conduction- and valence-band alignments in this material system permit considerable flexibility in the design of heterostructure devices and allow the realization of new device concepts that are not possible in more conventional material systems such as GaAs/Al$_x$Ga$_{1-x}$As. In this chapter we presented an overview of experimental and theoretical studies of transport in two-terminal interband transport structures. A wide variety of interband transport structures exhibiting negative differential resistance were grown, fabricated, and characterized. Various device structures have been found to yield extremely high peak current densities or high peak-to-valley current ratios, making them of considerable interest for high-frequency oscillators or various logic applications. In addition, it was shown that InAs/GaSb is partially reflecting which can lead to quantum confinement and resonant transport without a barrier layer.

References

[1] G.J. Gualtieri, G.P. Schwartz, R.G. Nuzzo, R.J. Malik and J.F. Walker, *J. Appl. Phys.*, **61**, 5337 (1987).

[2] G.J. Gualtieri, G.P. Schwartz, R.G. Nuzzo and W.A. Sunder, *Appl. Phys. Lett.*, **49**, 1037 (1986).

[3] The value of the band offset between InAs and AlSb was derived assuming the transitivity of measured band offsets.

[4] D.H. Chow, R.H. Miles, J.R. Söderström and T.C. McGill, J. Vac. Sci. Technol. B, July/August (1990).

[5] T.M. Rossi, D.A. Collins, D.H. Chow and T.C. McGill, *Appl. Phys. Lett.* **57**, 2675 1990.

[6] K. Taira, I. Hase and H. Kawai, Electronics Letters **25**, 1708 (1989).

[7] D.Z.-Y. Ting, E.T. Yu, D.A. Collins, D.H. Chow and T.C. McGill, *J. Vac. Sci. Technol. B*, July/August 1990.

[8] D.Z.-Y. Ting, E. T. Yu and T. C. McGill, *Phys. Rev. B* **45**, 3583-3592 (1992).

[9] H. Sakaki, L.L. Chang, R. Ludeke, Chin-An Chang, G.A. Sai-Halasz and L. Esaki, *Appl. Phys. Lett.*, **31**, 211 (1977).

[10] E.R. Brown, W.D. Goodhue and T.C.L.G. Sollner, *J. Appl. Phys.*, **64** (3), 1519 (1988).

[11] L.F. Luo, R. Beresford and W. I. Wang, *Appl. Phys. Lett.*, **55**, 2023 (1989).

Chapter 4

Experimental Realization of a Novel Tunneling Transistor

4.1 Introduction

4.1.1 Background

Attempts to fabricate quantum effect transistors have a long history stretching back over 30 years[1]. One motivation is to exploit the inherent speed of quantum phenomena to fabricate extremely fast and dense electronic circuits. A second motivation is to use the rich variety of quantum effect I-V curves (as shown in Chapters 2 and 3) to increase the computational power of the individual elements in an integrated circuit. More concretely, the goal is to provide the circuit designer with a three terminal device in which two of the terminals have an I-V characteristic showing NDR, with the third terminal electrostatically controlling the position or height of the current resonance.

To date, these efforts have failed to produce useful devices; typical current gains are 2-3 due to the large leakage currents in the terminal intended to control the emitter-collector (E-C) current[2, 3, 4]. One attempt to correct this problem was the Stark effect transistor (SET)[5]. It was proposed that an $Al_xGa_{1-x}As/GaAs$ double barrier, tunneling heterostructure with barriers of substantially different widths be grown, and that electrical contact be made to the quantum well and both of the GaAs cladding layers surrounding the double barrier structure. The E-C current would flow from one GaAs cladding layer through the thinner barrier and into the quantum well where it would be extracted. It was reasoned that applying a bias across the thicker barrier would electrostatically modulate the E-C current through Stark shifts of the energy levels in the quantum well. Because of the asymmetry in the thickness of the two $Al_xGa_{1-x}As$ barriers, the base current should be substantially smaller than the modulation of the collector current leading to current gains. Beltram *et al.* [6] subsequently demonstrated the SET concept: large asymmetries in the base and emitter currents and electrostatic modulation of the collector current. However, transistor action was only reported at 7 K which severely limited the device's usefulness. A second problem with the experimentally realized device was that surface Fermi level pinning depleted the exposed GaAs well leading to very large E-C resistances.

4.1.2 Outline of Chapter

This chapter reports a tunnel transistor with measured current gains as high as 100 at room temperature. Section 4.2 explains the device concept and shows how it is a natural outgrowth of the work reported in Chapter 3. The sample growth and device fabrication are detailed in Sections 4.3.1 and 4.3.2, respectively. Experimental results including 2-terminal I-V characteristics (4.4.1), room temperature current gains (4.4.2) and the effect of illumination on the structure

(4.4.3) are given in Section 4.4. Section 4.5 discusses the potential of the device and the chapter is summarized in Section 4.6.

4.2 Device Concept

Figs. 4.1(a) and 4.1(b) are a schematic bandedge diagram of the resonant interband tunneling Stark effect transistor (RITSET) and the geometry of the processed device, respectively. As stated above, the key concept in a SET is the asymmetric barriers. In its original conception this was accomplished by growing $Al_xGa_{1-x}As$ barriers of different widths. In this work we exploit the tremendous flexibility in band alignments offered by the InAs/GaSb/AlSb material system to achieve the barrier asymmetry. Inspection of Fig. 4.1(a) shows that the E-C current flows across the highly conductive InAs/GaSb interface, without tunneling through a classically forbidden region (see reference [7] and Section 3.7). However, current flowing from the base into the collector must tunnel through an AlSb barrier. This leads to large differences between the I-V characteristics of the E-C junction and the collector-base (C-B) junction, which allows a voltage applied between the base and collector to electrostatically control the E-C current without drawing large base currents. It should be noted that even though there is no quantum barrier between the collector and emitter, a quasi-bound state still forms in the InAs collector (as was shown in Section 3.8). The design of the structure builds on the concepts and results of Chapter 3: the E-C current flows through a BRIT like structure (Section 3.5) while the C-B current path is more RIT like (Section 3.3). The combination of these two very different structures is what gives the asymmetry in current conduction that is necessary for realizing the RITSET. The RITSET's bandstructure was suggested by the hybrid interband tunnel device covered in Section 3.6.

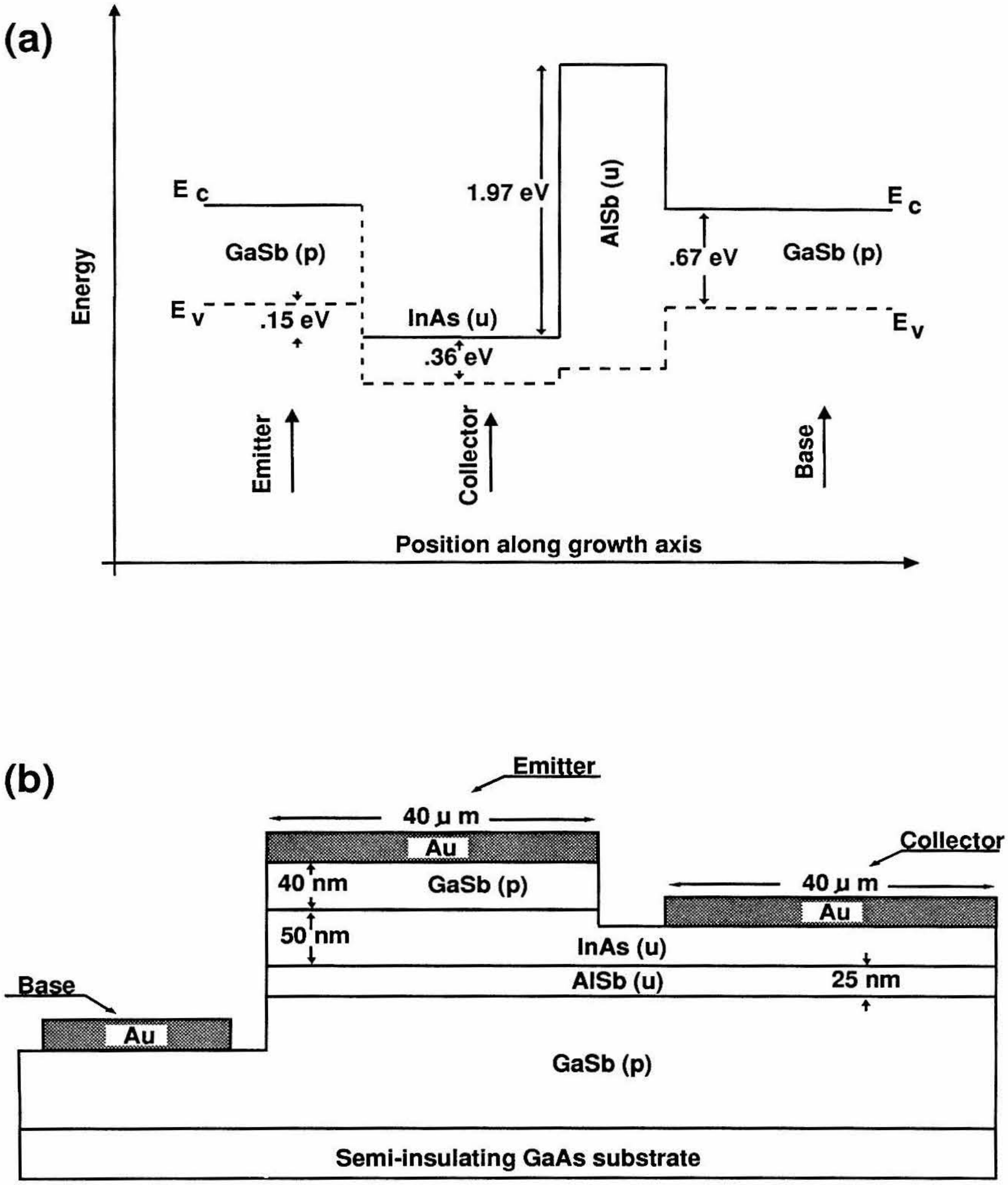

Figure 4.1: a) Schematic bandedge diagram (neglecting band bending) of the RITSET. b) Layout of the device after processing.

InAs was chosen as the well material since the negative Schottky barrier of n-type InAs allows a good ohmic contact to be made to a thin layer[9]. Further, this negative Schottky barrier ensures that surface depletion of the exposed collector well will not hamper device performance as was the case in the earlier attempt to realize a SET structure.[6]

4.3 Experimental

4.3.1 Sample Growth

The samples studied here were grown on semi-insulating GaAs substrates by a molecular beam epitaxy system equipped with cracked Sb and As sources. The growth started with 2000 Å of undoped GaAs followed by a 10 period, 1 monolayer/1 monolayer, GaAs/GaSb superlattice. After the growth of a 0.75 μm buffer layer of GaSb the device structure itself was grown (see Fig. 4.1). The GaSb buffer layer and the active region were grown at a substrate temperature of 490 °C. The superlattice and thick buffer layer are necessary since the lattice constant of the substrate is $\sim 7\%$ smaller than that of the active region of the crystal. This choice of substrates was dictated by the fact that there are no commercially available semi-insulating substrates that lattice match the InAs/AlGaSb material system.

The thick GaSb buffer layer and cap layer were both doped p-type with Si[10] ($p \approx 1 \times 10^{18}$ cm^{-3}). The InAs well and AlSb barrier were not intentionally doped.

4.3.2 Device Fabrication

The fabrication of a working RITSET is rather involved, entailing three separate photoresist (PR) applications and patternings, two metal contact depositions, and three different wet etches. In order to fabricate a working, device it is necessary to etch off the GaSb cap layer without removing the underlying InAs collector layer which is only 250 Å thick. To do this reproducibly an etch that selectively dissolves the antimonide layers but not the arsenide layers was needed. After much trial and error it was found that a basic solution ($NH_3OH : H_2O = 1 : 4$) etches the antimonide layers but not the arsenide layers while an acidic solution ($H_2O : H_2O_2 : H_2SO_4 = 80 : 8 : 1$) had the opposite effect. The development of these etches was crucial to the successful fabrication of the transistor.

The device processing steps are schematically shown in Fig. 4.2. First a chip $\sim$ 5 mm on a side is cleaved from the sample wafer and degreased in acetone, isopropyl alcohol and deionized water. Next PR is spun onto the chip and patterned with ultraviolet light shown through a mask consisting of circles 40 μm in diameter. After developing the PR, circular holes are left in the PR (see Fig. 4.2(a).) Next $\sim$ 2000 Å of Au/Ge is evaporated onto the surface of the chip. This metal layer is much thinner than the PR which is about 1.5 μm thick. As a result, when the chip is placed in acetone in an ultrasonic cleaner to strip off the PR, the Au/Ge on top of the PR is lifted off with it leaving metal circles 40 μm in diameter on the surface of the crystal (see Fig. 4.2 (b).) These metal circles serve as the emitter contact as well as a mask for the first basic etch that exposes the InAs collector well (see Fig. 4.2(c).) That the etch is stopped in the well layer is confirmed by placing two probe wires on the surface of the chip and measuring an I-V curve. If the first basic etch has stopped on the InAs layer, then the I-V curve will be ohmic due to the negative Schottky barrier of InAs. However, if the chip's surface is part of the GaSb emitter layer, then the I-V curve will show the Schottky barrier between the Au probe wire and GaSb. If the etch went past the InAs layer into the AlSb layer, the surface of the crystal turns a milky blue color due to the hydroscopic nature of AlSb. The etch depths were also measured with a stylus profilometer. The vertical resolution of the instrument is 100 Å which is comparable to the thickness of the emitter layer hence its usefulness is limited.

The above process of PR application and patterning, Au/Ge deposition and PR lift off are then repeated. The same mask is used during the exposure to the ultraviolet light, but the mask features are displaced $\sim$ 20 μm from the emitter contact. The result is a collector contact next to the emitter contact (see Fig. 4.2(d).) After this, PR is applied again and a mask which is a negative of the one used to form the contacts is used to pattern the PR. This mask is aligned so that the unexposed PR overlaps with the two metal contacts. This PR protects the current path between the collector well and the collector contact during the device isolation etch. After developing the PR the chip's surface will look like Fig. 4.2(d). At this point the unprotected InAs collector layer is removed with the acidic etch. The removal of the InAs layer is confirmed by watching for the surface to turn a milky blue color, indicating that the AlSb surface layer is reacting with the water in the etch (Fig. 4.2(e).) The individual devices are then isolated from each other by etching through the AlSb barrier and approximately half of the GaSb buffer layer using a second basic etch (see Fig. 4.2(f).) The remaining PR is stripped off of the sample which is then mounted on a header for measurement. Electrical contact to the base electrode is made by applying silver paint directly to the now exposed GaSb buffer layer. The final device geometry is shown in Fig. 4.1 (b).

Following processing the devices were probed with Au wires $\sim 25\,\mu$m in di-

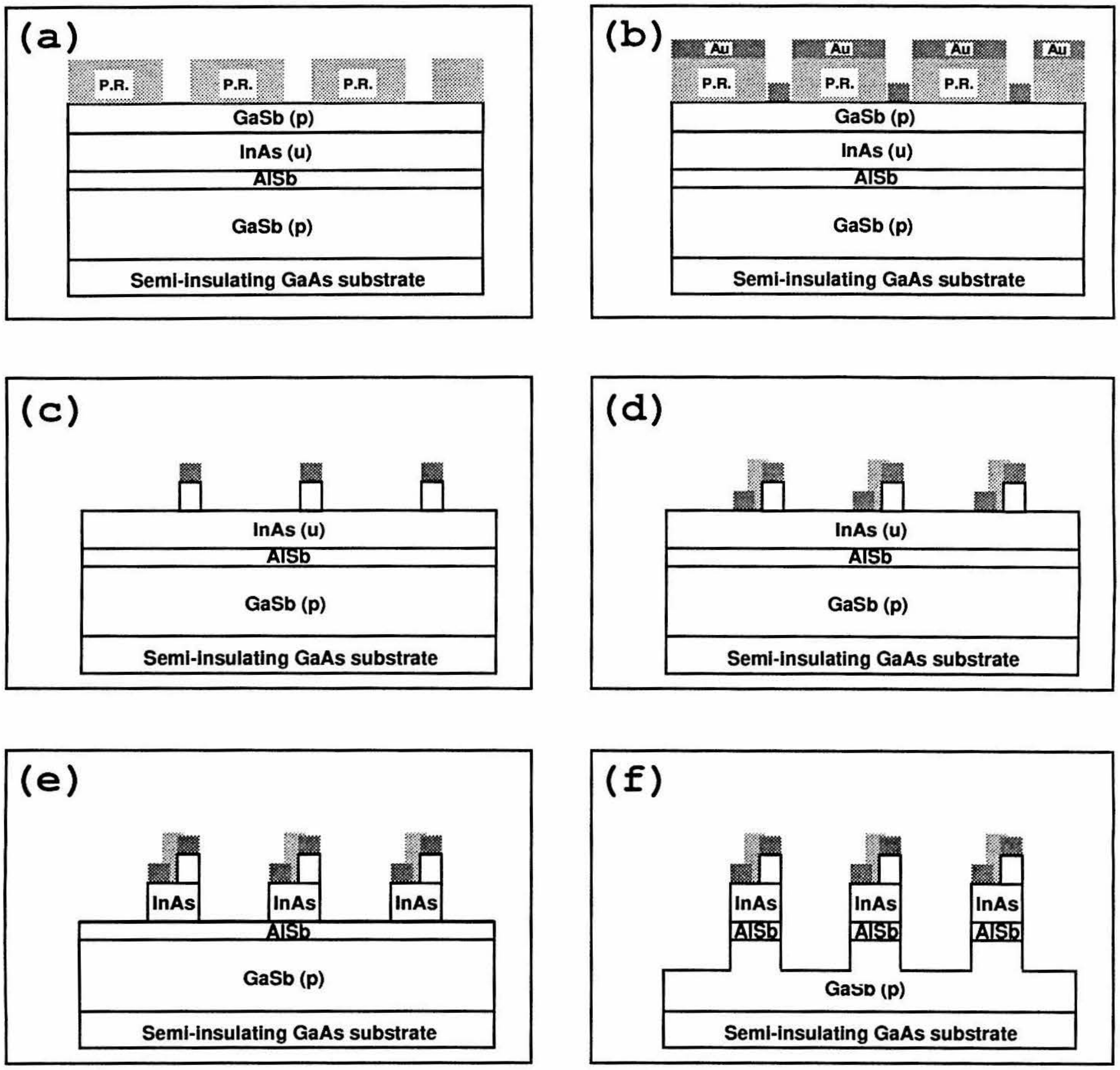

Figure 4.2: A schematic representation of the steps needed to process the transistor.

ameter and I-V curves were taken using an HP 4145A semiconductor parameter analyzer. All electrical measurements were taken with the transistor in the common collector configuration. It should be pointed out that even though the collector contact is at ground, the collector well that is beneath the emitter contact is not at ground. Because there is lateral current flow in the InAs collector well, there must be a voltage drop along it. The potential in the InAs layer is very complicated, involving the E-C current and having emitter and the base biases, the voltage of the collector contact, as well as the pinned surface of the exposed InAs as boundary conditions.

4.4 Electrical Results

4.4.1 Current-Voltage Curves

Fig. 4.3 shows representative I-V curves taken at room temperature for the E-C terminals. E-C curves are shown for base biases ranging from -400 mV to 200 mV in 200 mV steps. All four of the E-C curves pass through the origin showing that the base leakage current is small compared to the emitter current. This suggests that the base bias is rearranging the charge in the collector well rather than simply injecting current into it. The modulation of the E-C current due to the base bias can be thought of in two ways. Either the base bias is changing the band bending in the InAs well which affects the conductivity of the InAs/GaSb interface (Section 3.7), or that the base bias modulates the energy of the quasi-bound state in the InAs collector well through the Stark-effect. The net result of both pictures is the same.

Fig. 4.4 is the C-B I-V curve for the same device. The base biases applied in Fig. 4.3 are in the flat region of the C-B curve where the C-B current is small.

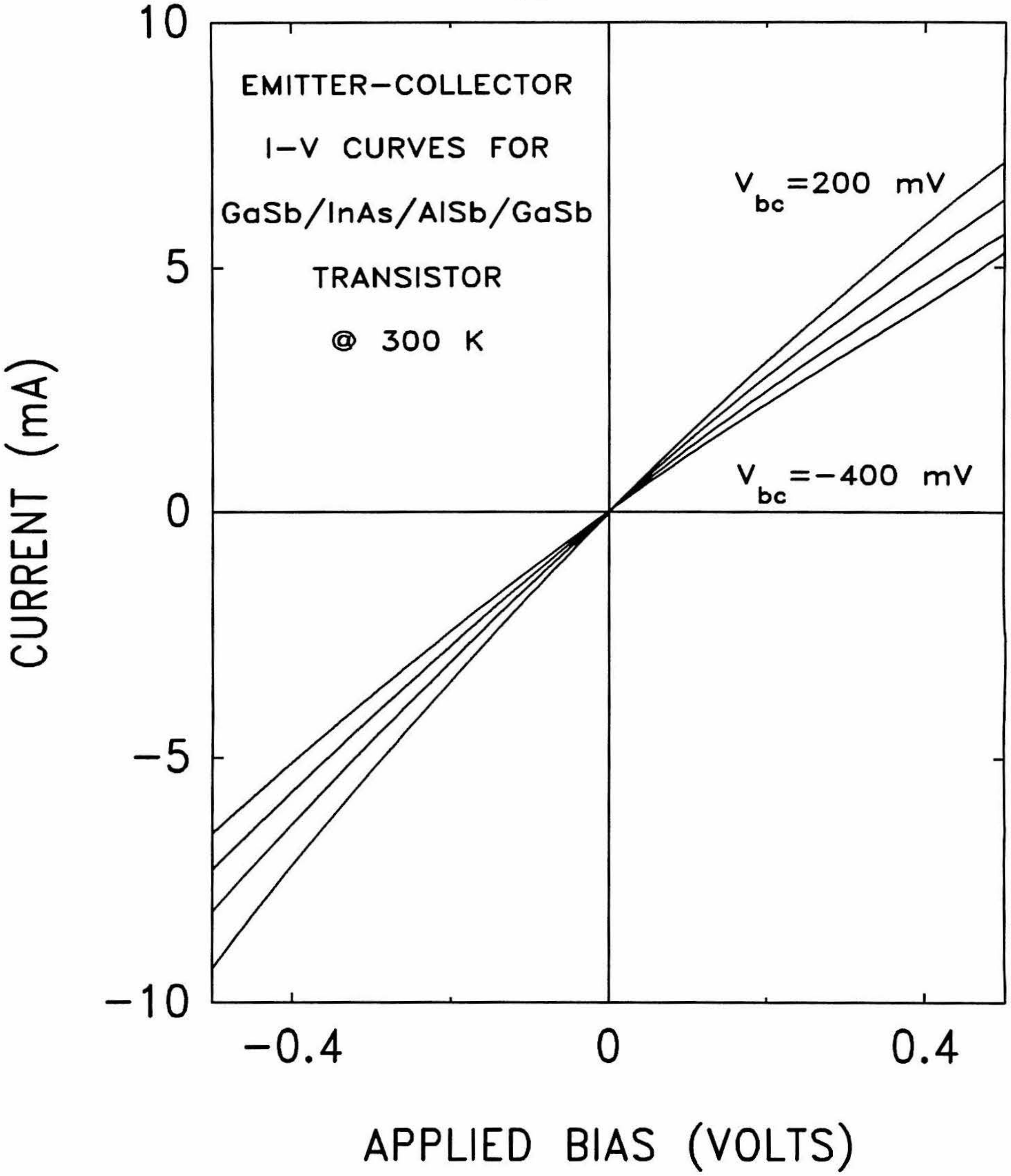

Figure 4.3: Emitter-collector I-V curves taken at room temperature for base biases of 200 mV, 0 mV, -200 mV and -400mV.

Figs. 4.3 and 4.4 show that the E-C and C-B junctions have very different electrical characteristics, as predicted by Fig. 4.1, and that the base is electrostatically controlling the collector current.

4.4.2 Measured Gain Curves

Base currents for voltages in the range from -400 mV to 200 mV are on the order of 10 microamps which is larger than typical gate currents in field effect transistors. As a result, instead of measuring the transconductance of this device, its current gain ($\beta \equiv \partial I_{EC}/\partial I_B$) was measured. β was determined by numerically differentiating plots of I_{EC} vs. I_B. Fig. 4.5 shows β as a function of injected base current for a fixed E-C voltage. The value of V_{EC} chosen for the plot was arbitrary. Different values of V_{EC} shifted the position of the peak in the gain curve and changed its height but did not affect its shape. The region of highest current gain corresponds to base biases in the flat region of Fig. 4.4. In the inset of Fig. 4.5 we show the measured current gain near the maximum. The gain in this region of base current is relatively constant, indicating that this device is potentially useful as a small signal amplifier which requires a reasonably flat gain curve. The range of base biases that correspond to the base currents shown in the inset of Fig. 4.5 is about 300 mV.

Fig. 4.6 plots β as a function of E-C voltage for a fixed base current. β was determined by superimposing a small modulation current onto the injected d.c. base current. The change in I_{EC} as a function of ΔI_B was measured at each value of the E-C voltage shown. The figure shows maximum current gains of over 100. The value of I_B used to collect the data shown in Fig. 4.6 was chosen to maximize the measured current gain. The shape of the gain curve is not sensitive to I_B, but the height and position of the peak gain are weak functions of it. The value

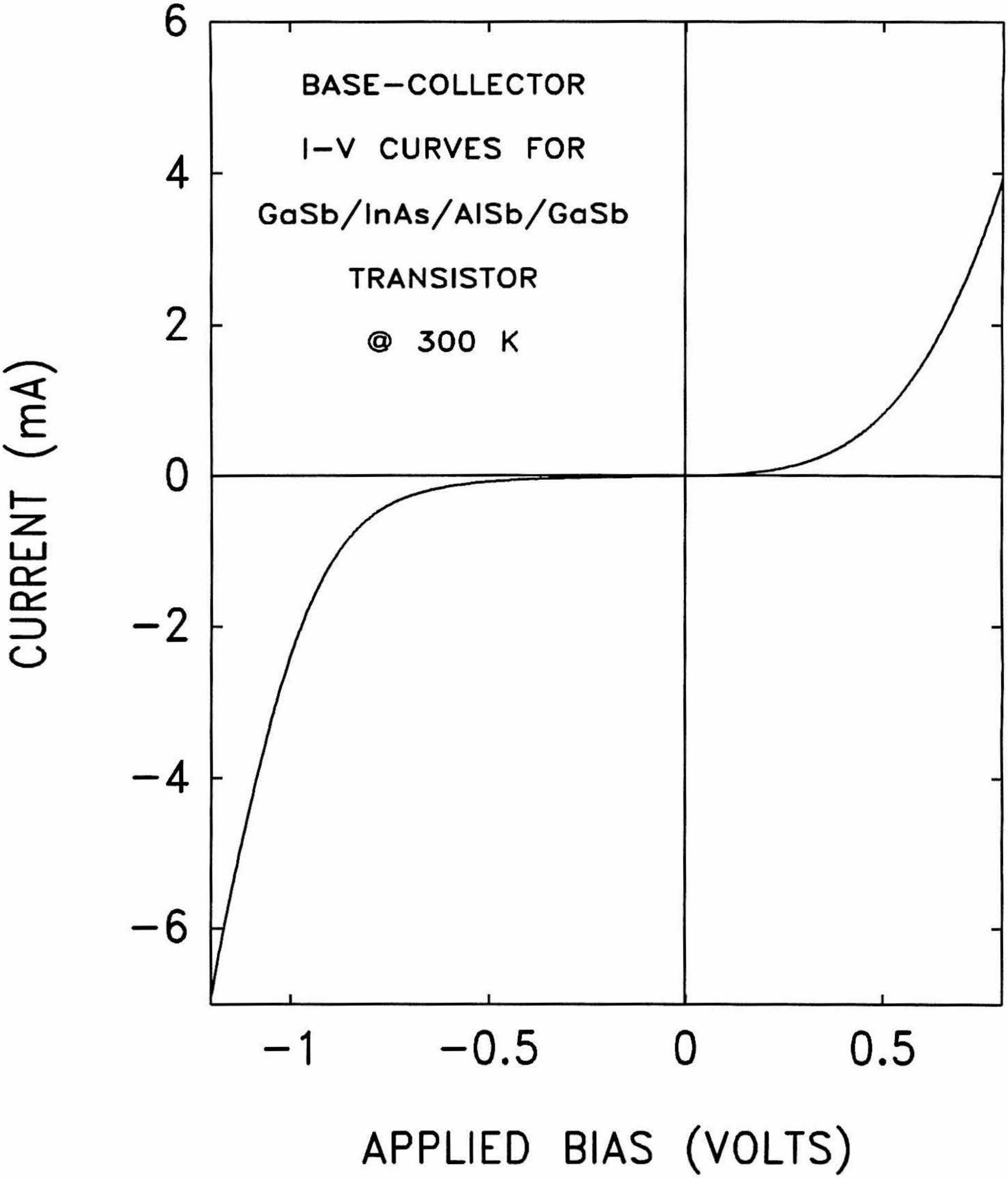

Figure 4.4: Collector-base I-V curve taken at room temperature for the same device shown in figure 4.3.

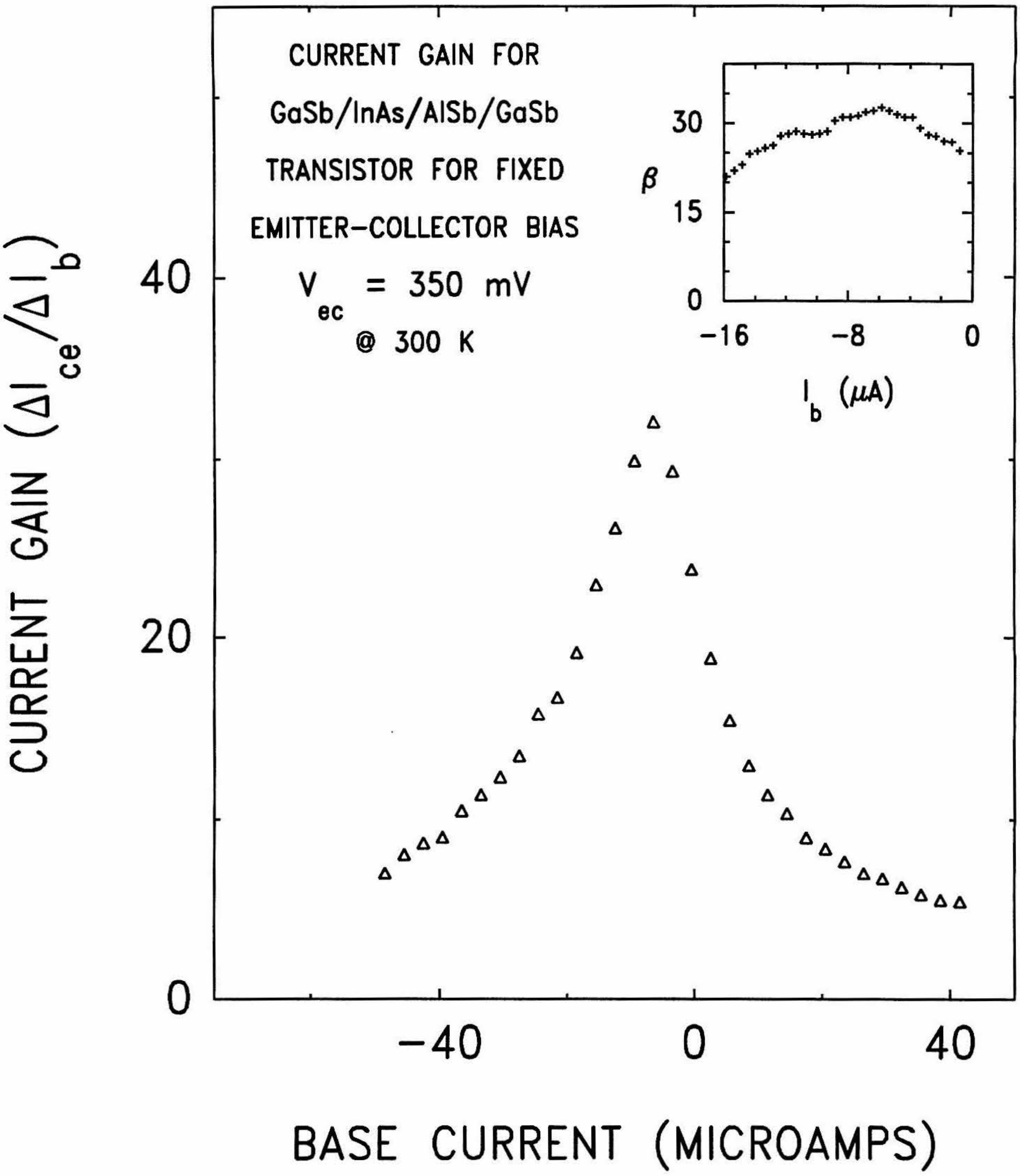

Figure 4.5: Measured current gain as a function of base current for a fixed collector-emitter voltage.

of I_B that maximized the peak current gain varied less than 5% between devices.

4.4.3 Effect of Light on the Device

While making measurements on these devices it was noted that the maximum current gain was cut in half if the sample was illuminated during measurement. In Fig. 4.7 the effect of illumination on the current gain is shown. The probe station used to make the electrical measurements is equipped with a microscope to facilitate making contact to the transistors. The two curves were consecutively measured using the same device. The only difference between them is whether or not the incandescent microscope lamp is turned on. As Fig. 4.7 shows, the lamp decreases the maximum current gain by a factor of two and changes the shape of the gain curve.

In order to understand what causes the change in current gain, two-terminal I-V curves were taken with the sample both illuminated and in the dark. The measurements were taken consecutively using the same device. During all of the two-terminal measurements the potential of the third terminal was allowed to float. Fig. 4.8 shows the change in E-C current with illumination. The change in current divided by the dark current is plotted. The figure shows that the E-C current decreases slightly, but it is unlikely that the $\sim 0.005\%$ change in emitter current could account for the dramatic change in the current gain plotted in Fig. 4.7. Fig. 4.8 indicates that the optical radiation is not greatly affecting the E-C current path.

In Fig. 4.9 the percent change in the C-B current is plotted. At small biases the C-B current increases as much as 45% which is more than enough to account for change in current gain. As the C-B bias is increased, the effect of the illumination decreases but the C-B current is still $\sim 20\%$ larger at $\pm$ 400 mV

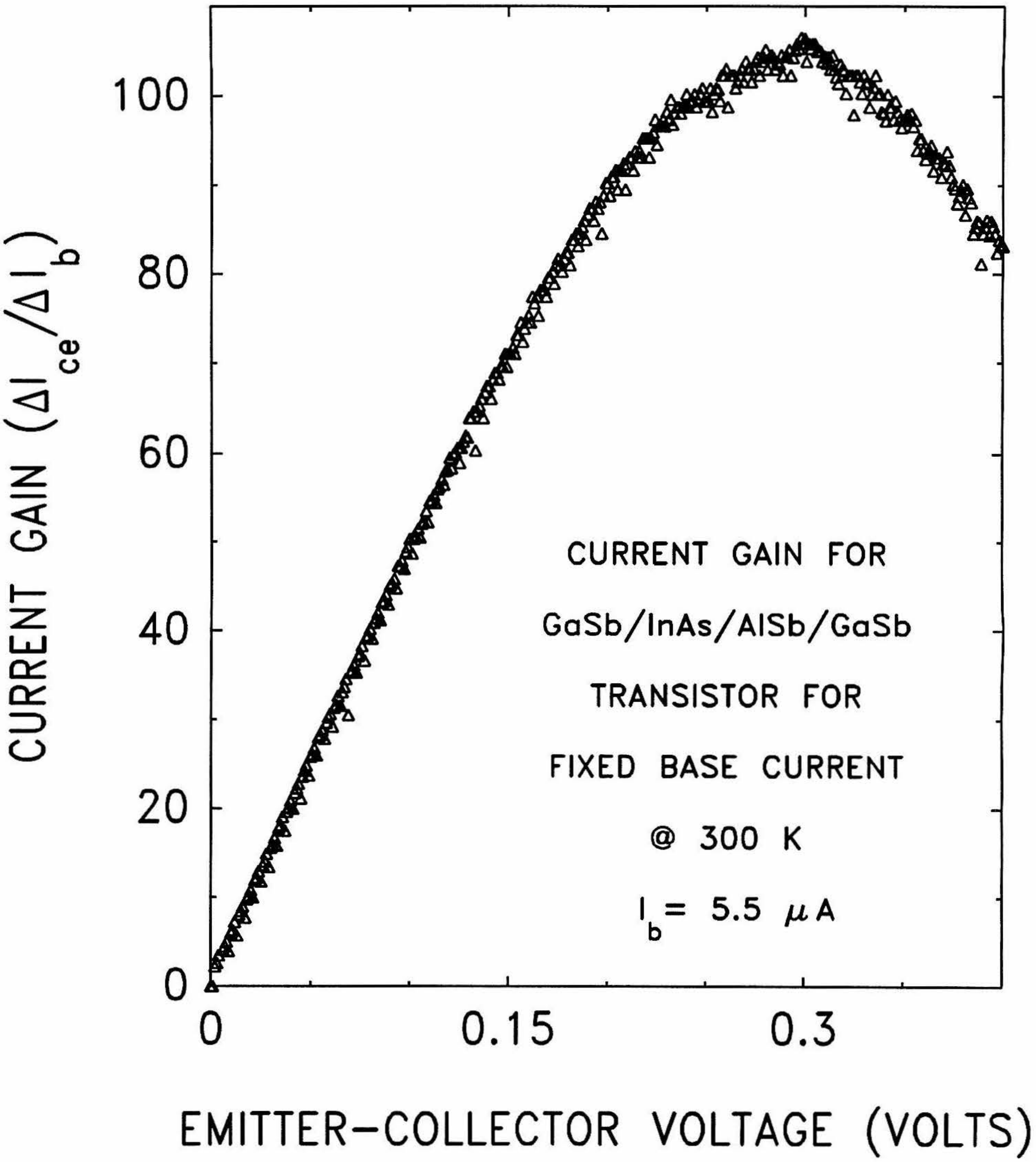

Figure 4.6: Measured current gain as a function collector-emitter bias for a fixed base current.

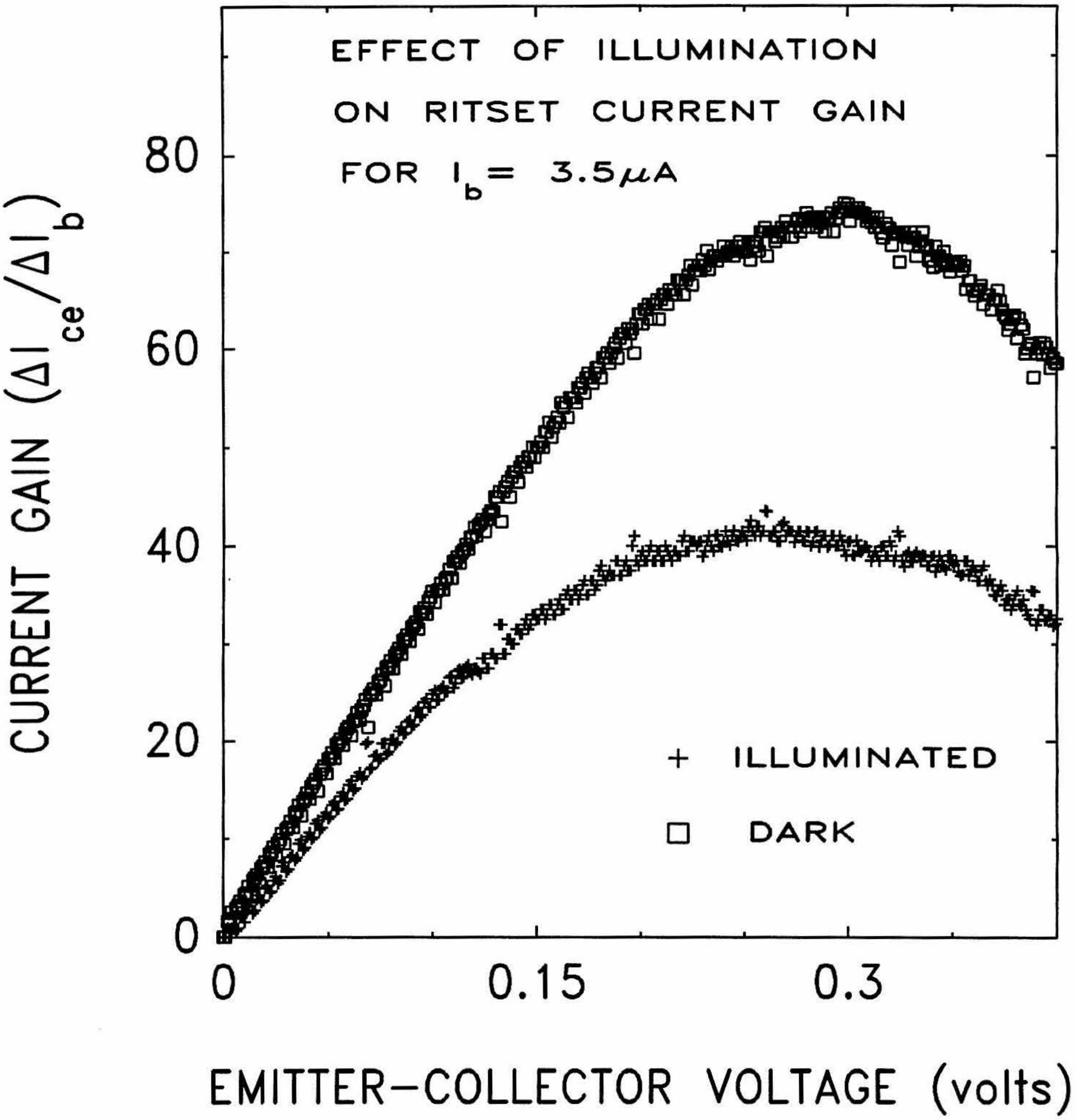

Figure 4.7: Effect of illumination on the transistor's current gain.

than when the sample is dark. Figs. 4.7, 4.8 and 4.9 are representative of all the devices measured. The size of the effect increased monotonically with the optical power incident on the sample.

Taken together, Figs. 4.8 and 4.9 indicate that the decrease in current gain when the transistor is illuminated is due to a 'leakier' C-B current path. It isn't surprising that light should effect the structure since the majority of the active region consists of direct, small bandgap materials: InAs and GaSb. Because all of the GaSb cap layer which is left in the processed device is covered by $\sim 2000\,\text{Å}$ of Au/Ge (see Fig. 4.1(b)), it is unlikely that much of the incident light reaches the GaSb emitter layer. As a result, the effect is probably due to electron-hole production in the InAs collector well between the emitter and collector contacts. Since the bandgap of InAs is small (450 meV) compared to the energy of visible light, very little of the light incident on the InAs layer should reach the underlying AlSb or GaSb layers. Therefore, the incident light must be affecting the InAs collector layer. Examination of Fig. 4.1(a) makes it clear that electron-hole pairs created in the InAs collector will increase the C-B current. Neglecting band bending, there are no barriers for holes in the InAs collector from diffusing into the valence bands of either the AlSb barrier layer or the GaSb emitter layer, irrespective of the sign of the C-B bias. For electrons the situation is slightly more complicated. If the base is negative with respect to the collector, there is no barrier keeping the excess electrons in the collector from flowing into the valence band of the GaSb emitter layer. However, if the base is positive with respect to the collector, the AlSb barrier will keep the electrons in the InAs layer so they will not contribute to the C-B current. This difference in the barriers that holes and electrons see when they are in the InAs collector well explains the asymmetry shown in Figs. 4.8 and 4.9.

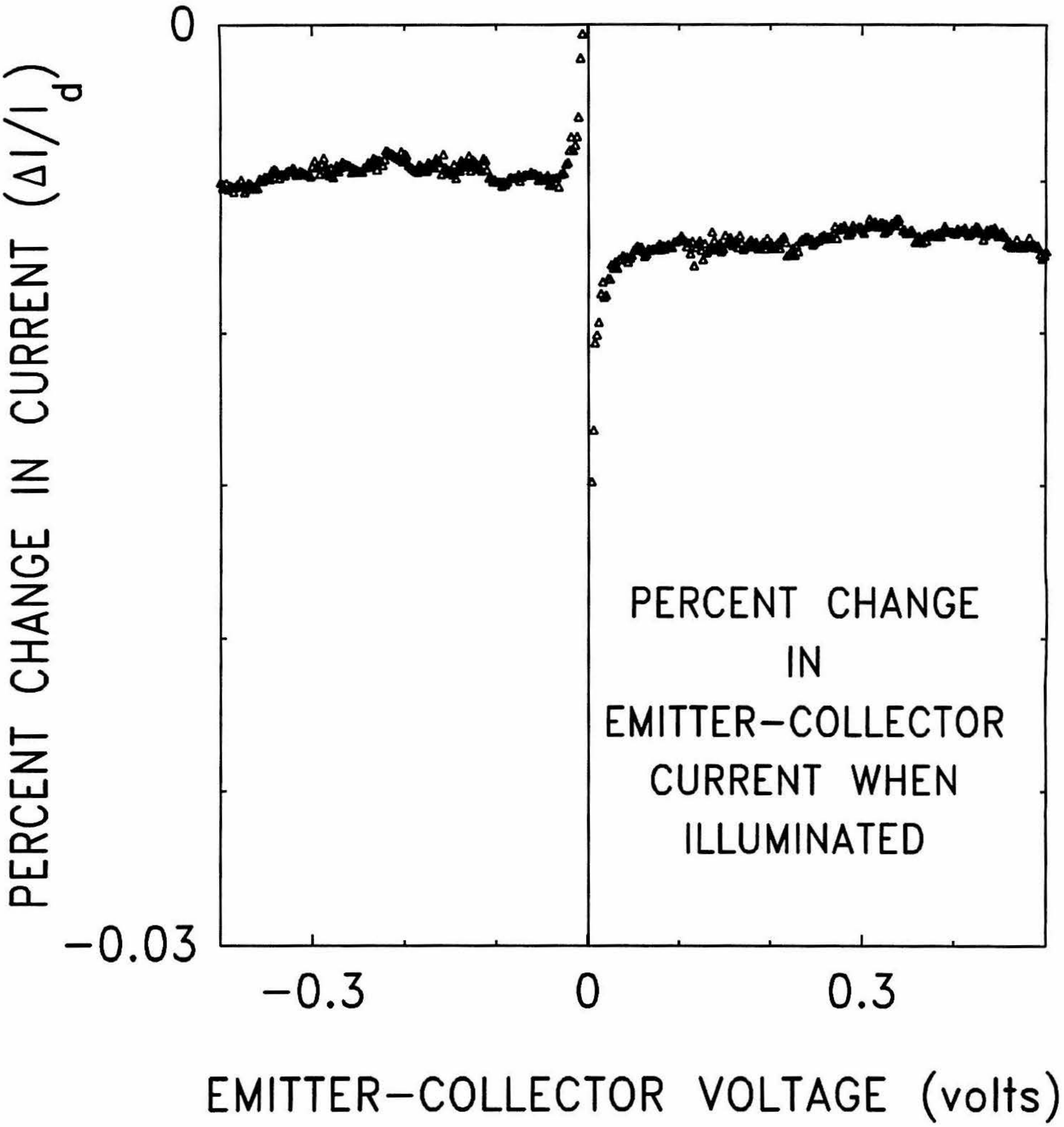

Figure 4.8: Effect of illumination on the emitter-collector current.

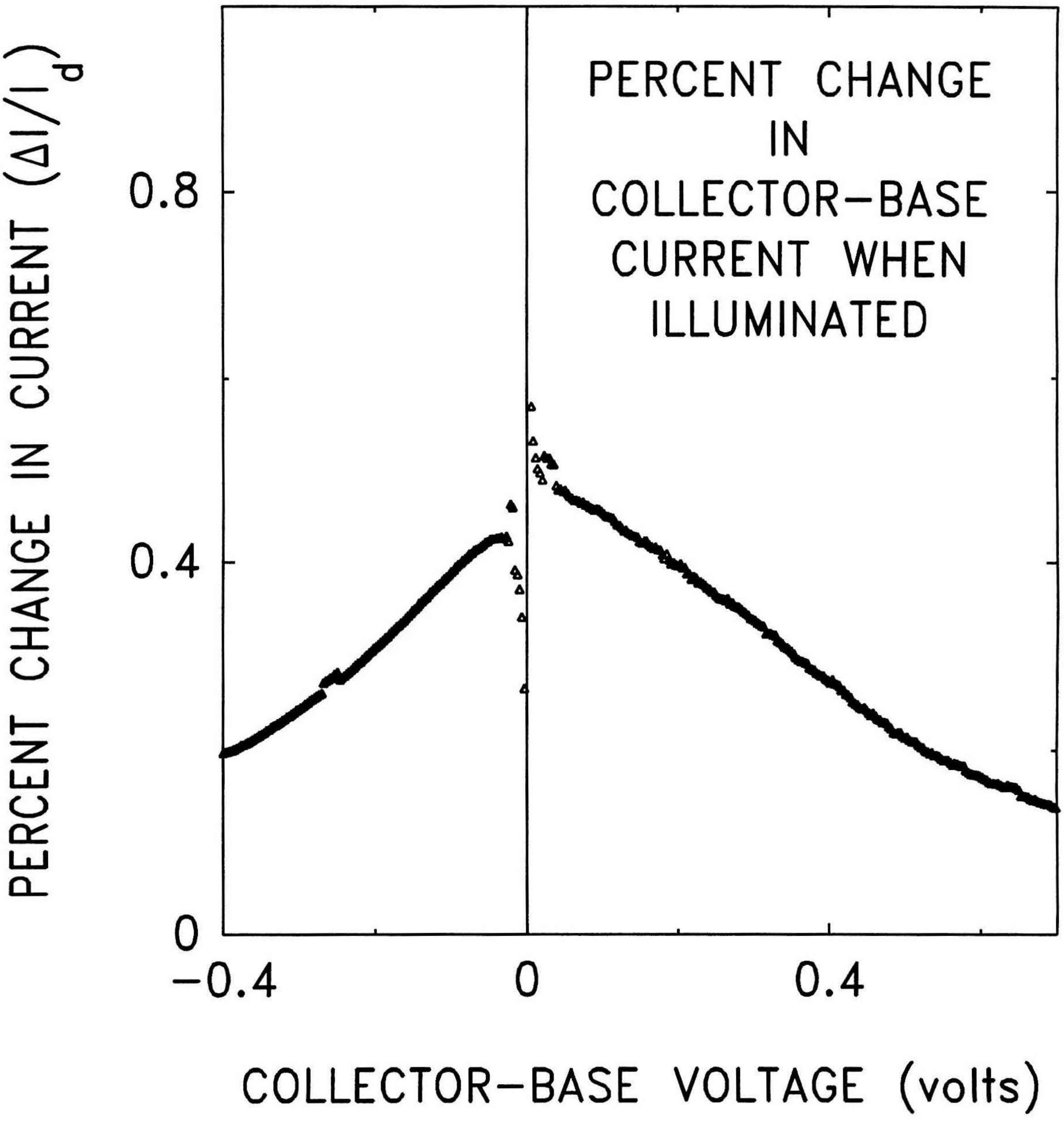

Figure 4.9: Effect of illumination on the collector-base current.

4.5 Discussion of Device Potential

It is difficult to predict the potential performance of any discrete device when it is placed in a circuit. In general, the actual speed of any integrated circuit is limited by parasitic R-C time constants which are highly dependent on the cleverness of the design engineers. Still, the RITSET holds promise for fabricating high speed switches and high frequency amplifiers. Because electrons can easily move across the InAs/GaSb interface[7], the E-C current should be able to respond very quickly to changing electrical fields. Furthermore, the small base currents should minimize delays due to tunneling across the AlSb barrier. Moreover, in a well designed RITSET the base bias modulates the E-C current by rearranging the charge in the InAs collector well rather than by charging the collector via the base electrode. In any case, the base current can be greatly reduced by simply growing a thicker AlSb barrier between the base and collector. (However, the AlSb barrier can not be made arbitrarily thick because the ~ 0.5 % lattice mismatch between GaSb and AlSb will eventually nucleate dislocations in the barrier layer which would presumably hamper device performance.)

The RITSET's speed will also be limited by the intrinsic response time of the materials and its interface capacitances as well as the lifetime of the quasi-bound state in the InAs collector well. The latter is extremely short and should not be a significant factor.[8] The zero-bias, junction capacitances are determined by the amount of charge that must be transferred across the InAs/GaSb interface because of the difference in energy between the bulk Fermi levels of GaSb and InAs.[11] By carefully controlling the doping of the layers in order to minimize this charge transfer, the junction capacitance can, in principle, be made extremely small.

Another possible limiting factor of the SET's speed is the large mass of GaSb heavy holes. Because the base current is small, the current density in the thick GaSb buffer layer is very small and should not be a major limitation of device performance. The current densities in the GaSb emitter layer are much larger and could be a problem. However, for basic symmetry reasons electrons at the InAs/GaSb interface will couple most strongly to the light hole band of GaSb.[12] If the GaSb cap layer is sufficiently thin, the electrons could potentially travel between the collector and the emitter contact through light hole states without scattering into the heavy hole states. Since the mass of light holes in GaSb is smaller than the mass of electrons in GaAs, the conduction of charge through the GaSb cap layer should not be a major limitation if it transverses the layer via light hole states. This is not an unreasonable possibility. Because of the large GaSb heavy hole density of states, the Thomas-Fermi screening length of GaSb doped at p= 5×10^{18} cm^{-3} is about 20 Å. Hence, cap layers as thin 50 to 100 Å should be sufficiently thick so that Fermi level pinning at the emitter contact does not effect the E-C junction.

4.6 Chapter Summary

In summary we have measured current gains as high as 100 at room temperature in a novel transistor. The device was grown in the InAs/GaSb/AlSb material system which offers three distinct types of band alignments. Because of this flexibility, the collector and base terminals are separated by a classically forbidden region while the emitter and collector terminals are not. This asymmetry in current transport between the terminals of the device allows base biases to modulate the emitter-collector current without injecting large base currents. Because current conduction in this unique structure is due to resonant transmission, it is potentially useful in the fabrication of high speed switches and high frequency oscillators.

References

[1] C.A. Mead, *Proc. IRE*, **48**, 359 (1960).

[2] A.C. Seabaugh, Y.-C. Kao, J. Randall, W. Frensley and A. Khatibzadeh, *Proceedings of the 22nd International Conference on Solid State Devices and Materials*, Sendai, Japan (Komiyama Printing, Tokyo) 15 (1990).

[3] M. Heiblum and M.V. Fischetti, *IBM J. Res. Devel.* **34**, 530 (1990).

[4] S. Yamaura, Y. Miyamoto and K. Furuya, *Proceedings of the 22nd International Conference on Solid State Devices and Materials*, Sendai, Japan (Komiyama Printing, Tokyo) 23 (1990).

[5] A.R. Bonnefoi, D.H. Chow and T.C. McGill, *Appl. Phys. Lett.* **47**, 888 (1985).

[6] Fabio Beltram, Federico Capasso, Serge Luryi, Sung-Nee G. Chu, Alfred Y. Cho and Deborah L. Sivco, *Appl. Phys. Lett.*, **53**, 219 (1988).

[7] D.A. Collins, E.T. Yu, Y. Rajakarunanayake, J.R. Söderström, D.Z.-Y. Ting, D.H. Chow and T.C. McGill, *Appl. Phys. Lett.*, **57**, 683, (1990).

[8] D.Z.-Y. Ting, D.A. Collins, E.T. Yu, D.H. Chow and T.C. McGill, *Appl. Phys. Lett.*, **57**, 1257 (1990).

[9] H.H. Wieder, *Appl. Phys. Lett.*, **38**, 170 (1981).

[10] T.M. Rossi, D.A. Collins, D.H. Chow and T.C. McGill, *Appl. Phys. Lett.*, **57**, 2256 (1990).

[11] LL. Chang and L. Esaki, *Surf. Sci.* **98**, 71 (1980).

[12] G. Bastard, *Phys. Rev. B.*, **25**, 7584 (1982).

Chapter 5

Time Resolved RHEED Studies of Superlattice Growth

5.1 Introduction and Outline

The structures which motivated this chapter are close cousins to the devices covered in Chapter 3: InAs/$Ga_{1-x}In_xSb$ strained layer superlattices (SLS.) These superlattices were proposed and demonstrated as candidates as far infrared detectors(8 - 20 μm)[1, 2, 3, 1]. While the basic detection mechanism has been demonstrated, the material quality of these SLS's must be improved before they can be employed in applications. In the course of studying the properties of these detectors it was found that the way in which their internal interfaces are formed has a dramatic impact on performance. We have observed that the background carrier type changes between structures whose only difference is the manner in which their internal interfaces are formed. The magnitude of the optical absorption is also seen to vary by over a factor two depending on how the structure is grown. In addition, the bandgap of nominally identical SLS's can vary by as much as 40 meV which is a large fraction of the bandgap of devices with intended cutoff wavelengths beyond 10 μm.

The importance of understanding and controlling the formation of mixed anion heterointerfaces is not limited to this device, however. In addition to InAs/$Ga_{1-x}In_xSb$ SLS's, as evidenced by Chapter 3, there is a rich variety of tunnel structures realizable in the mixed anion, InAs/AlGaSb material system. There are also a number of interesting, related structures incorporating arsenide/antimonide (As/Sb) heterointerfaces. Among them are InAs/AlSb RTD's with oscillation frequencies in excess of 750 GHz[5], GaInAsSb/AlGaAsSb lasers with wavelengths suitable for optical fiber applications[6], promising AlSb/InAs transistor technologies [7, 2, 9, 10] and far infrared InAs/InAsSb [11] detectors. These efforts have resulted in a large number of promising devices. In order for this broad class of structures to reach their full potential, a basic materials issue must be understood: how to control the structural and chemical properties of the As/Sb interface.[2]

Because the vapor pressures of the group V's (As and Sb) are substantially larger than those of the relevant group III's (In, Ga and Al), their sticking coefficients are very different at typical substrate temperatures. As a result, it is necessary to evaporate 4 to 10 group V atoms for each group III atom in order to grow a stoichiometric crystal. In structures involving a common anion – such as AlAs/GaAs heterostructures – this is not an issue. However, in As/Sb heterostructures the question of what to do with the excess anions is very important. There are two distinct problems. The first is controlling cross contamination of the group V's: As incorporation in the GaSb layers when growing an InAs/GaSb superlattice for instance. The second is the composition of the interface. For example, when switching between InAs and GaSb layers, one could imagine preparing an interface that consisted of InAs/In/Sb/GaSb or one with InAs/As/Ga/GaSb or some intermediate composition (see Fig. 5.1). There is no *a priori* reason to believe that these different kinds of interfaces would lead to similar electrical and optical properties. In fact, as mentioned above, the type of internal interfaces does effect the characteristics of InAs/GaInSb SLS's. In the InAs/AlSb material system, the interface composition affects the carrier mobility, carrier concentration, and the InAs/AlSb valence band offset [2, 3].

Section 5.2 explains how these InAs/$Ga_{1-x}In_xSb$ SLS's works and shows their sensitivity to how their internal interfaces are formed. The experimental setup is described in Section 5.3. The results of the experiments are presented and discussed in Sections 5.4 and 5.5 and the chapter is summarized in Section 5.6.

5.2 InAs/$Ga_{1-x}In_xSb$ Infrared Detectors

5.2.1 Theory of Operation

Fig. 5.2 sketches how these SLS's work. The upper part of the figure shows the device's bandedge diagram, with the resulting probability density distribution shown below. The structure consists of thin alternating layer of InAs and $Ga_{1-x}In_xSb$. The layers are 15 to 50 Å thick, with values of x between 0.10 and 0.40. The structures are strained to thick GaSb buffer layers, grown on GaAs substrates. The relative sizes of the lattice constants, A_x, are:

$$A_{InAs} < A_{GaSb} < A_{GaInSb}$$

with A_{GaInSb} increasing for larger In mole fractions. As a result, the layers of the superlattice are under alternating compressive (GaInAs) and tensile (InAs), biaxial strain. Quasi–bound states form in the valence-band of the GaInSb layers and in the conduction-band of the InAs layers. Since the SLS layers are thin, the states in the individual layers interact and form bands.

Two types of interfaces possible between two compound semiconductors

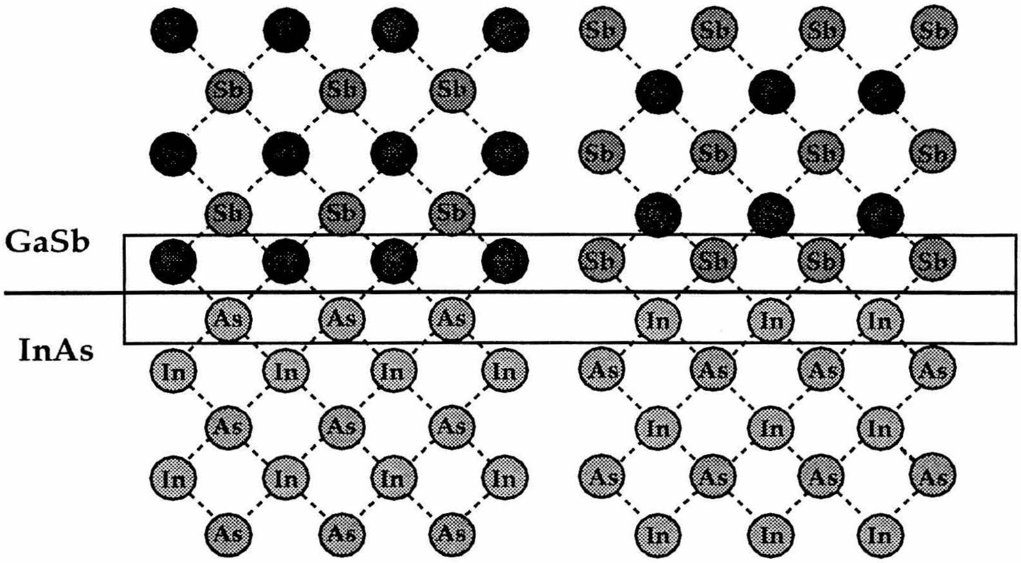

GaAs-like interface	**InSb-like interface**
~ 7 % compressive strain at interface	**~ 7 % tensile strain at interface**
n-type background in IR superlattice	**p-type background in IR superlattice**

- **Factor of two change in absorption for different interface schemes.**
- **Up to 50 meV change in bandgap for different interface schemes.**

Figure 5.1: The two types of interfaces that can be formed from two different compound semiconductors.

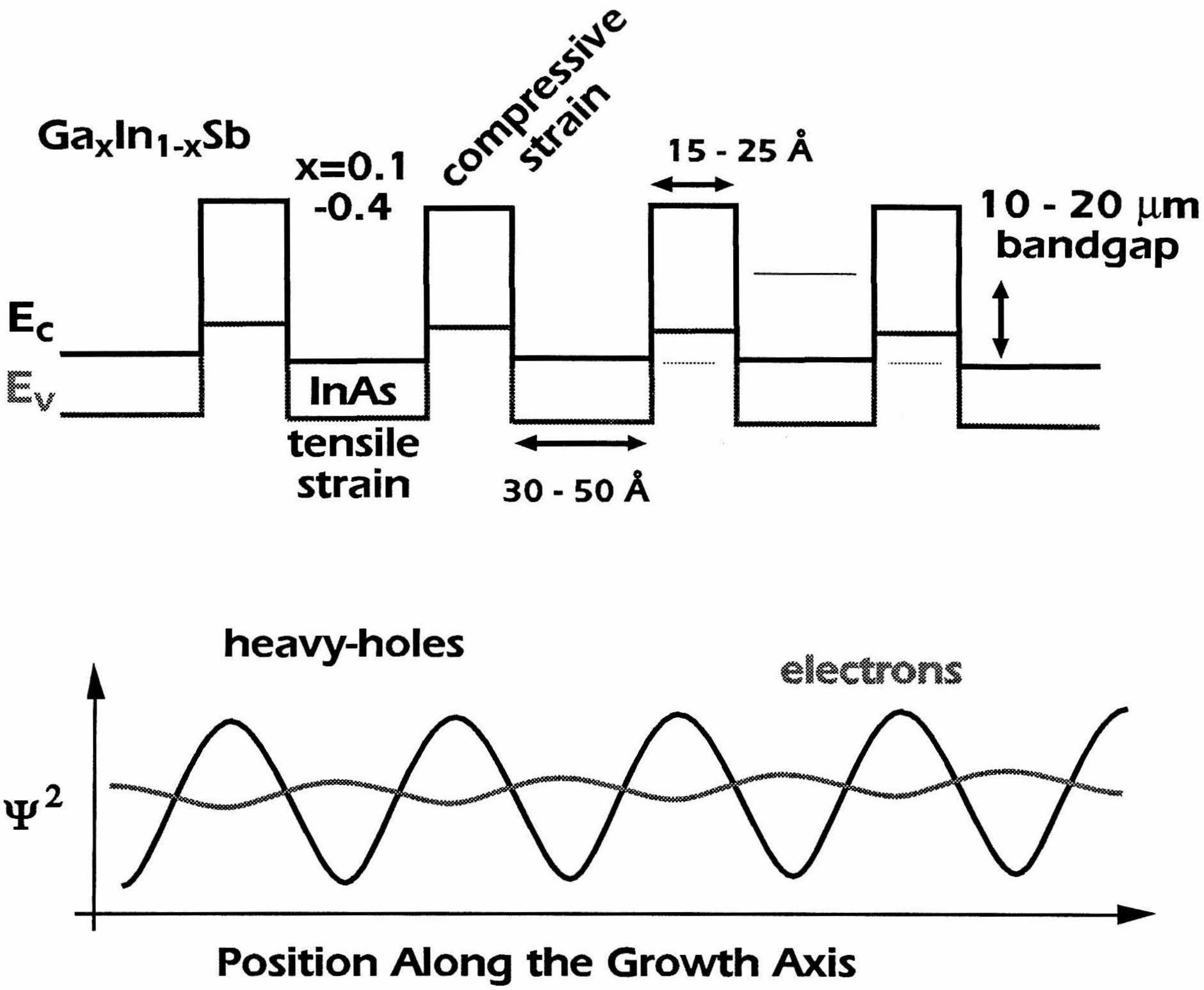

Figure 5.2: Bandedge diagram and carrier probability density for InAs/GaInSb superlattices. In the bandedge diagram, the conduction-band minimum is shown with a solid line, and the valence-band maximum is shown with the grey line.

The SLS bandgap can be altered by two means. Adjusting the superlattice period changes the quantum confinement and hence the absorption edge. Increasing the In content in the Sb layer narrows the SLS bandgap. The lattice constant of GaSb is about 0.5% bigger than that of InAs. InSb is roughly 7.0% larger than InAs. As a result, increasing the In mole fraction increases the compressive strain in the GaInSb layer which raises the heavy-hole bandedge, reducing the SLS bandgap. Because there are two independent means of adjusting the bandgap, a range of SLS periods and In mole fractions will give a desired detector cutoff wavelength. In general, the shortest period SLS will give the highest absorption since the carriers are less well localized in the individual superlattice layers. However, the In content in the GaInSb layer can not be made arbitrarily high due to the large strains in the structure. The largest X_{In} typically employed is 0.40.

5.2.2 Effect of the Internal Interfaces of Device Characteristics

As mentioned in the introduction, there are two ways to form an interface between different compound semiconductors. Fig. 5.1 sketches them for the care of an InAs/GaSb interface. In the left hand figure, there are a row of Ga–As bonds. These types of interfaces will be called 'GaAs–like' or 'GaInAs–like' in the case of an InAs/GaInSb superlattice. In the right hand figure the crystal is shown with a row of In–Sb bonds. These are termed 'InSb–like' interfaces. In an actual crystal, the interfaces will likely be an intermediate composition. As will be detailed later the MBE grower can force the crystal towards either of the two extremes by the oven shuttering sequence at the interface. In Section 5.2.1 the crucial role of strain in these structures was covered. Comparing the lattice constants of GaAs and InSb to that of GaSb explains why the interface has such a dramatic effect on device operation: the lattice constant of GaAs is about 7% smaller while that of InSb is roughly 7% larger than GaSb.

Fig. 5.3 shows the effect of the interface on the InAs/GaInSb SLS's bandgap. Hall data is shown for two SLS's which have the same period and GaInSb composition. The only difference between the two samples is the manner in which the interfaces are formed. The data were taken for temperatures where the SLS's have intrinsic carrier concentrations. The superlattice bandgap is determined by fitting the data to

$$n = Ae^{-E_g/2k_bT}$$

where A is a constant, T is the temperature, k_b is the Boltzman constant and E_g is the bandgap. The bandgaps of these nominally identical SLS's differ by almost 15% due to the different interfaces with the sample with GaInAs-like interfaces having the larger bandgap. This means that for a given desired cutoff wavelength, a GaInAs-like SLS will have a larger period. This indicates that for a given SLS bandgap, samples with InSb-like interfaces will have higher absorptions. The SLS's whose data is shown in Fig. 5.3 were grown in a Varian Gen two. However, similar samples were grown in two separate Perkin-Elmer 430 MBE chambers by three different growers. In samples grown in these two chambers, it was observed that the type of intrinsic background carrier changes when comparing SLS's grown with the two different types of interfaces.

Fig. 5.4 shows x-ray rocking curves taken from two nominally identical superlattice which differ only in how their interfaces are formed. The data were taken in the (004) direction. In the data, the signal from the GaAs substrate and the relaxed GaSb buffer layer are apparent, as well as the superlattice fringes. The data for the GaInAs-like sample is much broader since it has roughly half

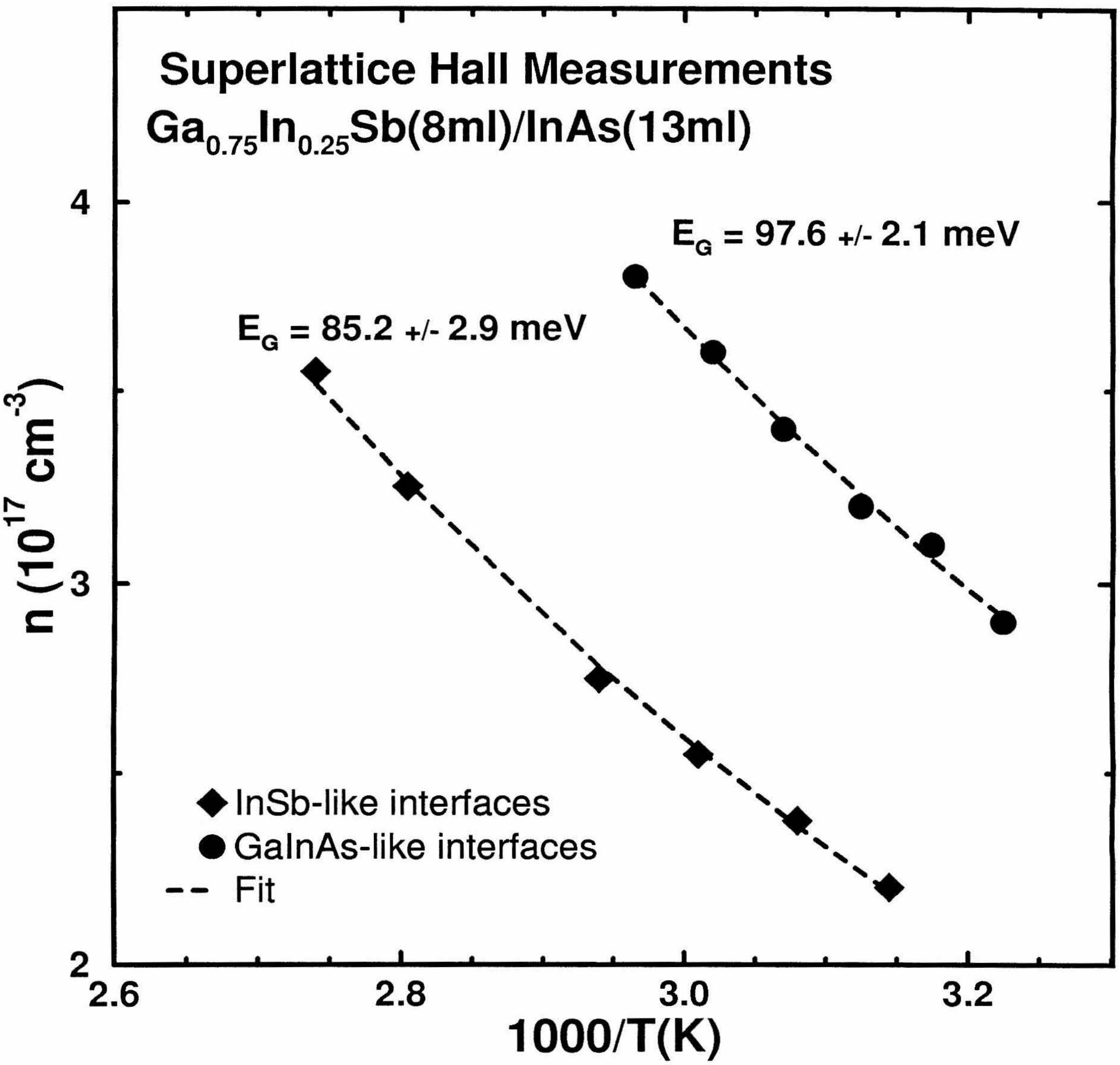

Figure 5.3: Hall measurements of the bandgaps of two superlattices. The structures are nominally identical except for the manner in which the internal interfaces are formed.

as many superlattice periods as the InSb-like SLS. Comparing the period of the superlattice fringes shows that the two SLS's have the same period, and the composition of the GaInSb layers in the two structures was held constant. However, the positions of the zeroth order superlattice peaks do not match. The position of this peak is related to the average atomic spacing in the growth direction. Data taken in the (115) and ($\overline{1}\overline{1}5$) directions confirms that both structures are coherently strained to the GaSb buffer. Therefore, the difference in the two structures must be due to the type of interface employed. The change in the internal strain is what causes the shift in superlattice bandgap between structures with identical periods and layer composition. Photocurrent measurements confirm that the bandgap of the GaInAs-like SLS is almost 20 meV larger than that of the InSb-like sample.

5.3 Experiment

5.3.1 Reflection High Energy Electron Diffraction (RHEED)

Reflection high energy electron diffraction (RHEED) is a standard sample characterization technique used during MBE growth. In RHEED, electrons are diffracted off the sample's surface at glazing angles and onto a phosphor screen. Because the electrons are typically 1 ° to 3 ° from the surface parallel, the electron gun and phosphor screen do not interfere with the MBE beam fluxes which are nearly normal to the wafer's surface. As a result, at RHEED geometries it is possible to monitor the surface's diffraction pattern during growth (see Fig. 1.1). Because of the glancing angle geometry, the electrons penetrate ~ 5 Å into the crystal hence RHEED is only sensitive to the first few atomic layers of the crystal.

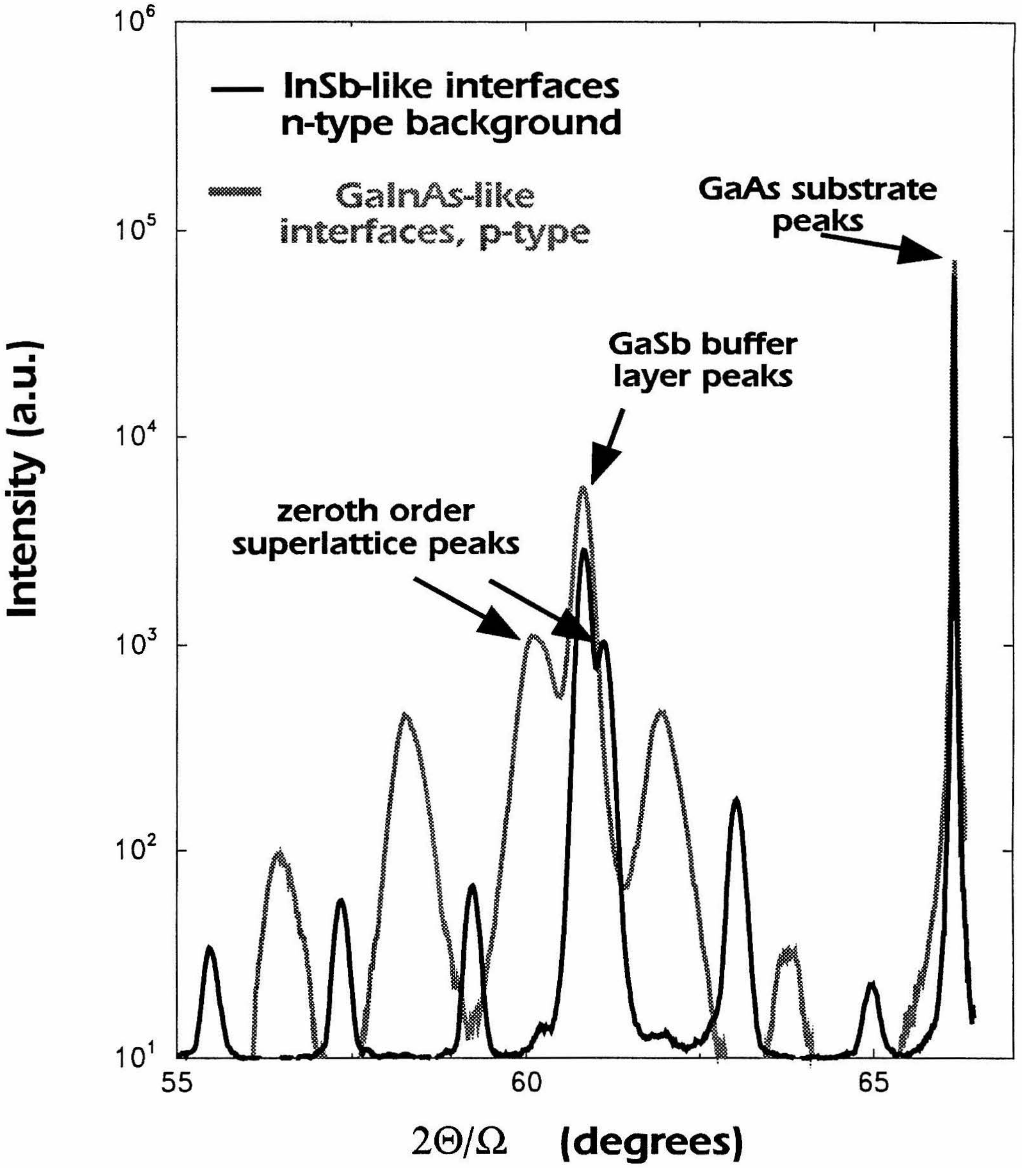

Figure 5.4: X-ray rocking curves of GaInSb/InAs superlattices with different types of interfaces. The structures are nominally identical except for the manner in which the internal interfaces are formed. The different positions of the zeroth order superlattice peaks shows that the atomic spacing and, hence, strain differs in the two structures.

Typical RHEED energies and currents are 10 keV and 0.5 mA, respectively. A word about the relevant length scales is also helpful. The electron spot size is on the order of 1 mm in diameter. Therefore, because of the glancing angle of incidence, the RHEED footprint on the sample is roughly 1 mm by 40 mm. The natural length scale of growth front ranges from a few Å (lattice constants) to a few hundred Å (island and step sizes and diffusion lengths). As a result, fluctuations in the surface morphology are washed out in the diffraction pattern.

RHEED patterns consist of streaks normal to the growth surface. These diffraction streaks are characteristic of any surface periodicity and are called integral order streaks. For a crystalline surface, the spacing of the integral order streaks is inversely proportional to the surface lattice constant. In addition, for certain surfaces under certain growth conditions, a second set of diffraction streaks, more closely spaced than the integral order streaks, are present. This longer range order is due to reconstruction of the surface, where the topmost layer of atoms rearrange themselves to terminate any dangling bonds. During growth, the surface reconstruction and transitions in the surface reconstruction are used to calibrate flux ratios and substrate temperatures. Other information can be extracted from RHEED patterns: 3-d vs. 2-d growth, the presence of amorphous puddles on the surface, surface oxide desorption point, average island size, etc. The most common use of RHEED is to calibrate growth rates. Suppose the MBE conditions are chosen such that 2-d growth occurs. When a layer is nucleated, the growth front will initially consist of randomly distributed islands scattered across the surface. As more material is deposited, the islands grow together until the entire atomic layer has been filled in. The next monolayer of material then nucleates islands and the process continues. This modulation of the surface roughness causes the intensity of the specular RHEED spot to oscillate with a period equal to the growth rate.

In order to study the formation of the As/Sb interfaces, an *in situ*, time resolved measurement of the crystal during growth is needed. In this chapter, we report measurements of the dynamics of the growth surface of InAs/$Ga_{1-x}In_xSb$ SLS's using electron diffraction. We find that the streak spacing of RHEED pattern changes during growth. The dynamics of the streak spacing was found to be reproducible between growths using the same shuttering sequence at the GaInSb/InAs interface. The streak separation dynamics of growths employing different interface shuttering schemes was found to vary markedly.

5.3.2 Experimental Apparatus

In order to extract information from the RHEED pattern, we have developed a technique for digital data acquisition. First the diffraction pattern is videotaped using a CCD camera and a S-VHS video cassette recorder. We focus on the specular and first order streaks in order to most accurately measure the streak separation, but any portion of the RHEED pattern could be videotaped (see Fig. 5.5). The tape is then played back and digitized into a 640 x 480 array of single-byte data with a RasterOps framegrabber installed in a SPARC 2 workstation. To increase the data acquisition rate, only a portion of the videotaped pattern is digitized. The system can digitize between 2 and 10 frames/second depending on the size of the portion of the pattern that is being examined. After digitization the data can be either integrated to obtain intensity variations or fit with a Lorentzian plus a linear function to determine the streak positions. Recording large portions of the diffraction pattern on videotape provides a great deal of flexibility. One of the goals of this project is to identify which portions of the RHEED pattern are relevant to understanding the nature of the As/Sb interface. The ability to examine different parts of the diffraction pattern of the same growth is crucial for realization of this goal.

All of the samples studied were grown in a Perkin-Elmer 430 molecular beam epitaxy system equipped with cracked Sb and As sources. The strained layer superlattices (SLS) were grown on semi-insulating GaAs substrates and particular care was taken to use substrates from different boules in order to decrease the likelihood that the peculiarities of a particular lot of wafers would affect the data. The SLS's were grown on a thick stress relaxed GaSb buffer at a substrate temperature of $\sim 385\,^{\circ}\mathrm{C}$. The growth rate of the InAs was 0.12 monolayers/second and that of the GaInSb was 0.64 monolayers/second. The In mole fraction in the antimonide layers was 0.24. From x-ray diffraction analysis of the SLS's, they are coherently strained to the thick GaSb buffer with the InAs layers under 0.6% tensile stress,. and the GaInSb layers under 1.5 % compressive stress. A more detailed description of the growth can be found in reference [13].

5.4 Results from InAs/$Ga_{1-x}In_xSb$ Superlattices

Fig. 5.6 shows the measured spacing between the specular streak and the first order streak during the growth of an InAs/GaInSb SLS. Each period consists of 28 Å of InAs and 23 Å of $Ga_{0.76}In_{0.24}Sb$. At the end of each layer, before switching materials, the growth surface is soaked in Sb. Because of this soak the internal interfaces of the SLS are termed to be 'Sb-like.' The data were taken on the [110] azimuth at a rate of 2.5 data points per second. Fig. 5.6(a) shows the dynamic streak spacing for a single period of the SLS. The times at which the oven shutters are opened and closed are marked with arrows. Fig. 5.6(b) is an overlay of four consecutive periods of the SLS where the profile labeled 'period 1' is the one

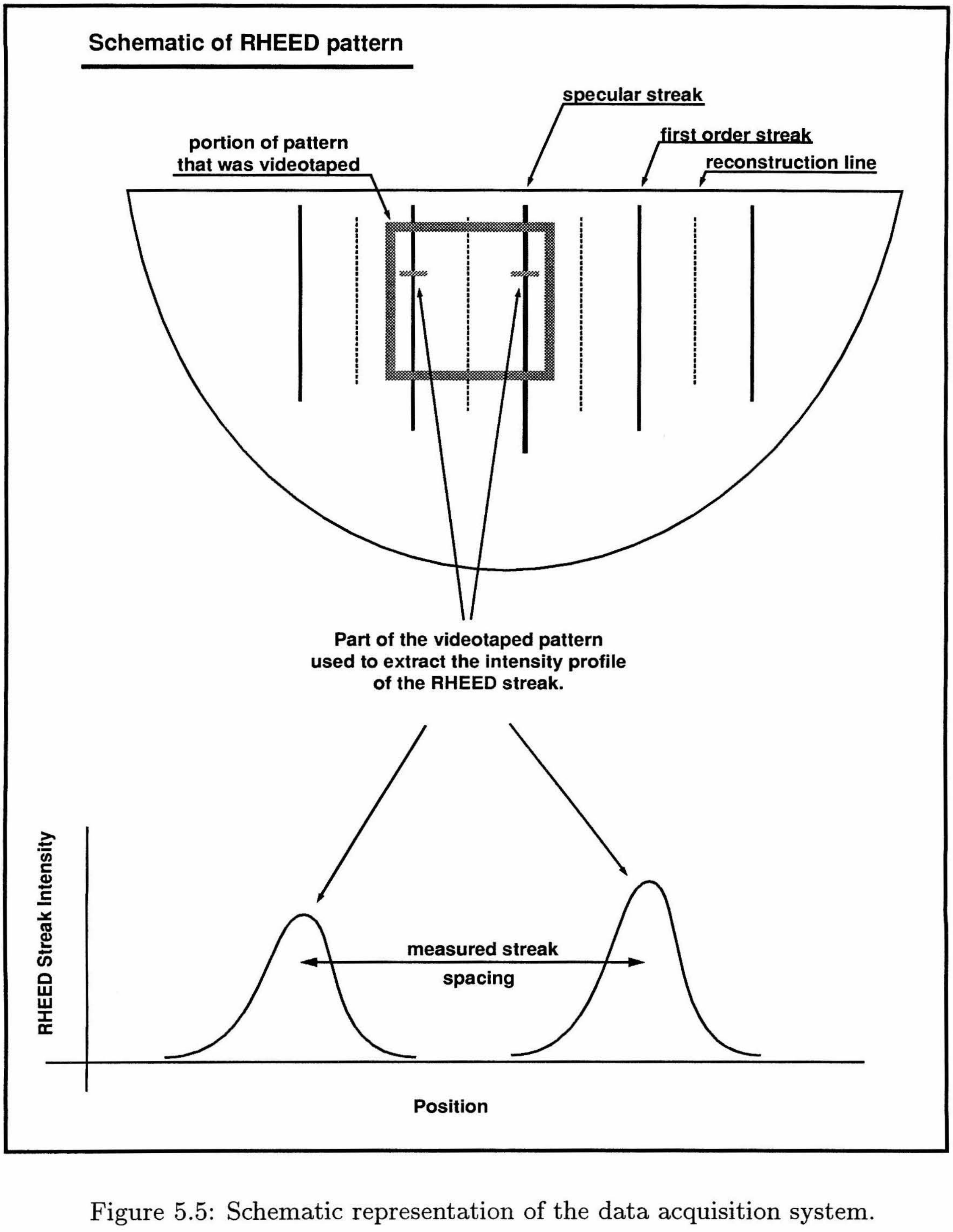

Figure 5.5: Schematic representation of the data acquisition system.

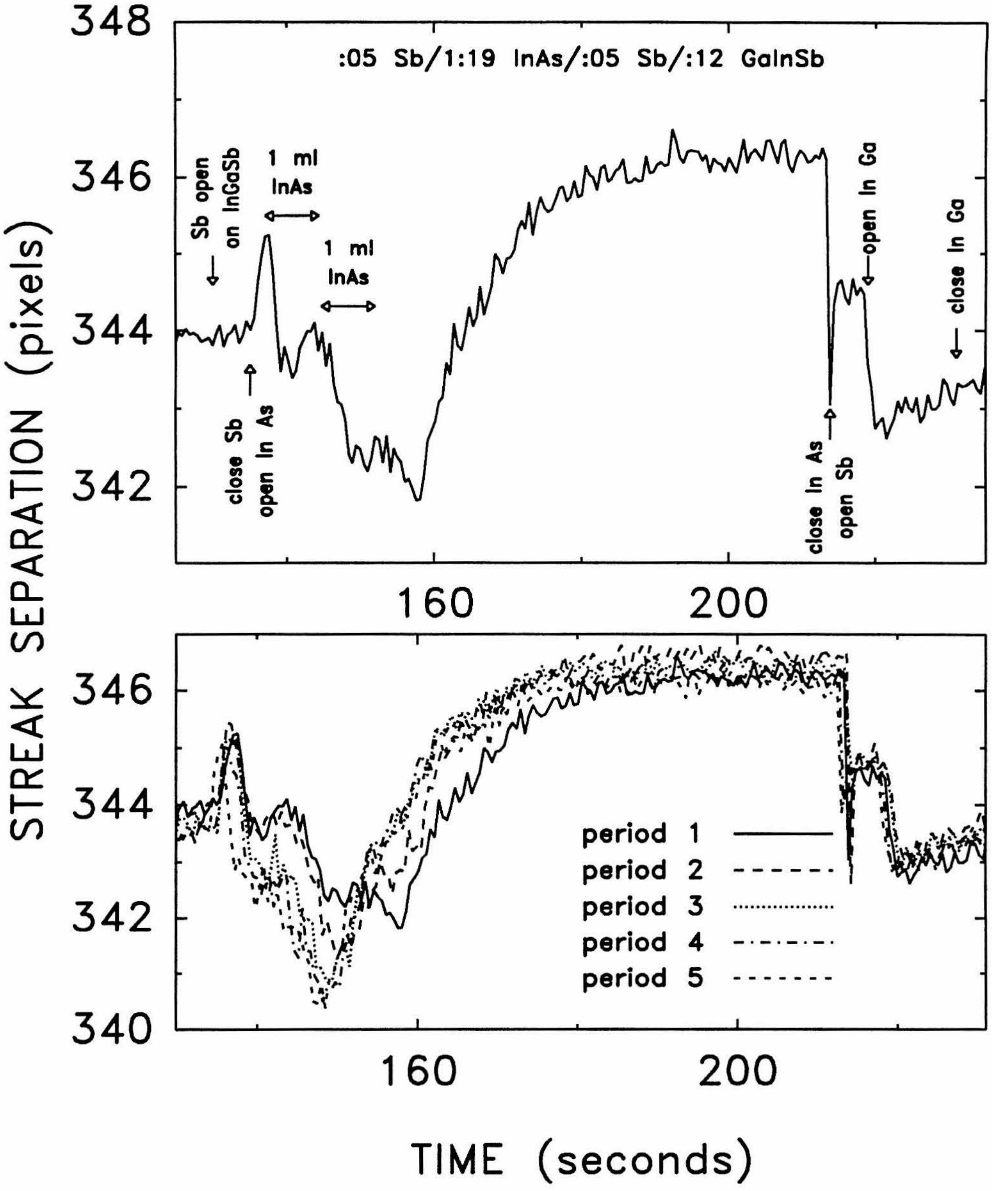

Figure 5.6: Separation between the specular streak and first order diffraction streak in the RHEED pattern of an InAs/$Ga_{1-x}In_xSb$ SLS. Fig. (a) notes the times when the shutters are either opened or closed, and Fig. (b) is an overlay of five consecutively grown periods of the SLS showing the reproducibility of the effect.

shown in Fig. 2(a). There are no vertical offsets in the data shown and the timing of the shutter actuations were determined from the clock on the VCR and period of the SLS. Three things stand out in the data. First, the apparent lattice spacing (ALS) – which is inversely proportional to the streak separation – of the surface of the crystal changes during growth. Secondly, abrupt changes in the ALS are correlated with either opening or closing a shutter. Thirdly, Fig. 5.6(b) shows that different periods of the same SLS have very similar dynamic streak spacings. Subsequent growths showed that when the same interface shuttering scheme was used, the profiles of the ALS matched those shown in Fig. 5.6.

To ensure that the features in the ALS that are correlated to the shutter openings are due to changes in the incident fluxes and not an electrical or mechanical artifact of the growth chamber, we measured the dynamic position of the specular and first order streaks while opening and closing the shutters of ovens that were at their idle temperature of 300 °C. The measurements were done on GaAs surfaces along both the [110] and $[1\bar{1}0]$ azimuths while growing GaAs and during As-flux soaks. To within our experimental resolution of about 0.5 pixels out of a streak spacing 420 pixels, neither the specular streak nor the first order streak moved. This indicates that the measured changes in the streak spacing when the shutters are actuated are due to changes in the incident flux and hence changes in the growth surface. It should be noted that the sizes of the measured shifts are small. In Fig. 5.6(a), the streak separation increases by about one pixel after the Sb shutter is closed and the In and As shutters are opened. This translates into $\sim 0.3\%$ change in the ALS.

In Fig. 5.7 we compare the measured streak spacing of the SLS shown in Fig. 5.6 with the intensity variation of the specular streak for slightly more than one period of the structure. The solid upper line is the data shown in Fig. 5.6 (a), and the lower dashed line is the intensity variation of the specular spot. The pairs of dotted vertical lines denote the extent of the Sb soaks. The two curves have similar shapes, and the plot of RHEED intensity has sharp features when the growth fluxes are changed just as in the case of the ALS profile. These intensity variations are reproducible when comparing different periods of the SLS. The features of importance in this graph are the oscillations in the intensity at the start of the InAs layer (second vertical line.) These oscillations have the same period as the oscillations in the streak separation with a period equal to the monolayer deposition time. These types of intensity oscillations are routinely used by many investigators to determine growth rates, and are believed to be caused by periodic changes in the roughness of the growth front.[17],[18] The strong correlation between the ALS profile and the RHEED intensity profile indicates that the streak separation modulation is sensitive to changes in the texture of the growth front.

We have examined the RHEED characteristics of roughly a dozen different interface shuttering schemes. In every case, abrupt changes in the ALS were correlated with changing the growth flux, and the changes in the ALS were reproducible between different periods of the SLS and different growths using the same or similar interface schemes.

Fig. 5.8 compares the measured streak spacing of two InSb-like SLS's grown with similar, but not identical interface shuttering schemes. The two structures have the same compositions and layer thicknesses and were grown under the same conditions. The data are vertically offset by four pixels for clarity. The extent of each Sb soak is marked by a pair of vertical dashed lines. The upper curve is the same as shown in Fig. 5.6(a). The difference between the shuttering schemes is that in the lower curve a single monolayer of In is deposited at the beginning and end of the InAs layer without an accompanying group V flux. The two curves are qualitatively similar but not identical. At the start and end of

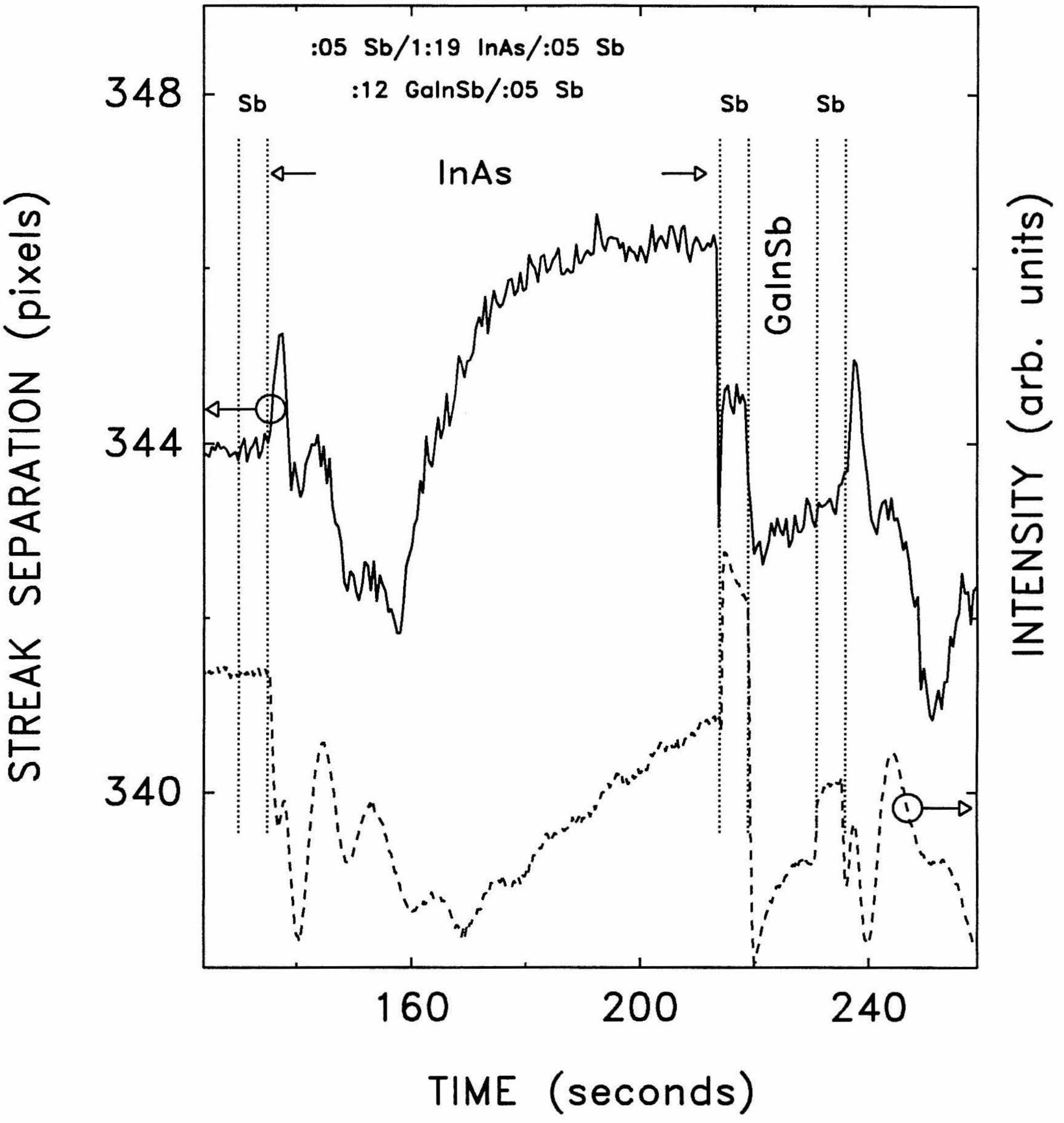

Figure 5.7: Comparison of the measured streak separation with the intensity profile of the specular streak. The upper solid line is the streak separation and the lower dashed line is the RHEED intensity. The extent of the Sb soaks are marked by the pairs of dotted lines.

the InAs layer (the second and third vertical lines respectively), the two curves are markedly different. These differences occur at precisely the times when the fluxes incident on the growth surface are different. This observation indicates that the measurement is sensitive to subtle changes in the growth surface. This similarity in ALS profiles when comparing similar interface shuttering schemes was observed in all the SLS's that were studied.

Fig. 5.9 compares the ALS profiles of two SLS's with the same layer thicknesses and compositions which were grown under the same conditions. The lower curve is the same as the lower curve in Fig. 5.8 (an InSb-like SLS). For the upper curve, each layer is terminated in an As soak, and 0.64 monolayers of $Ga_{0.76}In_{0.24}$, without an accompanying group V flux, are deposited at the beginning and end of the GaInSb layer: a GaInAs-like SLS. The two curves are vertically offset by five pixels for clarity and the positions of the group V soaks are marked by the pairs of vertical lines, Sb in the case of the lower curve and As for the upper curve. In this case the interface shuttering schemes are very different as are the ALS profiles. While both curves show decreasing streak separation, with oscillations having a period equal to a monolayer deposition time, at the start of the InAs layer, the net change in the streak separation during growth of the InAs layer is different for the two SLS's. In the upper curve (GaInAs-like) the separation decreases over the course of the InAs layer while in lower curve (Sb-like) the streak separation has increased after growing the InAs layer. In addition, the response of the ALS to the group V soaks is very different. In the upper curve, the ALS does not change during the As soaks of the InAs layer (see the third vertical line) while at the interrupts on the GaInSb layers (the first and fifth lines) the streak separation rises very slightly. In the lower curve, the ALS is not effected by the Sb soaks on the GaInSb layers (first and fifth vertical lines) while the ALS changes markedly at the Sb soak on the InAs layer and at the start of the GaInSb layer. The sharp

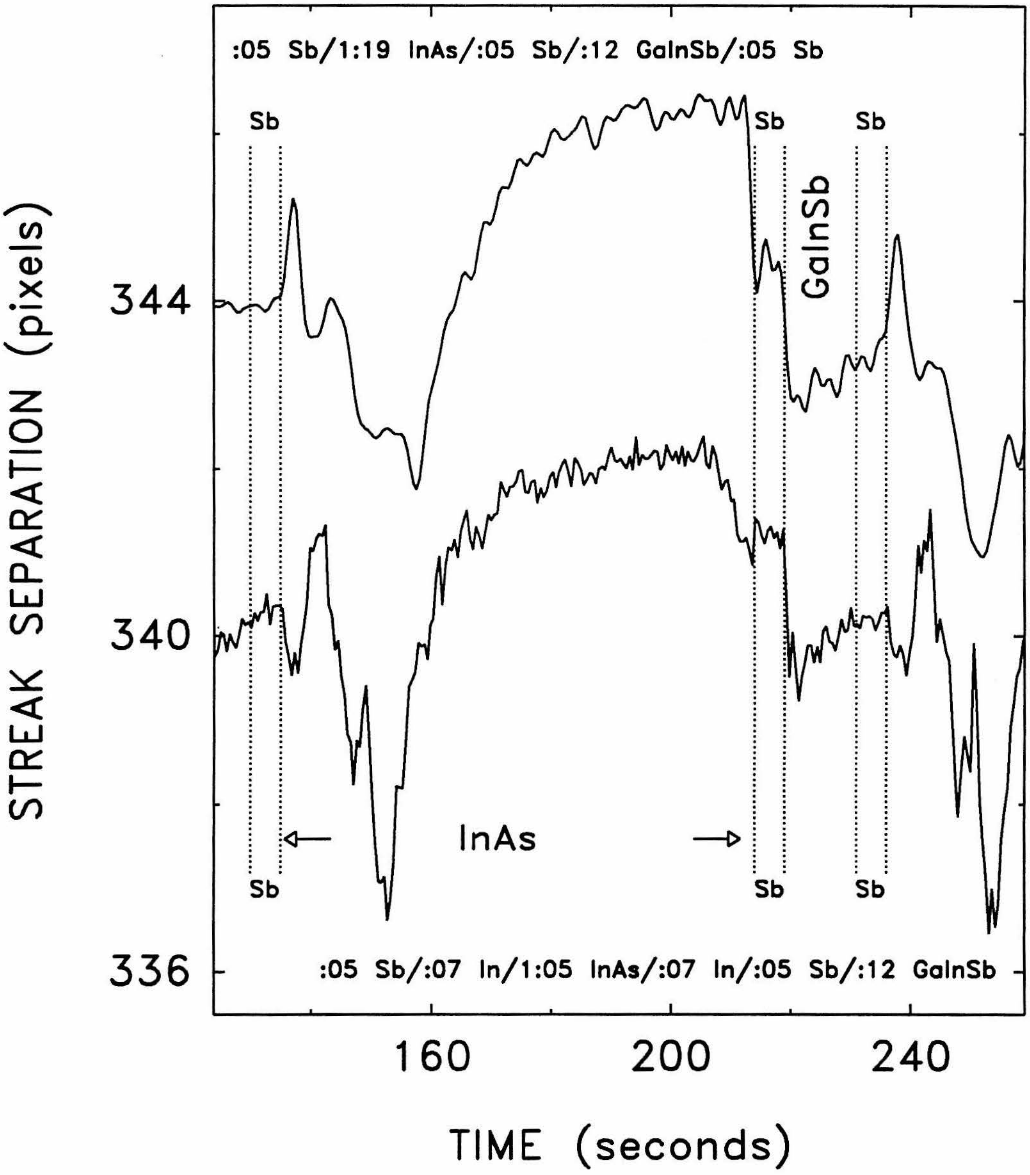

Figure 5.8: Comparison of the measured streak separation of two superlattices with the same layer thickness and compositions both of which were grown under the same conditions. The extent of the Sb soaks are marked by the pairs of dotted lines.

dip in the streak separation in the upper curve during the GaInSb layer (between the fourth and fifth lines in the upper curve) is a reproducible feature and not a noise spike. Fig. 5.9 shows that the ALS profiles of structures grown with very different interface shuttering schemes are correspondingly different.

These two type of interface schemes shown in Fig. 5.9 are especially interesting to compare. We have found that undoped SLS's grown with Sb-like interfaces have a p-type background carrier concentration as determined by low temperature, four-point Hall measurements and that undoped As-like, SLS's have n-type background carrier concentrations. It is our hope that careful study of the RHEED characteristics of these different shuttering schemes will help us understand this behavior.

5.5 Discussion of Superlattice Results

Interpreting the change in streak separation of these SLS's is complicated. The greatest difficulty is understanding the relationship between the surface periodicity we are measuring and the final bulk lattice constant. X-ray diffraction measurements on these structures show that the SLS's are coherently strained to the GaSb buffer layer, yet the periodicity of the growth front is clearly changing. One possibility is that as the strained material is grown, it nucleates in islands which have interatomic spacings intermediate between those of the coherently strained structure and the natural lattice constant of the material. If this were the case, it would only be after the islands coallessed and were buried under subsequent layers that the material would reach its final, coherently strained lattice constant. This explanation is consistent with oscillations in streak separation having a period equal to the monolayer deposition time. A second difficulty is that the RHEED pattern moves during growth. We have observed rotations of

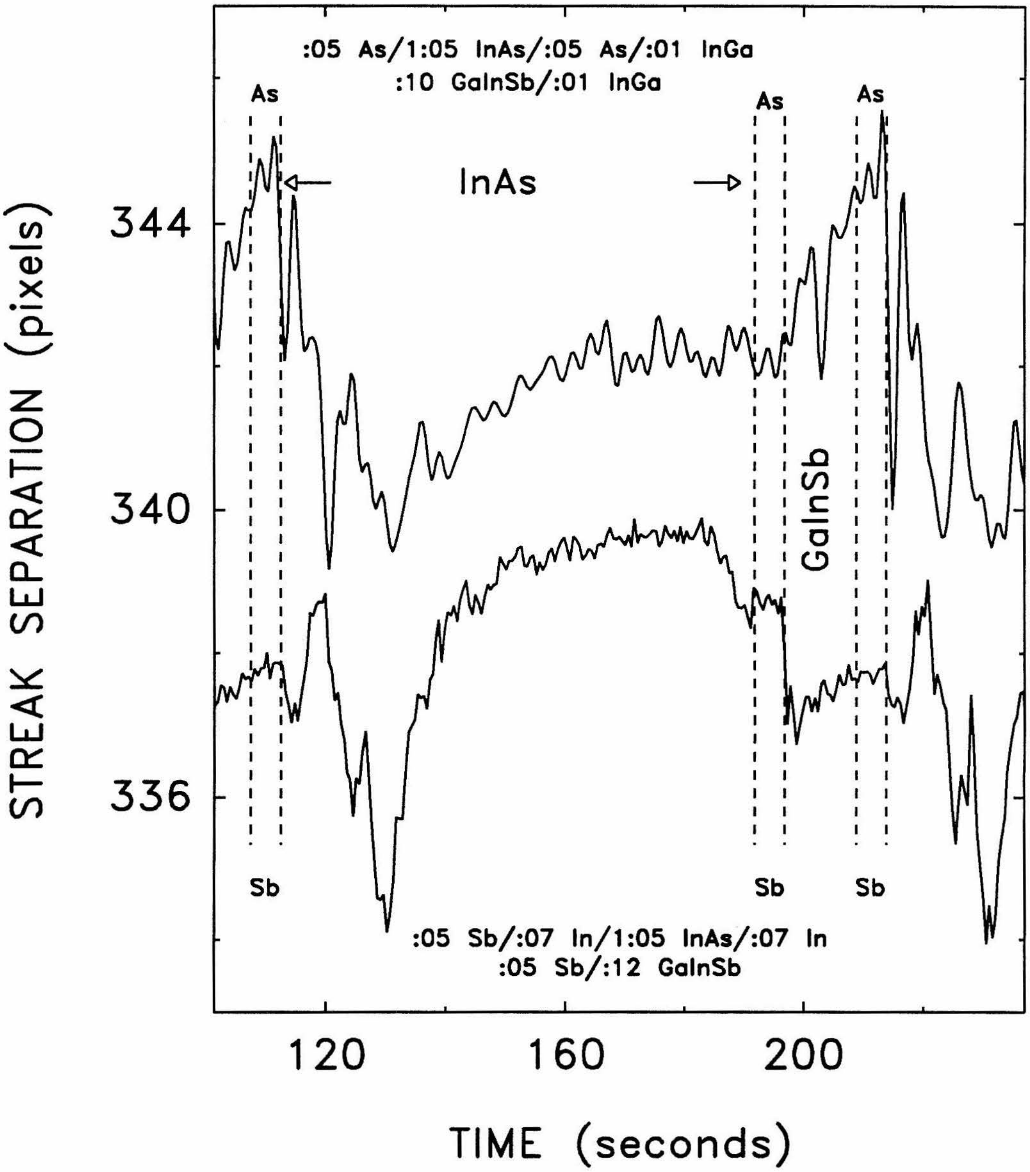

Figure 5.9: Comparison of the measured streak separation of two superlattices with the same layer thickness and compositions both of which were grown under the same conditions. The extent of the group V soaks are marked by the pairs of dotted lines, Sb for the lower curve and As for the upper curve.

the diffraction pattern about an axis parallel to the direction of electron travel and translations normal to the direction of electron travel or both. Without corrections for these effects, quantitative measurements are impossible. Finally, the dearth of techniques which are capable of probing the chemistry and structure of individual, buried interfaces complicates analysis of the final structures. Nevertheless, we are hopeful that this technique will prove to be useful in understanding mixed anion interfaces at least to the level of providing an empirical tool for growth of high quality, reproducible SLS's.

5.6 Summary

In conclusion, we have used RHEED to study the surface periodicity of the growth front of InAs/GaInSb SLS's. We found that the apparent surface lattice spacing reproducibly changed during growths which subsequent X-ray measurements indicated were coherently strained. Abrupt changes in the measured streak spacings were found to occur when the oven shutters were either opened or closed. Care was taken to check that these changes in the RHEED pattern were due to changes in the fluxes incident on the growth surface and not electrical or mechanical artifacts of the shutter actuator mechanism. The profile of the dynamic streak spacing was found to be reproducible when comparing consecutive periods of a SLS's or different SLS's employing the same shuttering scheme at the InAs/GaInSb interface. Finally, when the interface shuttering scheme was changed it was found that the dynamic streak separation profile also changed. Large changes in the shuttering scheme led to dramatic differences in the streak separation profile, and small changes in the shuttering scheme led to minor changes in the profile. In both cases, the differences in the surface periodicity profile occurred at the parts of the growth where the incident fluxes differed.

References

[1] D.L. Smith and C. Mailhiot, *J. Appl. Phys.* **62**, 2545 (1987).

[2] D. H. Chow, R. H. Miles, J. N. Schulman, D. A. Collins and T. C. McGill, *Semi. Sci. and Tech.*, 6(12C), 47 (1991).

[3] R.H. Miles, D.H. Chow, J.N. Schulman and T.C. McGill, *Appl. Phys. Lett.* **57**, 801 (1990).

[4] D. H. Chow, R. H. Milesand A. T. Hunter, *J. Vac. Sci. Technol. B* **10**, 888 (1992).

[5] E.R. Brown, C.D. Parker, L.J. Mahoney, J.R. Soderstrom and T.C. McGill, 48th Annual Device Research Conference Abstracts, IEEE Trans. Electron Devices, November 1990.

[6] H.K. Choi and S.J. Eglash, *Appl. Phys. Lett.*, **61**, 1154 (1992).

[7] D. A. Collins, D. H. Chow and T. C. McGill, *Appl. Phys. Lett.*, **58**, 1673 (1991).

[8] G. Tuttle, H. Kroemer and J. English, *J. Appl. Phys.*, **67**, 3032 (1990).

[9] K. Yoh, H. Taniguchi, K. Kiyomi and M. Inoue, *Jpn. J. Appl. Phys.*, **30(12B)**, 3833 (1991).

[10] X. Li, K.F. Longenbach, Y. Wang and W.I. Wang, *IEEE Elec. D*, **13(4)**, 192 (1992).

[11] S.R. Kurtz, L.R. Dawson, R.M. Biefeld, I.J. Fritz and T.E. Zipperian, *IEEE Elec. Dev. Lett.*, **10**, 150 (1989).

[12] J.R. Waldrop, G.J. Sullivan, R.W. Grant, E.A. Kraut and W.A. Harrison, *J. Vac. Sci. Technol. B* **10**, 1773 (1992).

[13] D.H. Chow, R.H. Miles, C.W. Nieh and T.C. McGill, *J. Cryst. Growth*, **111**, 683 (1991).

[14] J.M. VanHove, C.S. Lent, P.R. Pukite and P.I. Cohen, *J. Vac. Sci. Tech.*, **B1**, 741 (1983).

[15] J.H. Neave, B.A. Joyce, P.J. Dobson and N. Norton, *Appl. Phys.*, **A31**, 1 (1983).

Chapter 6

RHEED and XPS Observations of Surface Exchange Reactions

6.1 Introduction and Outline

Chapter 5 showed the wealth of information contained in the RHEED pattern during the growth of mixed anion superlattices (SL). It was shown that the dynamics of the RHEED pattern gave a reproducible signature for how the internal interfaces of InAs/GaInSb SL's are formed. Because the information was real-time and time-resolved, it suggests the possibility that detailed analysis of the diffraction pattern could greatly increase our understanding of the growth of these devices. The drawback of the work presented in Chapter 5 is that too much information, about a very complicated system, is available. In an attempt to understand the physics and chemistry of these complex structures, we carried out a study of a much simpler system. In this chapter we concentrate on the formation of these mixed anion interfaces by examining the effect of exposing an InAs surface to an Sb flux.

As noted in Chapter 5, the fashion in which the As/Sb interface is formed can greatly affect macroscopic device performance[1, 2, 3]. One way to form the interface is to briefly expose the arsenide layers to an Sb flux before depositing the antimonide layer. Typically these Sb soaks last 5 - 10 seconds. It is believed that this leads to a layer of Sb-In chemical bonds which are thought to give superior performance in field effect devices and infrared SL detectors. (Similarly, when depositing InAs on GaSb an analogous layer of Ga-As bonds can be formed.) The samples studied for this chapter were grown to mimic the Sb soaks that are typically employed before nucleating an antimonide layer on an arsenide layer.

In this chapter we report the results of two complimentary studies of these soaks using x-ray photoelectron spectroscopy (XPS) and RHEED. The XPS measurement gives chemical information about the crystal's surface, but has no time resolution. In essence, the XPS can deliver a chemical 'snapshot' of the surface after a particular soak length. The RHEED experiment is time resolved and can be carried out during the Sb/InAs soak. However, since RHEED is a diffraction technique, it carries no information about the chemistry of the surface. By combining the time resolution of RHEED with the chemical information from XPS, we believe we have developed an indirect, real-time probe of an anion, surface exchange reaction.

From the XPS study, we find that exposing an InAs surface to an Sb flux initiates an Sb/As exchange reaction. Using the data we can estimate the time needed for the reaction to go to completion. The XPS data also indicate that the exchange reaction is self-limiting after the topmost layer of As has exchanged. We also find that when an InAs surface is exposed to an Sb flux, the intensity of the specular RHEED spot first decreases then recovers toward its initial value. The time needed for the RHEED pattern to stabilize after starting the Sb soak is extremely reproducible as long as the absolute Sb flux and the Sb species employed are held constant. The stabilization time (ST) is much shorter when using a beam of cracked Sb (consisting mainly of Sb_2 with some Sb) as opposed to a beam of uncracked Sb (composed exclusively of Sb_4). Increasing the absolute Sb flux also decreases the ST of the diffraction pattern. The RHEED data are compared to the XPS results. The times obtained from the XPS experiments are in good agreement with the ST from the RHEED patterns. The effect on the ST of varying the Sb flux and Sb species as well as the good agreement between the XPS data and the RHEED data are consistent with the conclusion that the temporal changes in the RHEED intensity are due to the Sb/As exchange reaction.

In the following section we describe both the RHEED (6.2.1) and XPS (6.2.2) measurements. In Sections 6.3 and 6.4 we give the results of the XPS and RHEED experiments, respectively. Section 6.5 compares the RHEED and XPS data and the chapter is summarized in Section 6.6.

6.2 Experimental

The samples studied were grown under the same conditions as those in Chapter 5. The samples consisted of 100 Å thick InAs layers grown at a rate of 0.5 monolayers/second. The InAs epilayers showed a 2×4 RHEED reconstruction during growth, indicating that the growth front was As rich[6]. After growth, the sample was soaked in an As flux for a few minutes to ensure that all of the In bonds were terminated with As. The samples were grown on relaxed InAs buffer layers deposited on (100) GaAs substrates. The growth of the InAs was followed by exposing the epilayer to an Sb flux. Two groups of samples were concurrently grown: a set for XPS and a set for RHEED analysis. Before growing each XPS sample, a RHEED measurement was made so that the results of the two data sets could be compared. The RHEED measurement consisted of videotaping the diffraction pattern on the (110) azimuth while soaking an InAs surface in Sb. These Sb soaks typically lasted 1 minute. Following this, the surface was buried under an InAs layer and an XPS sample was prepared under the same MBE conditions.

A range of Sb species were used. The Sb cell used to prepare the samples consists of two thermally isolated zones. Each of the zones is equipped with a heating filament so that the temperatures can be individually controlled. The first filament sublimates Sb off of a bulk charge. Typical bulk evaporator temperatures are 510-550 °C. The temperature of second, or cracking zone, can be varied between 520 and 1050 °C without appreciably affecting the absolute Sb flux. In the cracker, Sb_4 from the bulk evaporator can be broken down into Sb dimers and/or monomers depending on the cracker temperature. For the XPS experiments two different cracker temperatures were investigated. The resulting Sb_x beams will be referred to as cracked and uncracked Sb. We estimate that the cracked Sb flux consisted primarily of Sb_2 with some Sb while the uncracked flux was entirely Sb_4[5]. For the RHEED experiments the full range of cracker temperatures were investigated.

6.2.1 RHEED Measurements

The videotape of the RHEED screen was digitized and a computer program tracked and recorded any changes in the intensity and width of the specular spot during the Sb soaks. The system used to digitize and analyze the RHEED pattern was similar to the one in Chapter 5, except that a DataCell S2200 framegrabber was substituted for the previous card. This upgrade resulted in a marked increase in the speed and flexibility of the system. With the new card it was possible to obtain 30 - 50 data points per second.

6.2.2 XPS Measurements and Data Analysis

The XPS measurements and analysis were carried out by another student, and a complete discussion of them can be found elsewhere[4]. A brief summary is included here in the interest of readability. In XPS, x-rays are directed at the surface of the sample. The x-rays eject photoelectrons from the crystal which are passed through a hemispherical energy analyzer. Even though the penetration depth of the x-rays is $\approx 1\mu$m, the escape depth of the photoelectrons is typically 20 - 30 Å [7, 8, 9]. Because of this, XPS is only sensitive to the near surface region of the sample. The photoelectrons come from two distinct sources. Studying the energies of electrons ejected from the energy bands of the crystal allows experimental determination of the band offsets between two semiconductors[10]. (Though not reported in this thesis, a large number of structures were grown for this purpose.[11, 12, 13, 14, 15]) The second flavor of photoelectrons – which were examined for this work – are those from deep within the atomic cores of the crystal's constituent atoms. Because these electrons are largely shielded from the rest of the crystal by the valence electrons, their energies are characteristic of the individual atoms that make up the lattice. By examining the energy spectrum of the photoelectrons, it is possible to determine what types of atoms are present in the crystal[10]. Comparing the intensities of peaks due to different chemical species leads to estimates of relative abundances. Detailed studies of the shapes and any energy shifts in these core-level peaks gives information about what types of chemical bonds are present in the crystal[12, 10].

The XPS measurements were obtained using a Perkin-Elmer Model 5100 analysis system with a monochromatic Al Kα source (hv = 1486.6 eV). All of the samples studied were transferred from the growth chamber to the XPS chamber via an ultra high vacuum transfer tube. The base pressure in the XPS chamber was typically $\sim 1 \times 10^{-10}$ Torr. Care was taken to ensure that the escape orientation of the photoelectrons remained constant from sample to sample to minimize any electron diffraction effects due to the single crystalline nature of the samples.

The difficulty in obtaining results with XPS lies in the analysis and not the data collection, which is rather straightforward. Fig. 6.1 (a) is a plot of the photoelectron energy loss spectrum from an InAs surface exposed to an Sb_2 flux for 15 seconds. Evident in the spectrum are the As $3d$ and In $4d$ core-level peaks from the InAs epilayer, as well as an Sb $4d$ peak that was not present before the Sb soak. To infer the stoichiometry of the surface it is necessary to measure the relative areas of the three core-level peaks. This was done by first making measurements on reference samples. These included bulk InAs, GaAs and GaSb epilayers as well as a metallic Sb film. From these it was possible to obtain the shapes of the individual core level features – As $3d$, In $4d$ and Sb $4d$ – by fitting them to Voight functions. (Note that each of the three features actually has two peaks. This is due to the splittings between spin up and spin down electrons in the various atomic levels.) To obtain the core-level peak areas in the samples of interest, the corresponding peaks from the reference standards were fit to the experimental data. When fitting the data from the InAs surfaces soaked with Sb, the magnitude and position of the reference peaks were free parameters while their shapes were fixed. Before measuring the core-level intensities, through the fitting procedure discussed above, the individual peaks must be isolated. As shown in Fig. 6.1 (a), there is a slowly rising background as you move to higher binding energy which must be removed from the experimental data. In addition there are plasmon replicas of the core-level peaks, which must be stripped from the spectrum before measuring any peak areas. These subtractions were accomplished by using the spectra of the reference samples. Fig. 6.1 (b) shows

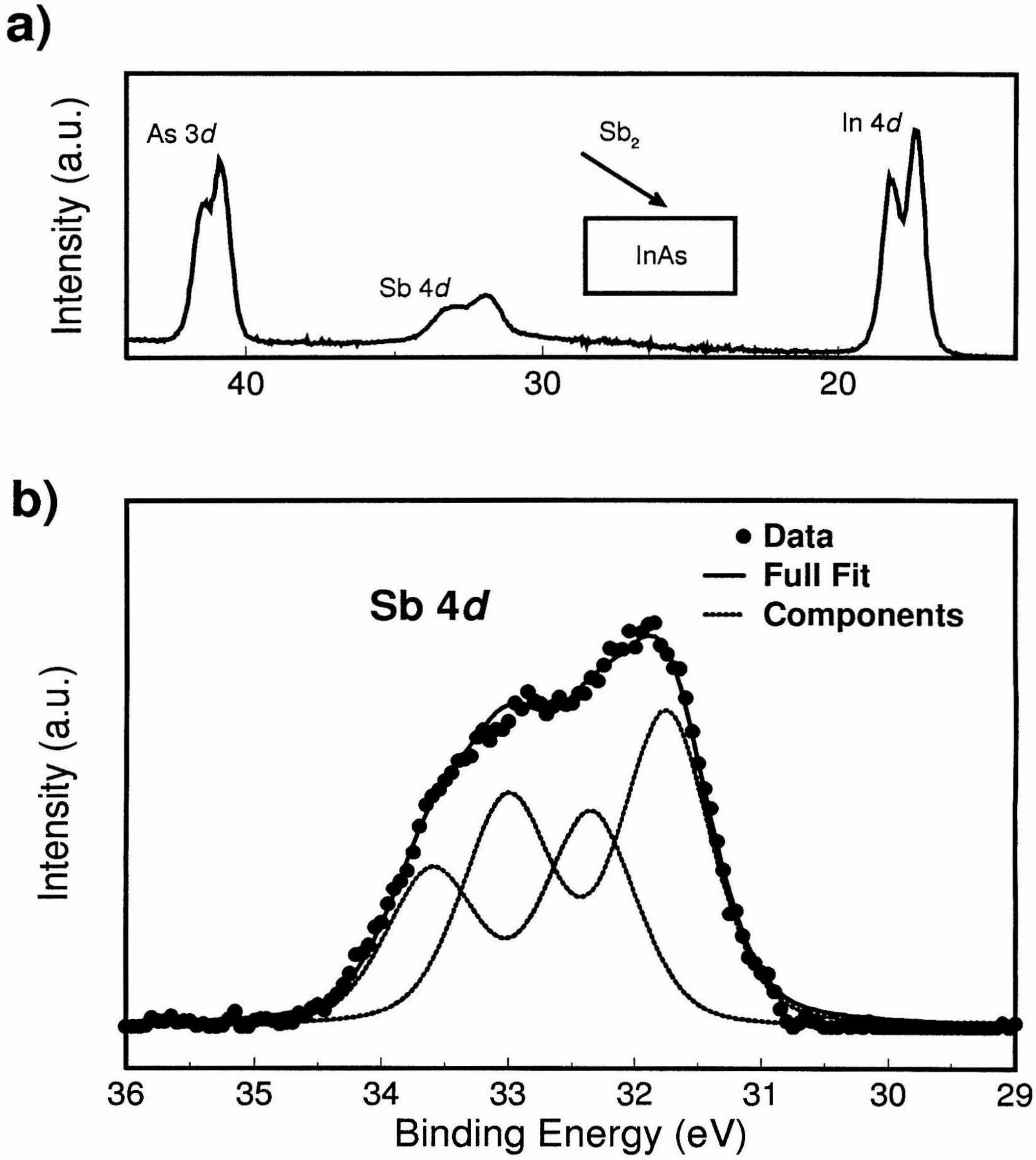

Figure 6.1: XPS data from an Sb soaked InAs surface. Panel (a) shows core level peaks associated with In, As and Sb atoms. Panel (b) is a blow up of the Sb 4d peak after the background has been subtracted, along with its numerical fit. To get an estimate of the Sb coverage, a similar fit was done on the In peak and the ratio of the areas of the Sb and In peaks was compared.

the resulting fit. The experimental data shown has been stripped of both a slowly rising background and a plasmon replica from the In $4d$ peak which coincides with the Sb $4d$ core-level. The peak shapes used to fit the data are shown as well as the final fit. The origin of the chemically shifted second peak is discussed below.

6.3 XPS Results

For the XPS study, a series of InAs epilayers were soaked in either cracked or uncracked Sb fluxes. The length of the Sb soaks varied from 2 seconds to 15 minutes. These samples were then transferred under UHV to an analysis chamber where their electron energy loss spectra were obtained (see Fig. 1.2). The core-level peak areas were then measured by the method detailed in section 6.2.2. The measured (Sb $4d$)/(In $4d$) peak area ratios, as a function of either Sb_2 or Sb_4 soak time, are shown in Fig. 6.2. Note that the measurement of Sb surface coverage is a relative and not an absolute one. This is due to the uncertainty in the escape depths of the photoelectrons[7, 8, 9]. The contribution of any particular atomic layer to the overall photoelectron spectrum is an exponentially damped function of distance from the crystal's surface. Because of this exponential dependence and the uncertainty in electron escape depths, it is difficult to make absolute measurements of chemical abundances with XPS alone.

The XPS data in Fig. 6.2 leads to four main conclusions. First, after even the shortest Sb soaks there is Sb present on the crystal surface. Though not shown, it was also found that the As $3d$ to In $4d$ ratio decreased as the strength of Sb $4d$ signal increased. Further, the magnitude of the drop in the As $3d$ signal was consistent with the amount of As present on the surface of the crystal decreasing by roughly the same amount that the Sb coverage increased. From this we conclude that the Sb has exchanged with As atoms from the crystal and

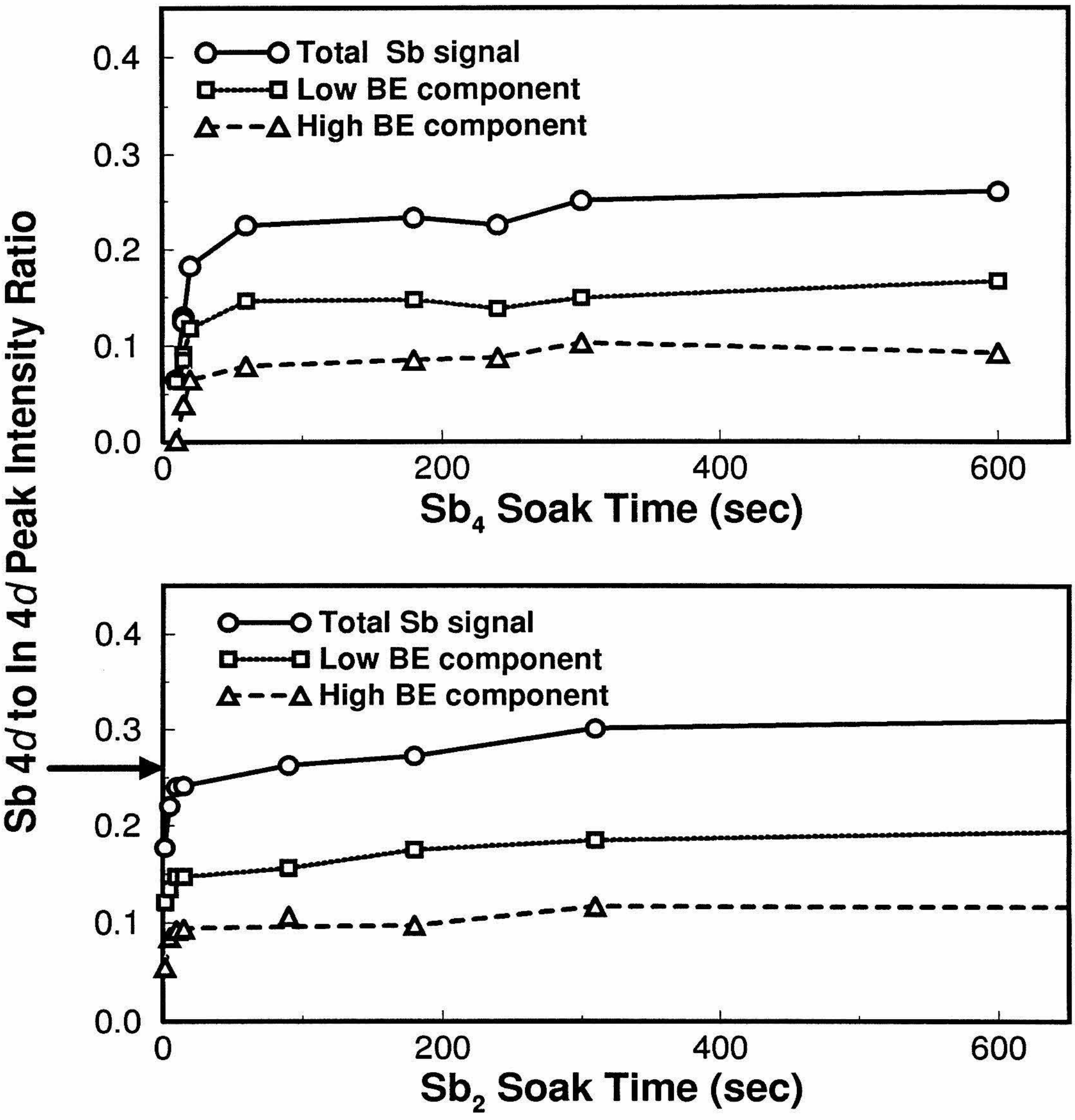

Figure 6.2: Sb 4*d*/In 4*d* peak area ratios as measured by XPS. The data were measured on InAs surfaces that were exposed to Sb_x soaks of differing durations. The upper panel shows the result of soaking the InAs in Sb_4. The lower panel is for Sb_2 soaks.

is not merely being deposited on top of the InAs epilayer. Second, comparing the data in the two panels shows that this exchange reaction occurs much faster when using cracked Sb (Fig. 6.2 (b)) instead of uncracked Sb (Fig. 6.2 (a)). Third, the size of the Sb peak initially increases rapidly then saturates and shows only a slow increase afterwards. The level at which the Sb $4d$ to In $4d$ peak area ratio saturates is consistent with the exchange of only the topmost As layer with Sb from the beam flux. This indicates that the surface exchange reaction is self-limiting. Fourth, the Sb $4d$ core-level actually consists of two components. (Fig. 6.1 (b) shows that two doublets, one shifted in energy and diminished in intensity, are needed to fit the experimental data.) Studying the behavior of the two components leads to the conclusion that the lower binding energy peak is due to Sb that exchanges with As in the crystal and bonds with In atoms. The high binding energy peak is attributed to the formation of small islands of metallic Sb on the crystal surface[4].

These XPS results should have a major impact on device growth. First, we have conclusive proof that these Sb soaks do initiate an anion exchange reaction. Next, the data indicates this reaction is self-limiting. This suggests that in order to ensure the Sb/As exchange goes to completion, longer Sb soaks can be employed without the danger of depositing additional Sb or exchanging more As out of the crystal. The minimum length of the Sb soak needed to complete the exchange reaction depends strongly on the composition of the beam flux. Finally, the presence of the metallic Sb islands on the InAs/Sb surface must be accounted for to ensure optimal crystal quality. Growth experiments to test the implications of these XPS measurements are currently being undertaken.

6.4 RHEED Results

In Fig. 6.3 we plot the measured change in the specular spot intensity of the RHEED pattern when an InAs surface is exposed to an Sb flux. The data were taken with the cracking zone of the Sb effusion cell at different temperatures. We estimate that for the bottom curve the Sb flux consisted entirely of Sb_4 while for the top curve the Sb flux was predominantly Sb_2 with some Sb[5]. The curves are labeled with the nominal Sb cracker temperature used when obtaining them. The Sb beam composition monotonically changes between these extremes. The start of the Sb soak is denoted by the dashed vertical line and the data are vertically offset for clarity. The substrate temperature and total Sb flux were held constant for all the data shown.

The curves in Fig. 6.3 are qualitatively similar. In each of them the specular intensity decreases at the start of the Sb soak then recovers back toward its value before the Sb soak was initiated. The difference between the curves is the time needed for the specular spot intensity to stabilize after exposing the InAs surface to the Sb flux. From Fig. 6.3 it can be seen that the ST monotonically decreases as the cracking zone temperature increases. From the XPS results in Section 6.3, we know that an Sb/As surface exchange reaction will occur in this situation. Further, physical intuition suggests that the exchange reaction will occur faster for a flux of either Sb or Sb_2 than for a flux of Sb_4. This is because Sb and Sb_2 should be more reactive than Sb_4 (otherwise Sb_4 would not be the dominate species that sublimes from solid Sb.) Also, assuming that the absolute Sb flux is held constant, when the Sb is cracked the number of Sb_x particles increases. This leads to higher Sb coverage of the InAs surface, and consequently a faster Sb/As exchange reaction. The behavior of the ST in Fig. 6.3 is consistent with the changes in the diffraction intensity being due to the As/Sb exchange.

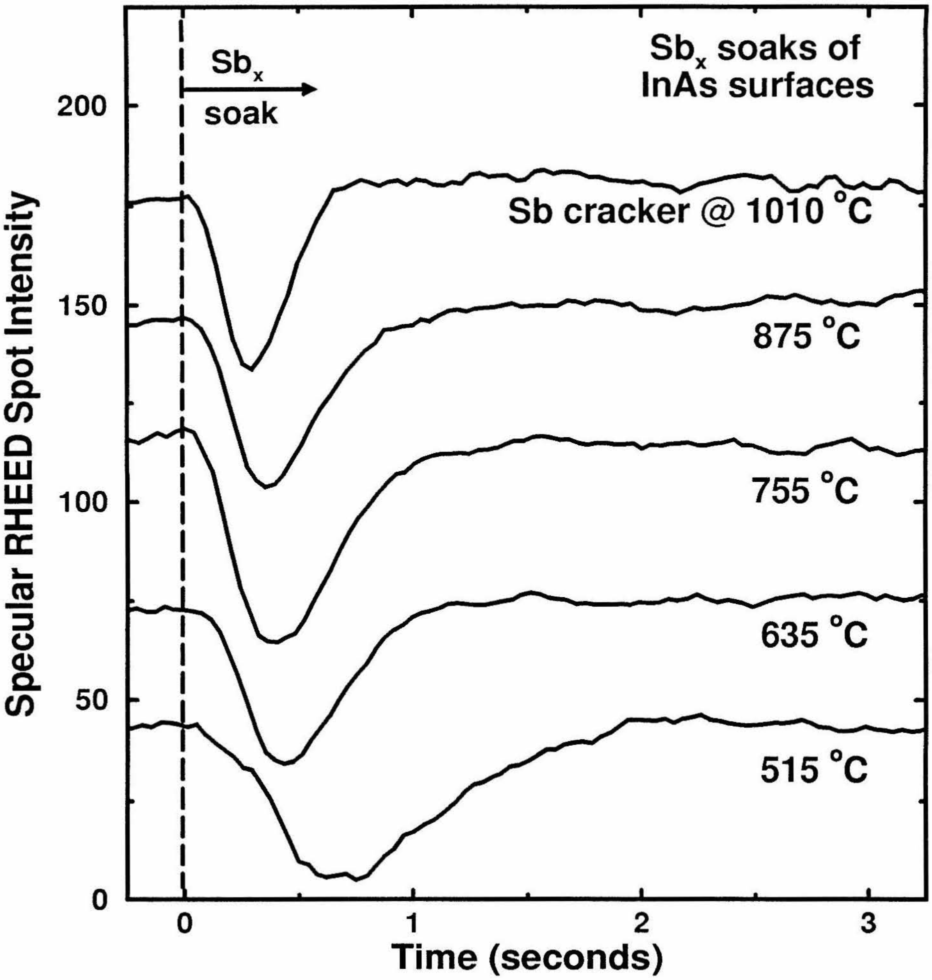

Figure 6.3: Plots of the change in the specular RHEED spot intensity during Sb/As exchange reactions. The curves are vertically offset for clarity. The dashed vertical line denotes when the InAs surfaces are first exposed to an Sb$_x$ flux. The lowest curve was obtained by exposing an InAs surface to an Sb$_4$ flux. In the upper curve the beam consisted mainly of Sb$_2$ with some Sb. For the middle curves an intermediate Sb flux composition was used. Each data set is labeled with the nominal Sb cracker temperature used.

Fig. 6.4 shows the reproducibility of the data discussed above. The two panels show overlays of RHEED data taken over the course of about six weeks. The upper panel shows data taken while using a cracked Sb beam (mainly Sb_2 with some Sb) and the data in the lower panel was taken while using Sb_4. The dashed vertical lines indicate when the Sb soak was started. Great care was taken to hold the substrate temperature and absolute Sb flux constant. The curves within each panel are very similar. The profiles of the intensity decreases are extremely similar in size, shape and length of time. Most importantly, the ST is the same for the different curves. The only difference between the curves is the final value of the diffraction intensity which we believe is due to surface morphology and not the exchange reaction itself[16].

We also looked at the effect of varying the bulk Sb cell temperature for fixed cracker temperatures. We found that the ST was inversely proportional to the bulk cell temperature. By comparing the ST to Sb vapor pressure tables we found that the ST scaled as one over the total Sb flux. This further indicates the the RHEED dynamics are characteristic of the Sb/As surface exchange reaction. The ST's scaling behavior, with respect to absolute Sb flux, also suggests that the Sb/As exchange rate is limited by the arrival of Sb and not the exchange reaction itself.

6.5 Comparison of RHEED and XPS Results

In Fig. 6.5 we show a comparison of representative RHEED data from Fig. 6.4 with XPS measurements of the relative Sb coverage of InAs surfaces after Sb soaks of various lengths. As can be seen from the data, the ST of the RHEED pattern corresponds quite closely with the time measured by XPS for the Sb/As exchange reaction to saturate. The minimum in the temporal RHEED intensity profile

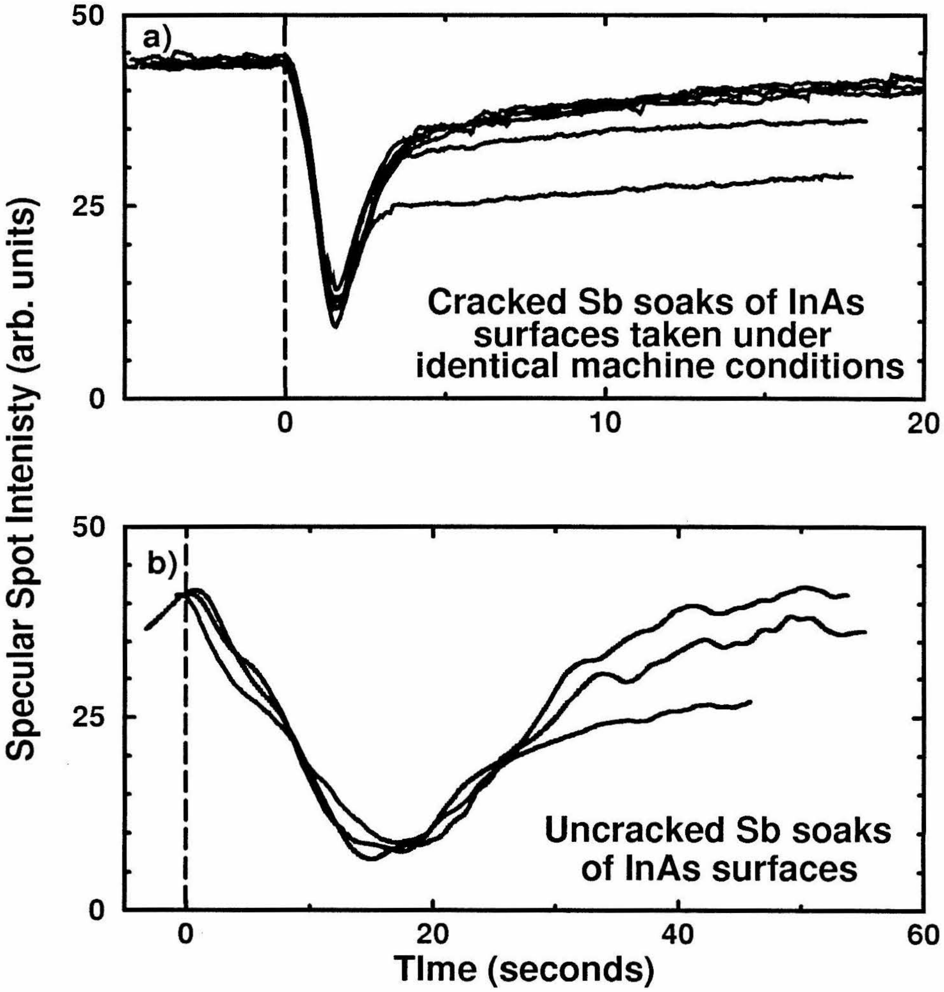

Figure 6.4: Overlays of plots of the change in the intensity of the specular RHEED spot while the anion exchange reaction is occurring. The dashed vertical lines signify when the InAs surfaces are exposed to the Sb flux initiating the As/Sb exchange reaction. The upper panel shows data taken when the Sb flux was predominantly composed of Sb and Sb_2, while in the lower panel a beam composed exclusively of Sb_4 was used. The group of curves within each panel show several measurements of the exchange reaction taken under identical machine conditions showing the reproducibility of the RHEED dynamics.

corresponds to a fractional Sb coverage. This suggests that the change in the RHEED intensity during the Sb soak could be due to a mechanism similar to that believed to cause RHEED oscillations during MBE growth: temporal modulation of the surface roughness[17, 18]. The roughness could be morphological since there will be large Sb atoms diffusing across the InAs surface during the exchange reaction. Also, the XPS results indicated the formation of islands of metallic Sb on the crystal's surface. These islands could be the cause of the intensity modulations. Another possible source of the surface 'roughness' could be the stoichiometry of the surface. At the start of the Sb soak As will cover the crystal surface (with the growth conditions employed). By the time the RHEED pattern stabilizes, the XPS measurements show that Sb is the dominate surface species. Since the form factors for electrons scattering off of Sb and As differ, this could lead to the 'surface roughness' used to explain RHEED intensity oscillations during MBE growth.

6.6 Summary

In summary, we have used RHEED and XPS to explore a surface exchange reaction. From the XPS study, we know that exposing an InAs surface to an Sb flux initiates an Sb/As exchange reaction. The XPS data also indicate that the exchange reaction is self-limiting after the topmost layer of As has exchanged. We also found that the reaction occurred faster when using cracked rather than uncracked Sb. A RHEED study of the same physical system was also undertaken. In particular, we measured the change in the specular spot intensity diffracted from an InAs surface while exposing it to an Sb flux. We find that the specular intensity drops sharply at the start of the Sb soak then recovers toward its initial value. The time needed for the diffracted intensity to stabilize is a strong function

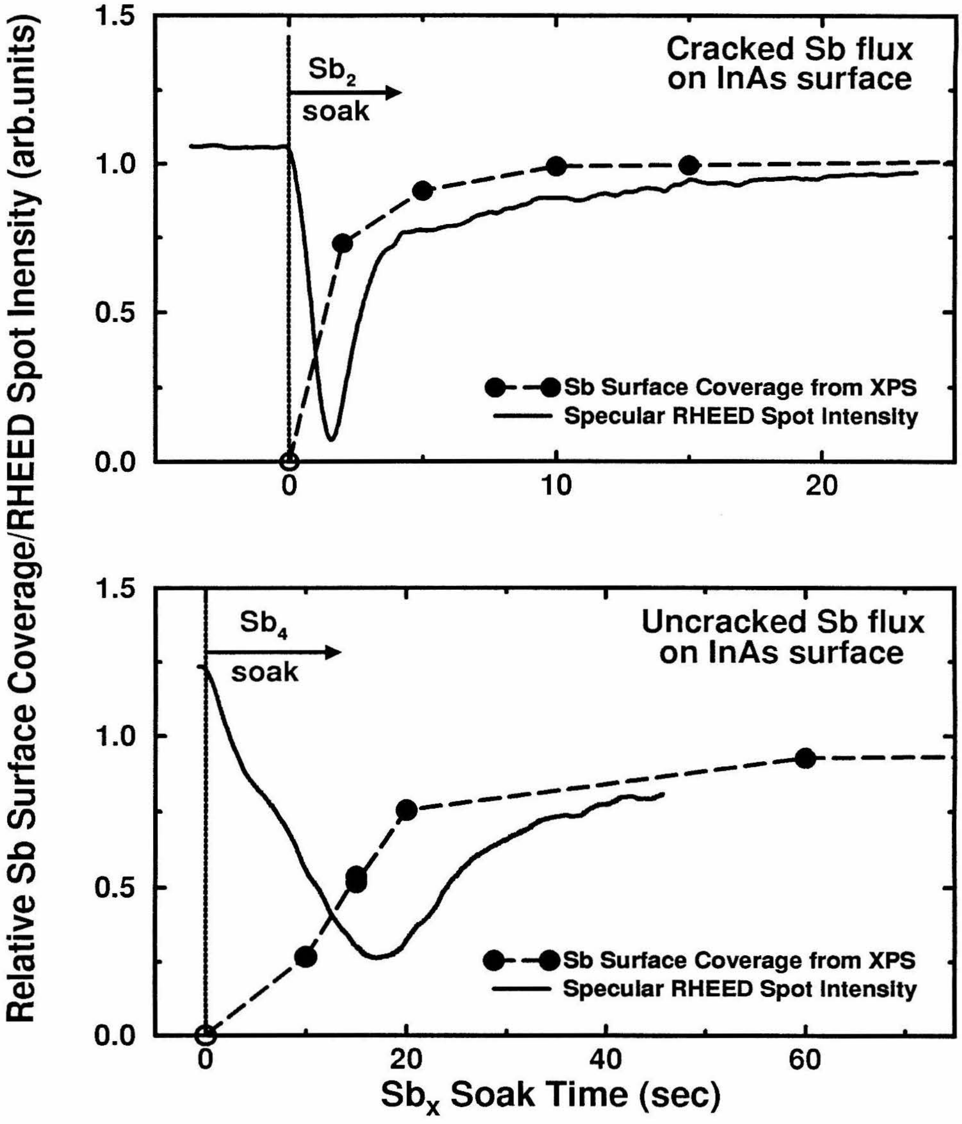

Figure 6.5: A comparison of representative RHEED data from Fig. 6.2 and XPS measurements of relative Sb surface coverage of InAs surfaces exposed to an Sb flux. Each RHEED data curve is representative of a series of data sets taken immediately prior to preparing a surface for an XPS measurement. The timescales on which the RHEED dynamics occur and Sb surface coverage changes are very similar. This indicates that the changes in the RHEED specular spot are related to the Sb/As exchange reaction.

of the Sb species incident on the InAs surface. For fluxes consisting primarily of Sb and Sb_2, the diffraction patterns stabilize much faster than incident fluxes made up of Sb_4. We also find that the surface stabilizes faster when the absolute Sb flux is increased. Both of these behaviors are consistent with the conclusion that changes in the RHEED pattern are due to the Sb/As exchange reaction occurring on the crystal's surface. We also compare the RHEED data to time-dependent XPS measurements of the relative Sb coverage of InAs surfaces soaked in Sb fluxes. The stabilization time of the RHEED pattern is in good agreement with the time indicated by the XPS measurements for the Sb/As exchange reaction to reach completion. This further suggests that the RHEED dynamics are caused by the Sb/As exchange reaction. Though further study is necessary to confirm this conclusion, the RHEED results indicate the possibility of indirect, time-resolved studies of surface exchange reactions and interface formation. This result could have a wide array of potential applications ranging from basic material science studies to MBE process control in manufacturing.

References

[1] D. H. Chow, R. H. Milesand A. T. Hunter, *J. Vac. Sci. Technol. B* **10**, 888 (1992).

[2] G. Tuttle, H. Kroemer and J. English, *J. Appl. Phys.*, **67**, 3032 (1990).

[3] J.R. Waldrop, G.J. Sullivan, R.W. Grant, E.A. Kraut and W.A. Harrison, *J. Vac. Sci. Technol. B* **10**, 1773 (1992).

[4] M. W. Wong, D. A. Collins, T. C. McGilland R. W. Grant. To be published in *J. Vac. Sci. Technol. B* **11**, July/August (1993).

[5] "Thermodynamic Properties of the elements," D.R. Stull and G.C. Sinke, 39-42, American Chemical Society (1956).

[6] B.F. Lewis, R. Fernandez, A. Madhukar and F.J. Grunthaner, *J. Vac. Sci. Tech. B* **4**, 560 (1986).

[7] M.P. Seah and W.A. Dench, *Surf. Interface Anal.*, **1**, 2 (1979).

[8] C.M. Kwei and L.W. Chen, *Surf. Interface Anal.*, **11**, 60 (1988).

[9] S. Tanuma, C.J. Powell and D.R. Penn, *Surf. Interface Anal.*, **17**, 927 (1991).

[10] "Fundamentals of Surface Analysis of Thin Films," L.C. Feldman and J.W. Mayer, pg. 213-23, Elsevier Scientific Publishing Co. (1986).

[11] E.T. Yu, E.T. Croke, D.H. Chow, D.A. Collins, M.C. Phillips, T.C. McGill and J.O. McCaldin, *J. Vac. Sci. Technol. B*, **8(4)** (1990).

[12] E. T. Yu, M. C. Phillips, D. H. Chow, D. A. Collins, M. W. Wang, J. O. McCaldin and T. C. McGill, *Phys. Rev B.*, **46(20)**, 13379 (1992).

[13] M.C. Phillips, Y. Rajakarunanayake, J.O. McCaldin, D.H. Chow, D.A. Collins and T.C. McGill, SPIE **1285**, pg. 158, *Growth of Semiconductor Structures and High-*T_c *Thin Films on Semiconductors* (1990).

[14] Y. Rajakarunanayake, M.C. Phillips, J.O. McCaldin, D.H. Chow, D.A. Collins and T.C. McGill, SPIE **1285**, pg. 142, *Growth of Semiconductor Structures and High-*T_c *Thin Films on Semiconductors* (1990).

[15] Y. Rajakarunanayake, M.C. Phillips, J.O. McCaldin, D.H. Chow, D.A. Collins and T.C. McGill, *Mat. Res. Soc. Symp. Proc.*, **198**, pg. 427 (1990).

[16] D. A. Collins, M. W. Wang, R. W. Grantand T. C. McGill. Unpublished.

[17] J.M. Van Hove, C.S. Lent, P.R. Pukite, P.I. Cohen, *J. Vac. Sci. Technol. B* **1**, 741 (1983).

[18] J.H. Neave, B.A. Joyce, P.J. Dobson, N. Norton, *Appl. Phys. Lett.* **31**, 1 (1983).